University of Crete,
School of Science and Technology
Department of Physics

Bachelor Thesis

Study on the Ozone gas sensing properties of Al-doped NiO thin films.

Name : Athanasios Paralikis

Supervisor : Dr. Vasileios Binas

Approved by the examining committee on January, 2021.

Konstantinos Makris Professor	Ilias Aperathitis Doctor	Vasileios Binas Doctor

January, 2021

Abstract

Ever since the industrial revolution, mankind has been producing enormous amounts of gases that would otherwise not be present in the ambient environment in such quantities or at all. These gases are either products from or reactants to a chemical reaction and exist in both industrial and urban areas. A key component to the reasoning behind the monitoring of such gases is that, even though some of them can occur organically in nature, the sheer amount generated from mankind is more than enough to cause irreversible problems to both humans (health issues) and nature (damage to flora and fauna, climate change etc.). To tackle the effects of these compounds, they first need to be detected either macroscopically (concentration and total mass of a gas in a macroscopic environment such as a metropolitan area, a country, or the whole planet) or mesoscopically (concentration and total mass of a gas in a mesoscopic environment such as a room, a house, or a working facility). For this task, a wide range of gas sensors/detectors has been invented. Gas sensors are devices that can detect a gas through a change that occurs in the medium which they use and can translate that change into some kind of signal that provides valuable information about the targeted compound. One of the most wide spread techniques for gas detection is the use of Semiconductor Metal Oxides (S.M.O.), as they offer a great amount of advantages, one of which is the numerous different compounds that can be produced, being that they are easily modified. The main mechanism that governs these kinds of sensors is the alteration of the current flowing through them whilst being and not being in contact with the target gas. In this thesis Aluminum doped Nickel oxide thin films have been employed for the detection of ozone using amperometric measurements and have been characterised with three different techniques (XRD, FESEM, UV-Vis). The reason behind ozone being selected as the target gas, is that it constitutes a hazard and has been increasing in concentration in the troposphere, making it a dangerous compound that could harm both humans and animals alike. Something worth mentioning is that there has not been any projects regarding the detection of ozone using Aluminum doped Nickel oxide (Al:NiO).

Περίληψη

Από την απαρχή της βιομηχανικής επανάστασης, η ανθρωπότητα παράγει τεράστιες ποσότητες αερίων, τα οποία δεν θα μπορούσαν να βρεθούνε στην φύση σε τέτοιες περιεκτικότητες ή και καθόλου. Τα αέρια αυτά είναι προϊόντα ή αντιδρώντα σε κάποια χημική αντίδραση και υπάρχουν σε βιομηχανικές, αλλά και αστικές περιοχές. Ένας βασικός λόγος πίσω απο την ανάγκη για επιτήρηση τέτοιων αερίων, παρόλο που αυτά μπορούν να παραχθούν οργανικά στην φύση, είναι πως το ποσό που προκύπτει απο ανθρώπινη δραστηριότητα είναι ικανό να προκαλέσει μη αναστρέψιμα προβλήματα στους ανθρώπους (προβλήματα υγείας) αλλά και στην φύση(καταστροφή χλωρίδας και πανίδας κλπ.). Για να αντιμετωπιστούν οι επιδράσεις των ουσιών αυτών, πρέπει πρώτα να ανιχνευτούν είτε μακροσκοπικά (συγκέντρωση και ολική μάζα αερίου σε μακροσκοπικό περιβάλλον όπως μια μητροπολιτική περιοχή, μια χώρα ή ολόκληρος ο πλανήτης) είτε μεσοσκοπικά (συγκέντρωση και ολική μάζα αερίου σε μεσοσκοπικό περιβάλλον όπως ένα δωμάτιο, ένα σπίτι ή ένας χώρος εργασίας). Για τον σκοπό αυτό, μία μεγάλη γκάμα αισθητήρων αερίων έχει αναπτυχθεί. Οι αισθητηήρες αυτοί είναι συσκευές που μπορούν να ανιχνεύσουν μία αέρια ουσία διαμέσου μιας μεταβολής στο μέσο ανίχνευσης που μεταφράζεται σε κάποιου είδους σήμα, το οποίο παρέχει σημαντικές πληροφορίες για τον αέριο στόχο. Μία από τις πιο διαδεδωμένες τεχνικές για την ανίχνευση αερίων είναι η χρήση ημιαγώγιμων οξειδίων μετάλλων (S.M.O.), λόγω των πολλαπλών πλεονεκτημάτων τους, ένα εκ των οποίων είναι η πληθώρα συνδυασμών που μπορούμε να παράξουμε, όντας ευκόλως τροποποιήσιμα υλικά. Ο κύριος μηχανισμός που διέπει αυτού του είδους τους αισθητήρες είναι η εναλλαγή της έντασης του ρεύματος που ρέει μέσα τους όταν βρίσκονται ή δεν βρίσκονται σε επαφή με το αέριο. Στην πτυχιακή εργασία αυτή γίνεται χρήση λεπτών υμενίων οξειδίου του Νικελίου με ”ντοπάρισμα” Αλουμινίου, για ανίχνευση όζοντος, με αμπερομετρικές μετρήσεις, τα οποία έχον πρωτίστως χαρακτηριστεί με τρείς διαφορετικές τεχνικές (XRD, FESEM, UV-Vis). Το όζον επιλέχθηκε ώς ο αέριος στόχος της εργασίας καθώς αποτελεί κίνδυνο και η συγκέντρωση του στην τροπόσφαιρα αυξάνεται συνεχώς, καθιστώντας το απειλή για την ανθρώπινη υγεία, όπως και για την υγεία την συνολικής πανίδας του πλανήτη. Άξιο αναφοράς είναι το γεγονός πως στην βιβλιογραφία δεν υπάρχει κάποιο πρότζεκτ που να αφορά την ανίχνευση όζοντος με χρήση του οξειδίου του Νικελίου με ”ντοπάρισμα” Αλουμινίου.

Acknowledgements

Athanasios Paralikis, Physics Department, U.o.C.

In these few lines I would like to thank the people that supported me throughout the time I spent for the completion of this bachelor thesis.
Firstly I would like to thank Dr.V. Binas and Prof.G. Kyriakidis for allowing me to be a part of their team, providing me with the materials needed to complete this thesis and imbuing me with their invaluable guidance. Moreover, I am sincerely thankful to V. Kabitakis for his useful assistance and whose own thesis inspired this project as well as Dr. Aperathitis for the preparation of the samples and his crucial comments regarding this thesis.

All this, although, could not be possible without the priceless help and counseling of Dr. E. Gagaoudakis who transcended the border of a simple co-worker and supervisor and went out of his way to assist me in any way imaginable.
Last, but definitely not least, I would like to thank my friends and family that were supporting me all this time, even when I was a burden to their own endeavors.

Contents

List of Figures

List of Equations

1 Metal oxide Gas Sensors

1.1 Semiconductors

Semiconductors are any of a class of crystalline solids intermediate in electrical conductivity between conductors (generally metals) and insulators (e.g. most ceramics). Semiconductors can be pure elements, such as Silicon (Si) or Germanium (Ge), or compounds such as Gallium Arsenide (GaAs) or Cadmium Selenide (CdSe). [6]

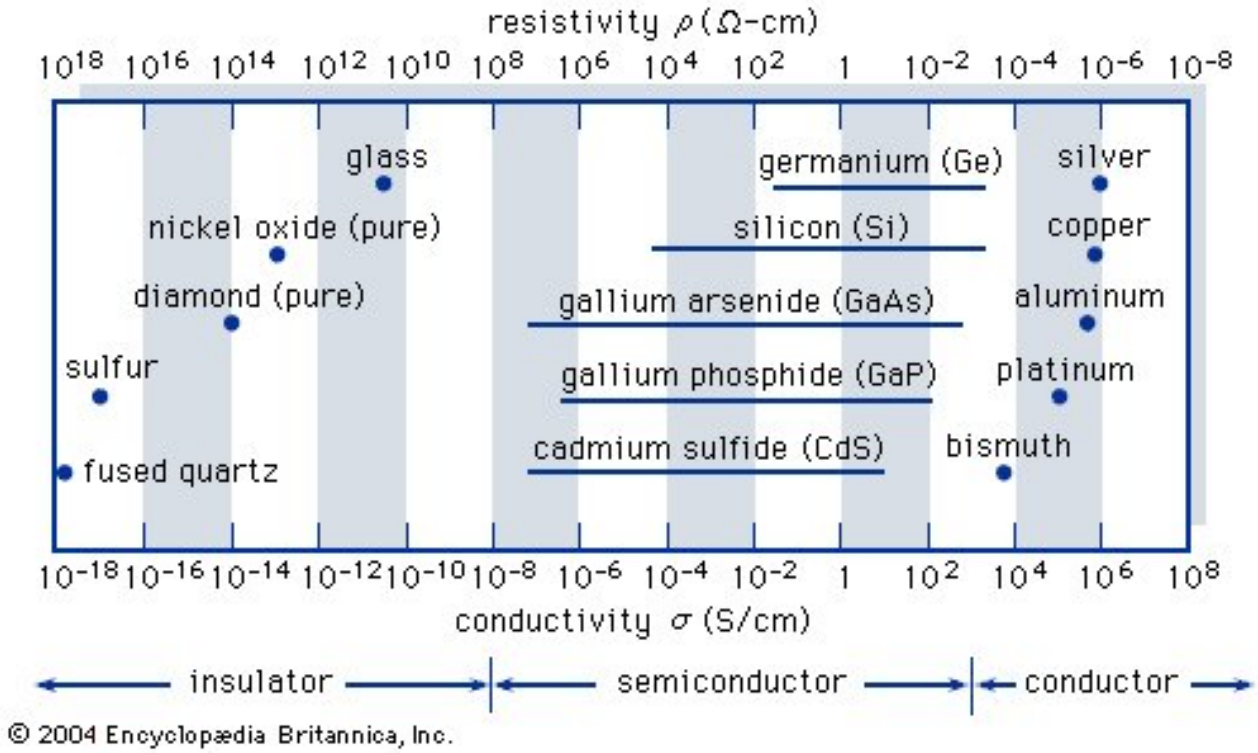

Figure 1.1: Typical range of conductivity values for insulators, semiconductors, and conductors.

Conductivity values of semiconductors are between the extremes such as fused quartz and aluminum, and are generally sensitive to temperature, illumination, magnetic fields, and minute amounts of impurity atoms. Conductivity is determined by the energy gap between the so called “Valence band” (V-band) and “Conduction band” (C-band). When an electron is excited from the V-band to the C-band, an electron-hole pair is created, both of which can become carriers of electrical current. In metals the two bands overlap, so electrons are free to move in the material without having to be excited in any way. Insulators, on the other

hand, have a huge band gap, therefore being virtually unable to conduct electricity.

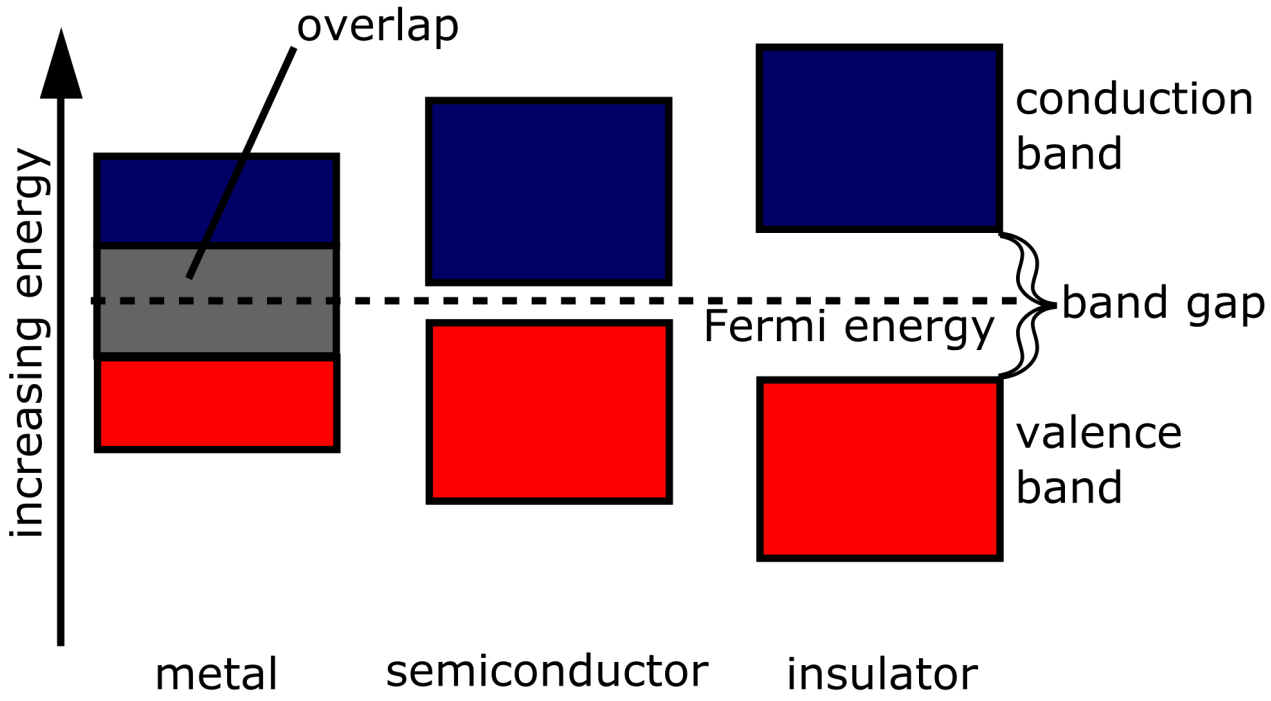

Figure 1.2: Representation of the band model.

Semiconductors are employed in the manufacture of various kinds of electronic devices, including diodes, transistors, and integrated circuits [16]. Such devices have found wide application because of their compactness, reliability, power efficiency, and low cost. As discrete components, they have found use in power devices [8], gas sensors [15, 40] , and light emitters [33], including solid-state lasers [19]. They have a wide range of current- and voltage-handling capabilities and, more important, lend themselves to integration into complex but readily manufacturable microelectronic circuits. They are, and will be in the foreseeable future, the key elements for the majority of electronic systems, serving communications, signal processing, computing, and control applications in both the consumer and industrial markets. Before arriving at the modern use of semiconductors though, their study began at the early 19th century. After over a century of studies, scientists have divided semiconductors into three main “families” according to their compounds:

1. Elemental semiconductors that, as aforementioned, are composed of single elements from column IV, although other elemental semiconductors such as Selenium (Se) from column VI are also used but in a lesser degree.

2. Binary and ternary compounds that are formed using elements from the third and fifth (III-V) columns of the periodic table.

3. Binary and ternary compounds that are formed using elements from the second and sixth (II-VI) columns of the periodic table.

Ternary compounds can also be formed by elements from three different columns—for instance, Mercury Indium Telluride (HgIn2Te4), a II-III-VI compound. They also can be formed by elements from two columns, as stated before, but with a significant difference in the composition, such as Aluminum Gallium Arsenide (AlxGa1 − xAs), which is a ternary III-V compound, where both Al and Ga are from column III and the subscript x is related to the composition of the two elements from 100 percent Al (x = 1) to 100 percent Ga (x = 0). This, although, is not to be confused with doping. [44]

Doping means the introduction of impurities into a semiconductor crystal for the purpose of modulating its electrical, optical and structural properties. The dopant is integrated into the lattice structure of the semiconductor crystal and the number of outer electrons define the type of doping.

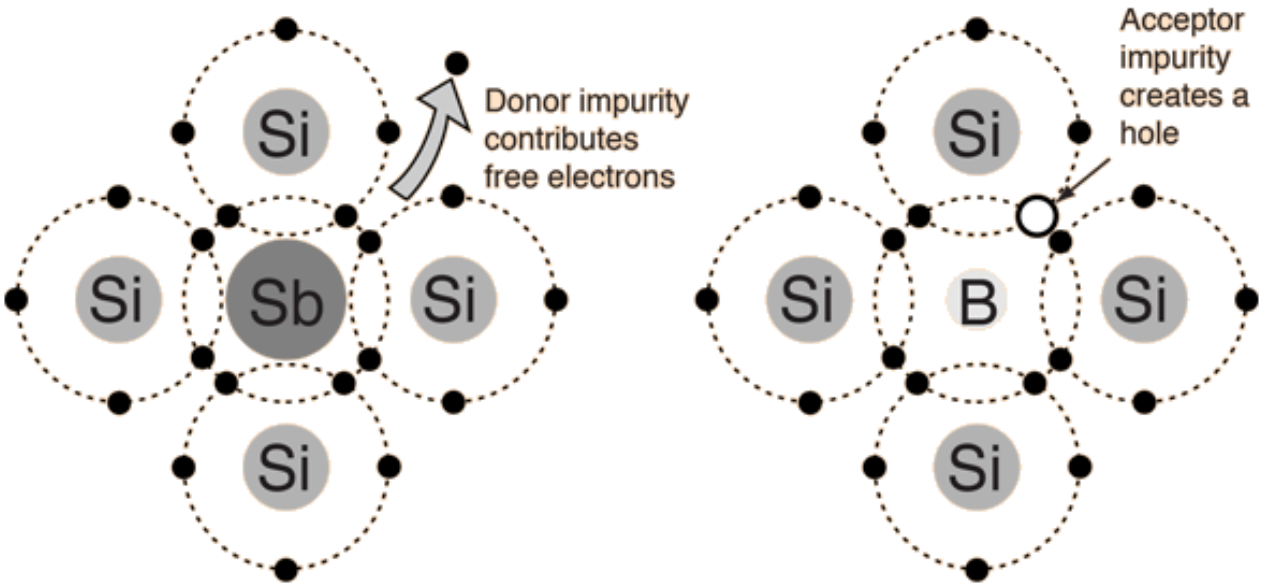

Figure 1.3: Representation of donor/acceptor impurity

According to the above, semiconductors are divided into two groups depending on the dominant carrier of the electrical current. If the carrier is the electron then the semiconductor is called n-type. Otherwise, if the carrier is a hole (missing electron-positive charge), the semi-

conductor is called p-type.

The addition of donor impurities contributes electron energy levels high in the semiconductor's band gap so that electrons can be easily excited into the conduction band. In the case of acceptor impurities, they contribute hole energy levels low in the band gap, so that electrons can be easily excited there, leaving positively charged holes in the valence band.

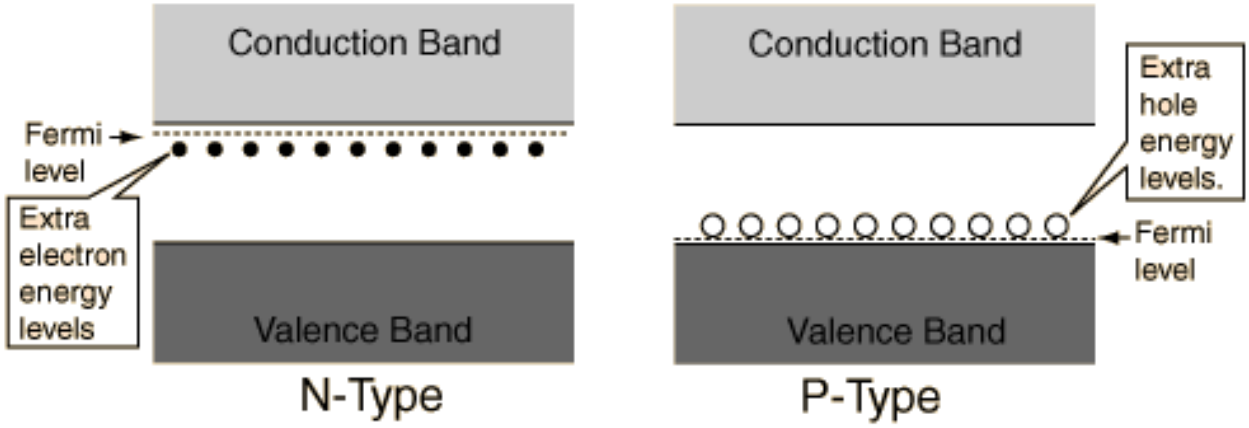

Figure 1.4: Depiction of the extra energy levels contributed by the impurities

1.2 Metal Oxides

A distinct category of semiconductors, are metal oxides. Oxides of all metallic elements have been studied showing a great variety of properties in terms of structures, acidity, basicity and conductivity. Namely, an oxide can exhibit molecular, 1-dimensional chain, 2-dimensional layer, or 3-dimensional structures. There are basic, amphoteric, and acidic metal oxides depending on the identity of the metallic element. Furthermore, the range of electrical conductivity displayed is also broad, ranging from insulators and semiconductors to conductors and superconductors. Their composition could also diverse from stoichiometric to non-stoichiometric [44] .

Due to the aforementioned variety, it would be wise to classify metal oxides according to their properties, so since structure gives us more information for the oxide's physical and chemical properties, typical oxides are firstly categorized according to the dimensionality of their structures.

	1	2	12	13	14	15	16	17	18
2	Li_2O	BeO		B_2O_3	CO CO_2	N_2O NO NO_2			
3	Na_2O Na_2O_2 NaO_2	MgO		Al_2O_3	SiO_2	P_4O_6 P_4O_{10}	SO_2 SO_3	Cl_2O ClO_2	
4	K_2O K_2O_2 KO_2	CaO	ZnO	Ga_2O_3	GeO_2	As_4O_6 As_4O_{10}	SeO_2 SeO_3		
5	Rb_2O Rb_2O_2 Rb_9O_2	SrO	CdO	In_2O_3	SnO_2	Sb_4O_6 Sb_4O_{10}	TeO_2 TeO_3	I_2O_5	XeO_3 XeO_4
6	Cs_2O $Cs_{11}O_3$	BaO	HgO	Tl_2O Tl_2O_3	PbO PbO_2	Bi_2O_3			

Figure 1.5: Typical metal oxides of main group elements

Oxidation number	3	4	5	6	7	8	9	10	11
+1		Ti_2O^{l}							Cu_2O Ag_2O
+2		TiO	VO NbO		MnO	FeO	CoO	NiO	CuO Ag_2O_2
+3	Sc_2O_3 Y_2O_3	Ti_2O_3	V_2O_3	Cr_2O_3		Fe_2O_3	Rh_2O_3		
+4		TiO_2 ZrO_2 HfO_2	VO_2 NbO_2 TaO_2	CrO_2 MoO_2 WO_2	MnO_2 TcO_2 ReO_2	RuO_2 OsO_2	RhO_2 IrO_2	PtO_2	
+5			$V_2O_5^{l}$ Nb_2O_5 Ta_2O_5						
+6				CrO_3^{c} MoO_3^{l} WO_3	ReO_3				
+7					$Re_2O_7^{l}$				
+8						RuO_4^{m} OsO_4^{m}			

[m] molecular, [c] chain, [l] layer, others 3-demensional.

Figure 1.6: Typical metal oxides of transition metals

Molecular metal oxides

Molecular metal oxides such as Ruthenium tetroxide or RuO_4 (mp 25°C and bp 40°C) and Osmium tetroxide or OsO_4 (mp 40°C and bp 130°C) have low melting and boiling points and are generally prepared by heating the metal powder in an oxygen atmosphere at 800°C. Their structure is tetrahedral and are soluble in organic solvents and also slightly soluble in water. Since these oxides are very volatile and poisonous, they are to be dealt with extremely carefully.

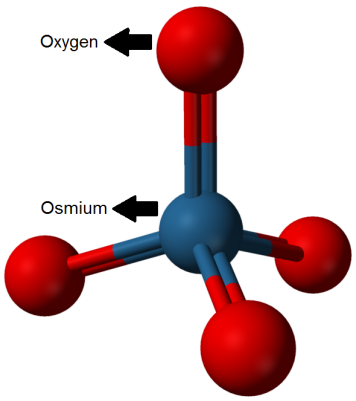

Figure 1.7: Structure of OsO_4

One dimensional chain-like metal oxides

This category does not have any distinct characteristics other than their chain-like structures. Oxides that fall under this category are Mercury oxide or HgO, a red crystalline compound, with an infinite zigzag structure, Chromium trioxide or CrO_3, also a red crystalline compound, with a low melting point (197^{o}C) and a structure of tetrahedrally coordinated chromium atoms that share vertices.

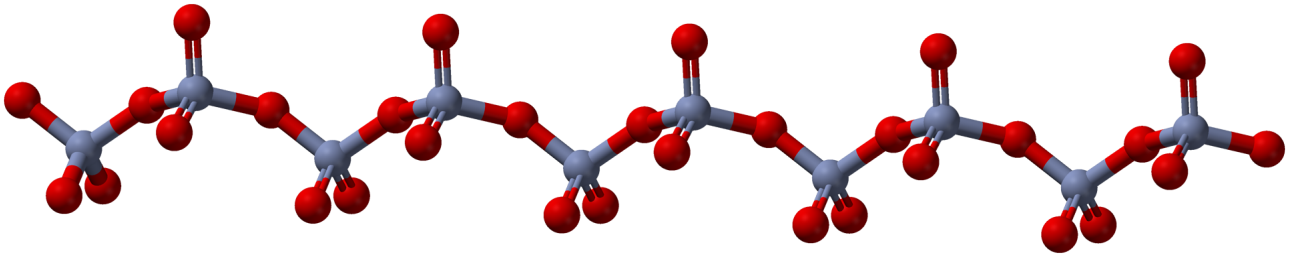

Figure 1.8: Structure of CrO_3

Two dimensional stratified oxides

These are layer compounds with a tetragonal pyramid structure where the metal atom is located at the peak of the pyramid and oxygen atoms at the four vertices. These metal atoms are located alternatively above and below the layer of oxygen, parallel to it. SnO and PbO are prime examples of this structure. Nevertheless, there is a slightly altered structure represented by MoO_3, which is composed of layers of distorted MoO_6 octahedra in an orthorhombic crystal. The octahedra share edges and form chains which are cross-linked by oxygen atoms to form layers.

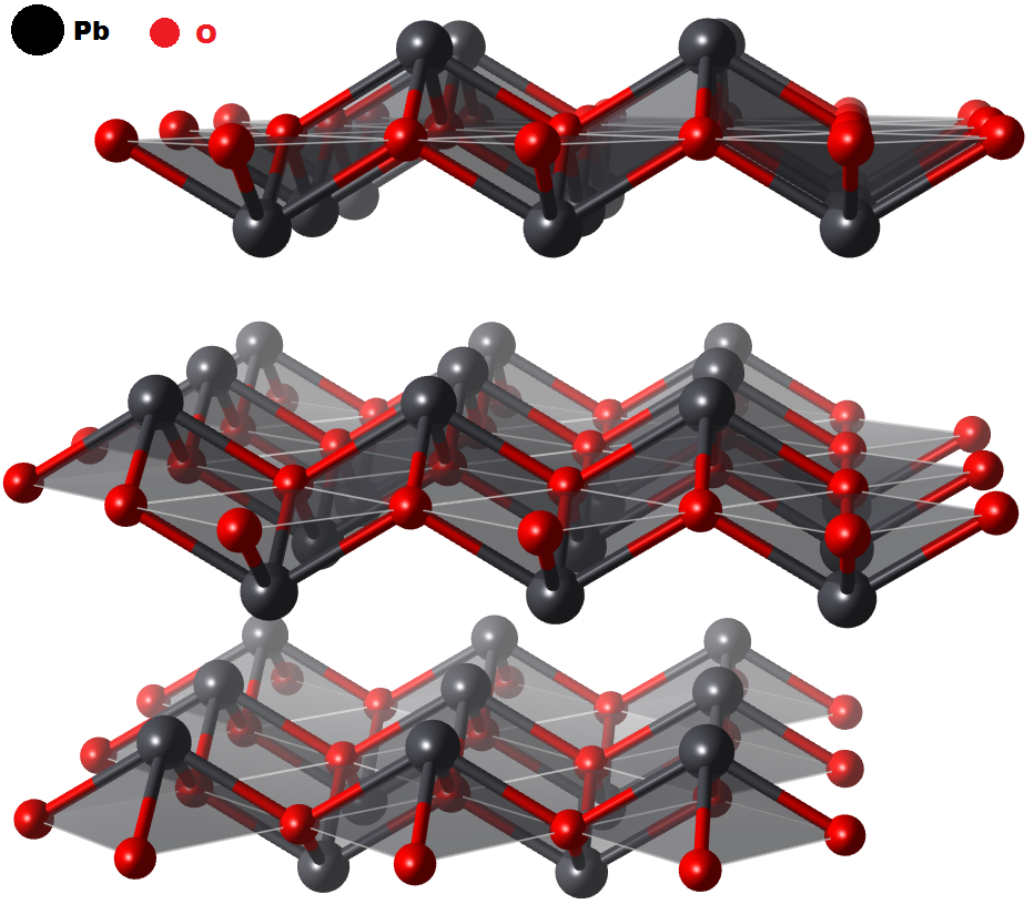

Figure 1.9: Structure of PbO

Three dimensional oxides

Alkali metal oxide, M_2O (where M is Li, Na, K, and Rb) have the antifluorite structure, and Cs_2O has the anti-$CdCl_2$ lamellar structure. They are mostly obtained by peroxide M_2O_2 when an alkali metal burns in the air if the amount of oxygen is less than stoichiometric.

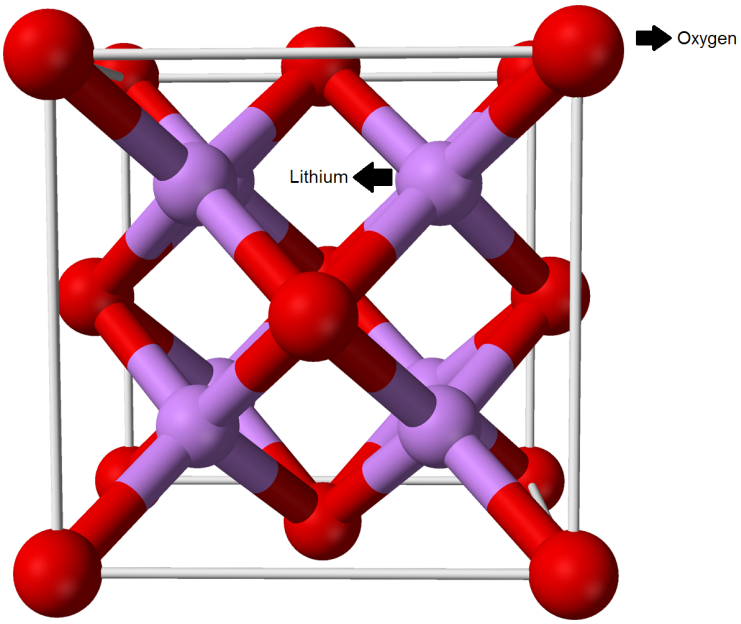

Figure 1.10: Structure of Li_2O

MO type metal oxides

Finally arriving at the metal oxides' type that we are mostly concerned in this project. The basic structure of transition metals (Ti, Zr, V, Mn, Fe, Co, Ni, Eu, Th, U) and Group 2 metals (Mg, Ca, Sr, Ba, Ra), except for BeO (Wurtz type) is the rock-salt structure, with the only difference being that transition metals have defective structures and the ratios between metal and oxygen are non-stoichiometric. For example, FeO has the composition Fe_xO (x=0.89-0.96) at 1000°C. This charge imbalance is compensated by the partial oxidation of Fe^{2+} to Fe^{3+}.

In recent years, SMO materials have attracted much attention in gas sensors [40]. However, the current semiconductor materials are mostly wide bandgap semiconductors, requiring energetic operating conditions. Most of them require high temperature or ultraviolet light to excite their valence band electrons, which make them difficult to be applied in practical applications. Scientists have been trying to enhance the gas-sensitive properties of SMO materials in room temperature.

However, there is a wide range of gas sensors with different abilities and capabilities, upon which we are going to expand in the following section. [44]

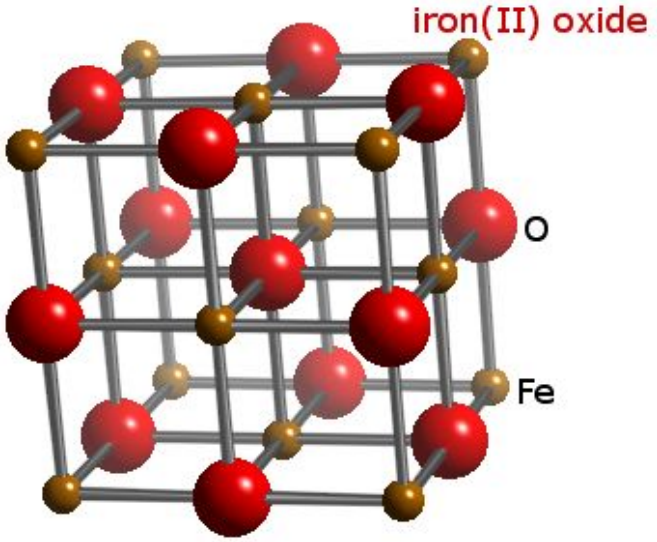

Figure 1.11: Structure of FeO

1.3 Gas Sensors

The first thing we need to take into account when talking about gas sensors, are the so called ”3S”. Sensitivity, Selectivity and Stability are the three main attributes of a sensor and the telltale sign of its quality [15].

Sensitivity

As a physical quantity, sensitivity describes the magnitude of change in the electrical signal passing through the sensor when it comes into contact with the target gas as opposed to a stable state with no contact with the target gas. There are many ways in which we can amplify this quantity through optimization of our sensor. One of these ways is tampering with the grain size. For a significantly large grain, with grain size of D » 2L (thickness of the electron depletion layer) [a] the conductance is limited by a Schottky barrier at the boundaries between grains, known as grain boundary control. If D = 2L [b], conductance is limited by necks between grains (known as neck control) and if D < 2L [c], conductance is influenced by every grain (known as grain control) [15].

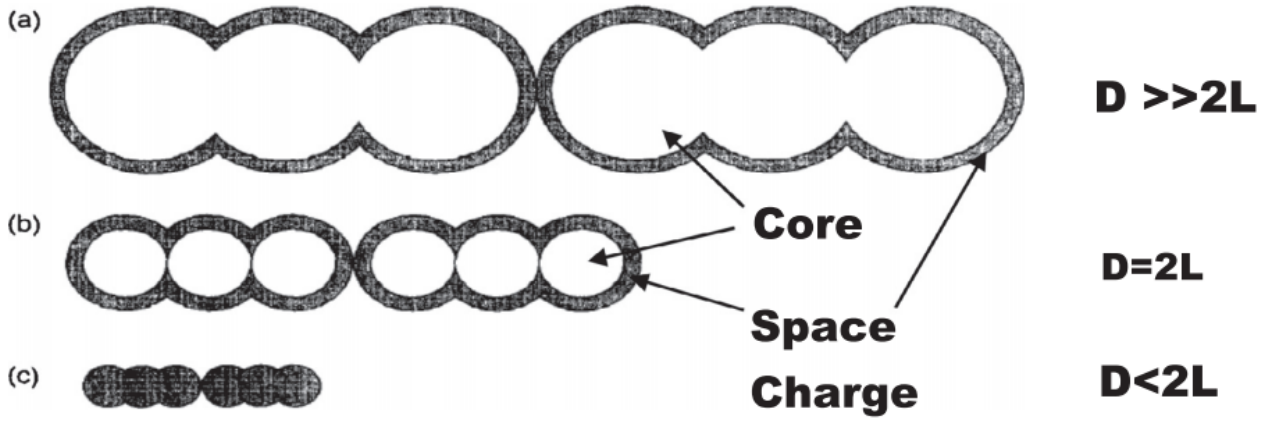

Figure 1.12: Representation of grain sizes in a specimen

Thus, the smaller the grain size the better the sensitivity of gas sensors, but excessive decrease in grain size decreases structural stability. A finely dispersed small crystallite has a detrimental effect on the temporal stability of the sensor.

Another solution has been stated to be the change of the specimens' microstructure and porosity, as SMOs with higher surface area exhibit increased gas sensitivity [5].

Selectivity

The selectivity of a gas sensor refers to the ability of the material to discern the target gas from a plethora of others, as it would be required in a domestic or industrial use. Most scientists follow two main approaches to solving this predicament. The first one is to create a material that is solely selective to one compound and have close to zero cross-sensitivity for other compounds which may be present to a working environment. The second approach is to discriminate between several analytes in the mixture. This is usually achieved by either modulation of temperature or by using sensor arrays [34], but unfortunately it does not help at all in projects dealing with a one-material sensor.

Stability

Rounding out the three most important aspects of a gas sensor, stability speaks for itself as it is a quantity that describes the ability of a gas sensor to produce a stable as well as reproducible signal when in contact with a specific target gas. In the real market, valuable and cost-worth sensors have a life expectancy of 2-3 years which correspond to 17 thousand to 26 thousand hours of operation [31]. Scientists have categorized stability into two different kinds. One is related to the reproducibility of the sensor's characteristics during a certain period of time at working conditions including high temperature and presence of a known analyte. Such stability is referred to as active stability [15]. The other stability is connected with retaining the sensitivity and selectivity during a period of time at normal storage conditions like room temperature and ambient humidity and has no distinctive name. An accurate one could be dormant stability, but it has not been adopted in any project. According to one study the factors that might be responsible for sensor instability are: structural transformation, phase transformation, poisoning, degradation of contacts and heaters, bulk diffusion, error in design, change in humidity, fluctuations of temperature in the surrounding atmosphere, interference effect. Increasing stability of SMO sensors has no universal and uniform approach. To some degree, it could be increased by calcination and annealing of the specimen and by reducing the working temperature as to ease the load of the mechanical parts. Moreover, doping or synthesis of mixed metal oxides could also work.

In general, gas sensors are the intermediate device for detecting the toxic gases. Its two main parts are the transducer and the receptor. Receptor is called the material, which is interacting with the gas molecules. The interacting gas molecules can change some respective parameters of the gas sensing material such as resistance, refractive index, mass, biological properties, heat, light etc. The other part, called the transducer, detects the changing parameters and converts it into the electrical signal.

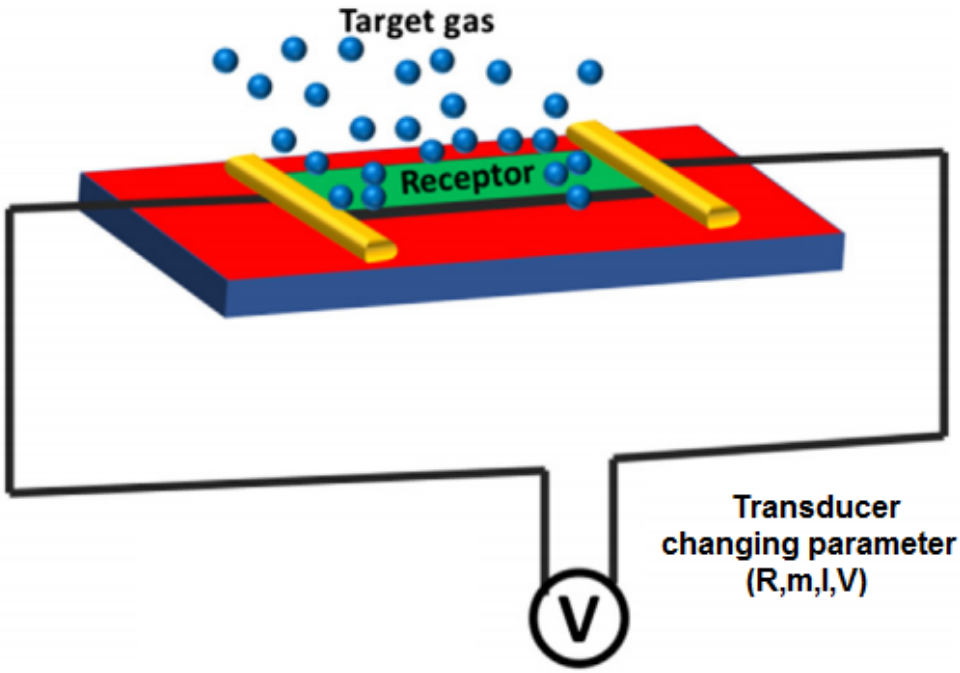

Figure 1.13: Schematic representation of the two main parts of a gas sensor, the transducer and the resceptor.

A given sensor can be described from the target measurement point of view e.g., temperature sensors, or from the platform point of view, e.g., electronic sensors [26]. The following figure shows a possible breakdown of sensor classes based on the transducer's changing parameter in the sensor.

The type of gas sensor used in this thesis which used metal oxides is also referred to as chemiresistive or electrochemical, because of the chemical reactions taking place at the surface of the specimen leading to a change in electrical resistivity [27]. More on this specific family is coming up in Chapter 2, where the sensing mechanisms will be thoroughly explained. In the following lines some other major families of gas sensors will be partially explained.

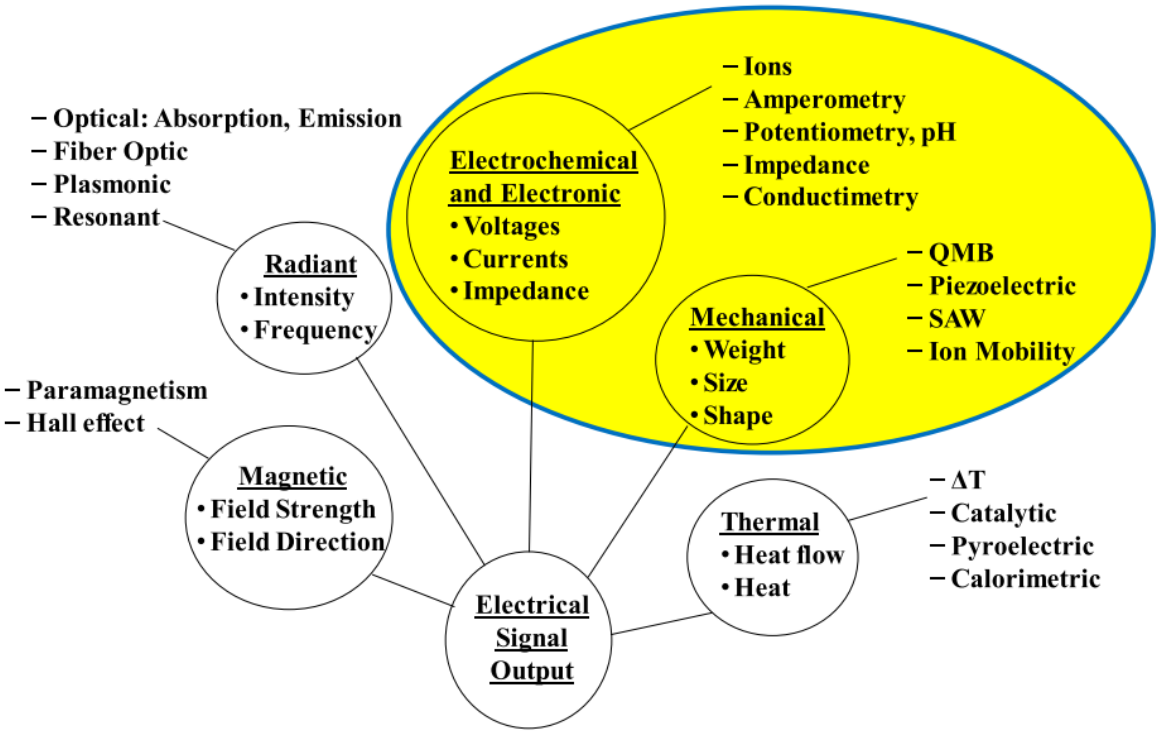

Figure 1.14: Schematic representation of the classes of chemical sensors by transducer platform, with examples of the different sensor types.

Catalytic combustion

Like chemiresistive sensors, catalytic combustion sensor fall under the general category of solid state sensors. This is a simple and very popular method of detecting combustible gases in air. The energy released from the oxidation of a combustible gas on the surface of a catalyst is converted to a change in the resistance of a temperature sensitive element. A thin platinum wire coil is embedded in a porous refractory bead, usually alumina, of about 1mm in diameter. A reference and an active element are arranged in a wheatstone bridge. The active element is doped with a catalyst chosen to suit the gas to be detected. Platinum, palladium and thoria are some of the catalysts used. [41] The reference element, on the other hand, has no catalyst. The beads are brought up to their normal operating temperature through an applied voltage. The bridge is balanced initially in the presence of air free of combustibles. A known concentration of the combustible gas of interest is then admitted with air into the detector. The combustible gas and the oxygen react on the surface of the catalyst and the resultant energy raises the temperature of the bead, and hence that of the

platinum coil, leading to a change of resistance in one arm of the bridge. The output of the bridge is nearly linear, with gas concentration enabling simple gas detection systems to be designed. The technique, however, is basically non-selective; certain gases and compounds inhibit (sulphur) or poison (silicones) the catalyst, and the presence of oxygen is necessary to complete the combustion process. A form of this sensor known as the Pellistor has been popular since the 1950s. [41]

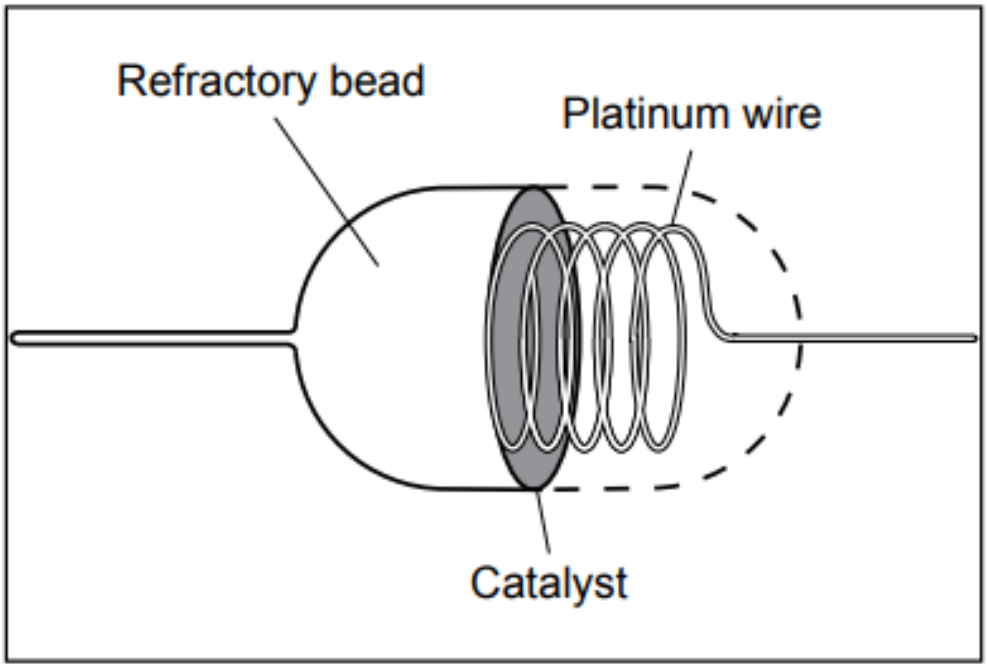

Figure 1.15: Basic construction of a Pellistor.

Thermal conductivity

This is perhaps one of the simplest and oldest of gas sensors. It relies on the difference between the thermal conductivity of different gases and the main parts of a sensor are shown in Figure 1.16. It is basically a heated filament which is exposed to the sample gas and an identical filament exposed to a reference gas. The filament is made of temperature sensitive materials such as platinum, nickel or tungsten. It is often sealed with glass to stop any catalytic combustion on its surface, if there are any combustible gases in the gas mixture. The two elements are normally used in a wheatstone bridge arrangement which is in balance when the zero gas is passed through the sample side. When a gas of different thermal conductivity and known concentration is passed through the chamber, the rate of loss of

heat alters, hence the filament temperature will change and the bridge will be unbalanced. The bridge imbalance can be calibrated in terms of the concentration of the gas of interest. In conclusion, this type of sensor is ideal for binary mixtures and is used extensively in gas chromatography. However, if more than one gas is present, great care has to be taken in predicting and compensating for the other gases. [23, 41, 57]

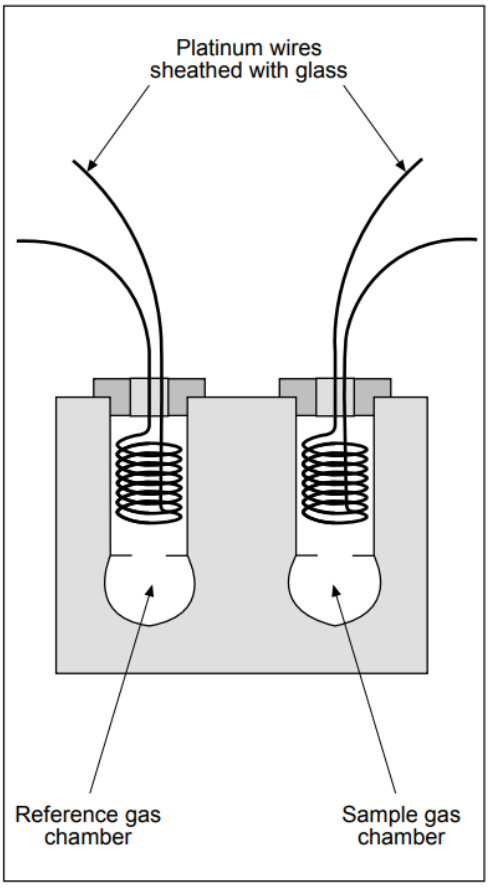

Figure 1.16: Schematic representation of a thermal conductivity gas sensor.

Photo-Acoustic Spectroscopy (P.A.S.)

P.A.S. falls under the general category of optical gas sensing, meaning that it utilises the interaction of electromagnetic waves with a target gas in order to produce some kind of signal, triggering a detector to the presence of the aforementioned target gas. Photoacoustic spectroscopy (PAS) has one crucial characteristic different over the other absorption spectroscopy methods and that is the reason that this is the method chosen to represent the general category. The other methods (NDIR, TDLAS, CEAS) have the disadvantage that their detection limit scales linearly with the laser-gas interaction length, so it is difficult for the

equipment to guarantee both sensitivity and small size. It is also hard for them to benefit from high-power lasers because of the max peak power of the photodetector. In contrast, due to the basic principle behind it, in P.A.S. the detection limit is approximately independent of the laser-gas interaction length, which enables both sensitivity and small size in its equipment.

PAS is an indirect absorption spectroscopy technique. As an effective supplement to direct absorption spectroscopy, it detects non-radiative relaxation channels of excited molecules. The ground state molecule is excited to a higher energy state after absorbing light energy and returns to the ground state by non-radiative transition and releases the energy. Some part of the released energy will increase the kinetic energy of the molecules, which macroscopically shows an increase in temperature, and eventually changes the gas pressure. If the excitation light is modulated, this change in gas pressure will also follow the modulation of the light to generate gas pressure waves (sound waves), which will eventually be detected by an acoustic sensor (such as a capacitive microphone).

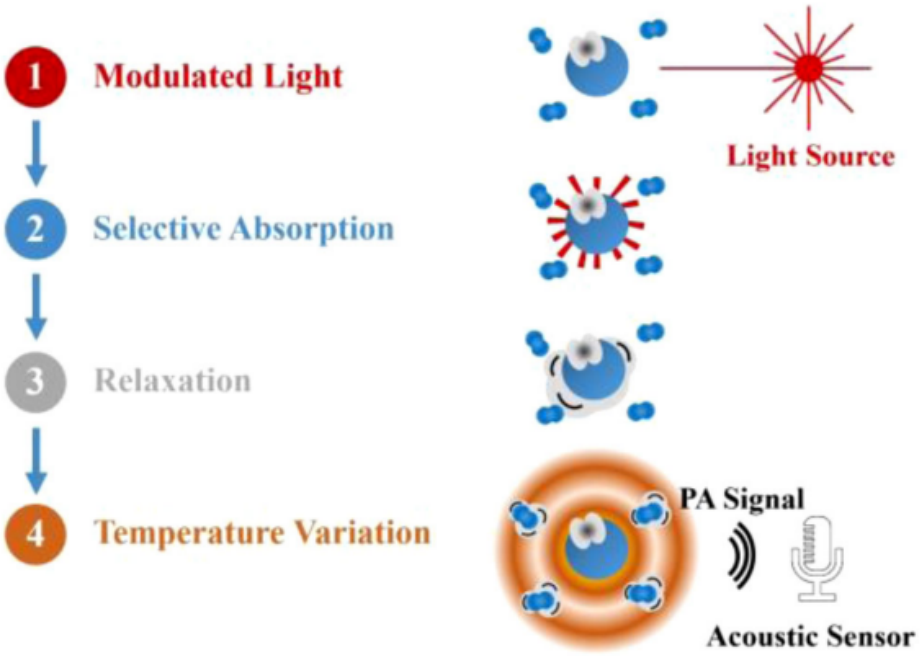

Figure 1.17: Principle of the PAS effect.

The advantages of this method are clear:

a) PAS does not require an optical detector. Therefore, it has no selectivity for detection wavelengths so that it can be applied to all wavelengths from ultraviolet to infrared and tera-hertz.

b) PA signal is directly proportional to the power of the excitation light, and the detection sensitivity can benefit from the constant development of highpower lasers.

c) The zero-background property allows the detector and pre-amplifier to work in an extended dynamic range based on the zero signal. [55]

2 O_3 gas sensing

2.1 Target gases

Ever since the industrial revolution, gas production has become a dominant feature both in the industry and in domestic life. These gases can be the products of a chemical reaction or reactants to one. Most of the times these gases (NO_2, NH_3, CO, CO_2, ethanol, methanol, O_3, H_2 etc.) are hazardous either to humans, the end product or the environment [10, 56]. This created a demand for detecting and monitoring the aforementioned gases for energy saving, environmental and health protection reasons. As far as energy production and saving is concerned, in recent years, hydrogen emerges as the pioneer candidate for the renewable energy sources due to its ultrahigh energy density (120 kJ/g) [43]. However, H_2 is highly flammable. Moving to more dangerous gases, certain air pollutant toxic gases such as NO_2, NO, CO_2, ethanol, and methanol are the most commonly released into the environment from vehicles, energy sources, and power plants that use fossil fuels [45]. NO_2 is produced during the burning of fossil fuels, and when it reacts with moisture, it forms acid rain that is very harmful to ecosystems. Humans are also vulnerable to some of those pollutants, such as methanol vapor (CH_3OH) that affects the human central nervous system (CNS) and circulatory system, which could cause headaches, vertigo, nausea, vomiting, loss of vision, and even possibility of death depending upon the level of exposure. In addition, acid acetic as an organic acid and colorless is a hazardous material that can damage internal organs [35]. Two great families that play a great role in this project are Nitrogen oxides (NOx) and Volatile Organic Compounds (VOCs).

Nitrogen Oxides (NOx)

In atmospheric chemistry, NOx is a generic term for the nitrogen oxides that are most relevant for air pollution, namely nitric oxide (NO) and nitrogen dioxide (NO_2). Nitrogen oxides (NOx) are considered as the primary air pollutants, and as aforementioned, could be majorly attributed to the combustion exhaust of fossil fuels from both stationary factory chimneys

and mobile vehicles. They can contribute to a series of severe environmental issues such as acid rain, photochemical smog, the ozone hole, and even exert detrimental effects on human health. The majority of environmental problems and health hazards is a result of various processes occurring in the atmosphere. The array of potential NOx reactions with different compounds present in the atmosphere (O_3, VOC, etc.) is quite complex [25, 45]. Furthermore, in the presence of sunlight various photochemical reactions are possible. Some reactions which NOx can undergo in the atmosphere are presented here briefly.

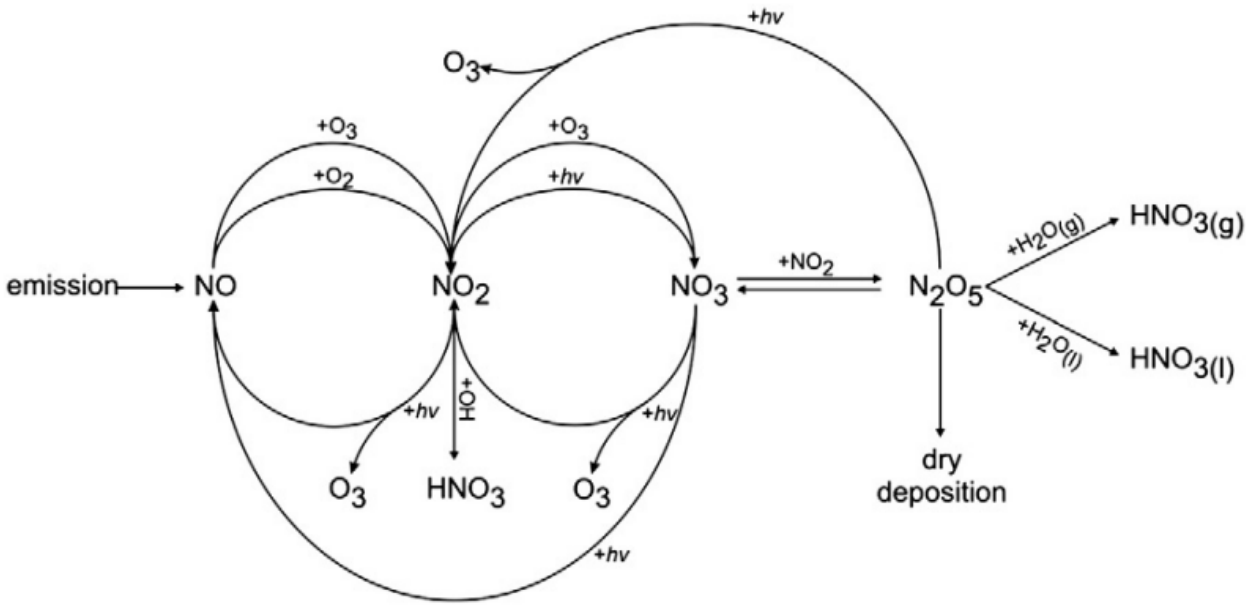

Figure 2.1: Schematics of atmospheric NOx reactions.

Due to an increasing social sensitivity in matters of environmental well-being, in the last few decades extensive efforts have been devoted to control the NOx emission, leading to the funding of projects dedicated to create appropriate materials for sensing and disintegrating these kinds of gases. Some characteristics of Nitrogen dioxide (NO_2) are that it is reddish-brown gas above 21.2°C (294.3 K) with a pungent, acrid odor, becomes a yellowish-brown liquid below 21.2°C (294.3 K), and converts to the colorless dinitrogen tetroxide (N_2O_4) below −11.2 °C (261.9 K). Nitric oxide (NO), on the other hand, is a colourless gas that has a boiling point of -152°C and when exposed to oxygen becomes NO_2 : $2NO+O_2 \rightarrow 2NO_2$. A plethora of detection methods of these gases have been reported over the years, that may include monitoring the air with a VIS-NIR field spectrometer and then using statistical models to predict the concentration levels of the target gas [37], or using amperometric measurements

[2, 29]. MoS_2 films have also been reported to be adequate H_2 sensors, a testament to the abundance of target gases that can be detected using a single material with slight changes, and the difficult task of being able to discern them [2].

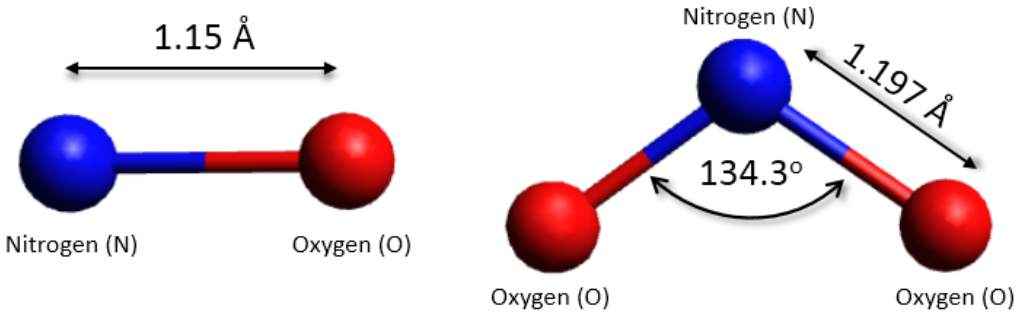

Figure 2.2: Schematic representation of NO and NO_2 molecules.

Volatile Organic Compounds (VOCs)

Volatile organic compounds (VOCs) are organic chemicals that have a high vapour pressure at ordinary room temperature. Their high vapor pressure results from a low boiling point, which causes large numbers of molecules to evaporate or sublimate from the liquid or solid form of the compound and enter the surrounding air, a trait known as volatility. For example, formaldehyde (CH_2O), which evaporates from paint and releases from materials like resin, has a boiling point of only –19°C. They are an enormous family of gases that include both man-made (C_6H_6, CH_2O, C_3H_6O) and biologically generated (C_5H_8, $C_{10}H_{16}$, CH_3OH) ones. Actually most scents or odours are VOCs that our body detects and they are the main means of communication between plants, or sometimes between plants and animals. They are also used in medicine, agriculture, industry and many more aspects of human life. Hence, not all of them are harmful either to humans or the environment as a whole, though most man-made VOCs tend to be hazardous [18, 35]. Coming full circle to the topic of this thesis, VOCs have been detected through the use of SMO using materials such as SnO_2, In_2O_3, ZnO, NiO providing valuable information to the scientific community [20–22, 36].

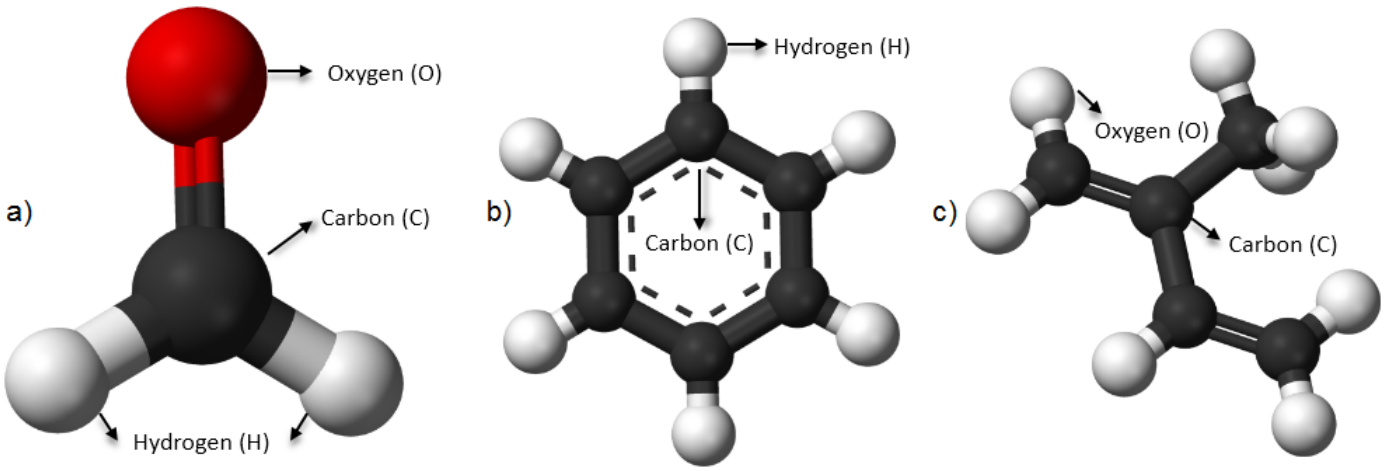

Figure 2.3: Schematic representation of a) Formaldehyde, b) Benzene and c) Isoprene.

Closing off this section, VOCs and NOx gases play such an important role because when they interact, they produce O_3. Although the chemical cycles that lead to the production of ozone are too many to count, the main chemical reactions the reader should be at least familiar with are :

$$CO + OH \rightarrow CO_2 + HO_2 \tag{2.1}$$

$$HO_2 + NO \rightarrow OH + NO_2 \tag{2.2}$$

$$NO_2 + h\nu \rightarrow NO + O_3 \tag{2.3}$$

In a nutshell, VOCs react with the ambient air and produce CO into the environment which then produces hydroperoxyl. This compound (HO_2) is used to produce NO_2 which then produces ozone, and OH, which reacts once more with CO [58].

In order to get a good grasp of the way we detect these target gases, we will dive into the gas sensing mechanisms that govern the reactions between them and our materials. Though depending on the sensor type, there are different mechanisms, we will mainly focus on the

electrochemical sensors that apply to the specimen we are using in this thesis.

2.2 Sensing mechanisms

As far as gas sensing abilities are concerned SMOs are preferred because they exhibit superior performance over other sensors due to their excellent physical and chemical properties and unique structure. The properties of SMOs are often greatly affected by the material size. In particular, at the nanoscale, a material will show unique properties due to the nano-effect. For example, the electrical properties undergo very significant changes, creating a good gas sensing material [47].

In general, common SMO-based gas sensors detect a gas through the change of the electrical signal caused by the gas. Gas sensing mechanisms explain the means through which a gas can cause changes in the electrical properties of a material and thus change the electrical signal that we detect. Scientists have divided the most commonly used gas sensing mechanisms into two categories. One category explains the aforementioned changes in electrical properties in the microscopic level and includes mechanisms such as Fermi level control theory, grain boundary barrier control theory, and EDL/HAL (Electron Depletion Layer/Hole Accumulation Layer) theory. Explanatory as they might be, these concepts are more theoretical. In application, changes in electrical properties are always accompanied by changes in physical properties such as energy bands. The other category is relatively macroscopic, and it focuses mainly on the relationship between materials and gases. The adsorption/desorption model, the bulk resistance control mechanism and the gas diffusion control mechanism belong to this kind of theory. In this project we will be focusing on the adsorption/desorption model, as it is the main mechanism through which the gas sensing process takes place [27].

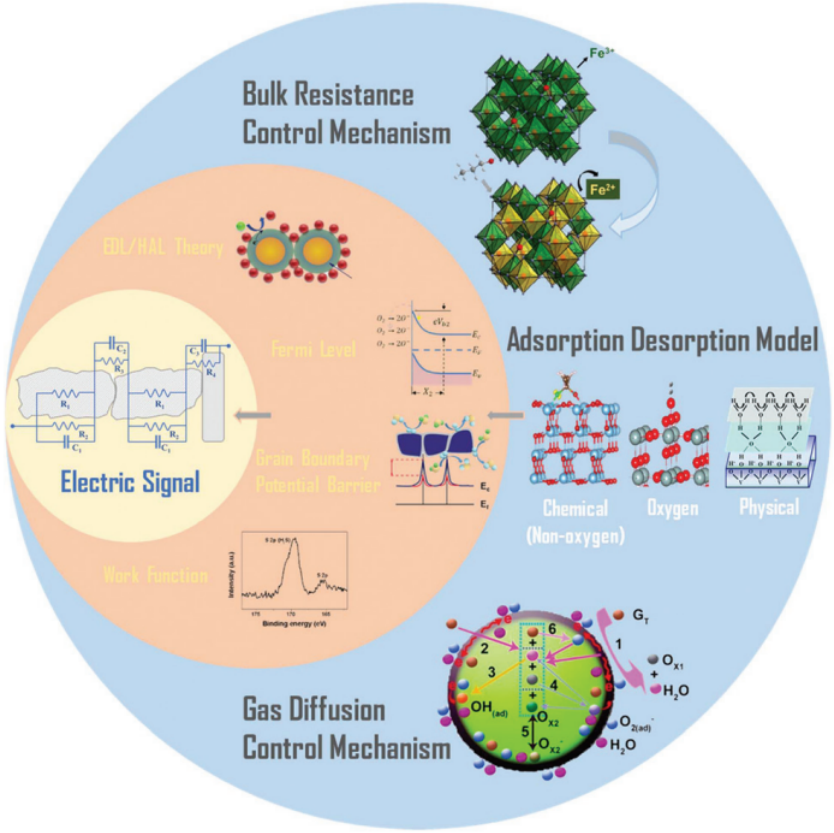

Figure 2.4: Gas sensing mechanisms of metal oxide semiconductors: classification and summary.

Adsorption/desorption model

This model is the basis of most of the current mainstream gas sensing mechanisms. It mainly focuses on the change of concentration of charge carriers resulting in resistance change, that occurs when a gas come into contact with the surface of our material. Researchers have correlated the change in conductance and work function of SMOs with the presence of gases such as O_2 and CO, as early as the 1930s.

The most mainstream of these mechanisms is called “Oxygen adsorption mechanism” which is suitable for almost all SMO gas sensing materials and has as extensions of it the EDL/HAL theory. Its simplistic description is that when an SMO is exposed to air, oxygen molecules are adsorbed on the surface of the material. This adsorbed oxygen takes electrons from the material conduction band to form negative oxygen species. Since the electrons in the conduction band are consumed, an electron depletion layer is formed. Furthermore, oxygen adsorption causes the Fermi level to move down and the conduction band to bend upwards. In an n-type SMO this lowers the current passing through our material. In a p-type SMO this

reaction amplifies the current due to the creation of holes. When the target gas enters and undergoes a redox reaction with the negative oxygen species, the electrons are re-released back into the conduction band, the electron depletion layer shrinks, the oxygen vacancies re-form, the Fermi level and the conduction band return to normal, and eventually the resistivity is restored.

In another study that concerns mesoporous SnO_2 [54], the creation of the depletion layer is generalized in a grain boundary potential barrier control model, which is also based on an oxygen adsorption model. Due to the porous structure of the material, the oxygen molecules that had been adsorbed on the grain surface gradually diffuse and eventually cover all the grains. The loss of electrons naturally causes the generation of an electron depletion layer and the formation of a potential barrier between adjacent grains, which in turn leads to an increase in the resistance towards electrons flowing at grain boundaries. Thus, when a target gas that acts as an electron donor, in this case H_2S, enters the frame, this depletion layer shrinks once more, the barrier between adjacent crystal grains is lowered, the electron flow becomes smooth again, and the electric resistance is also decreased. Unlike the formation of an electron depletion layer by n-type SMO materials, p-type SMOs, such as Mn_3O_4 [32], form a hole accumulation layer, accompanied by a decrease in electrical resistance.

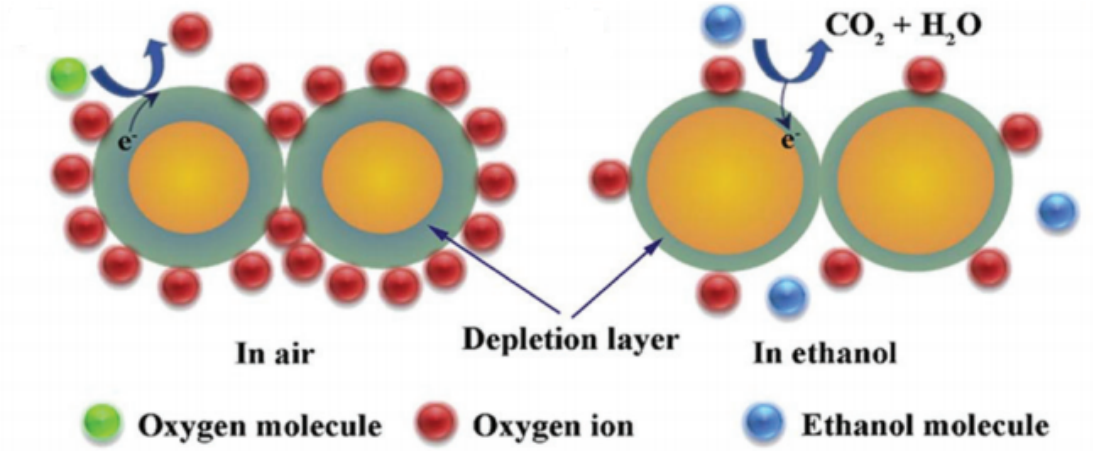

Figure 2.5: Schematic diagram of EDL theory for n-type MOS gas sensing materials.

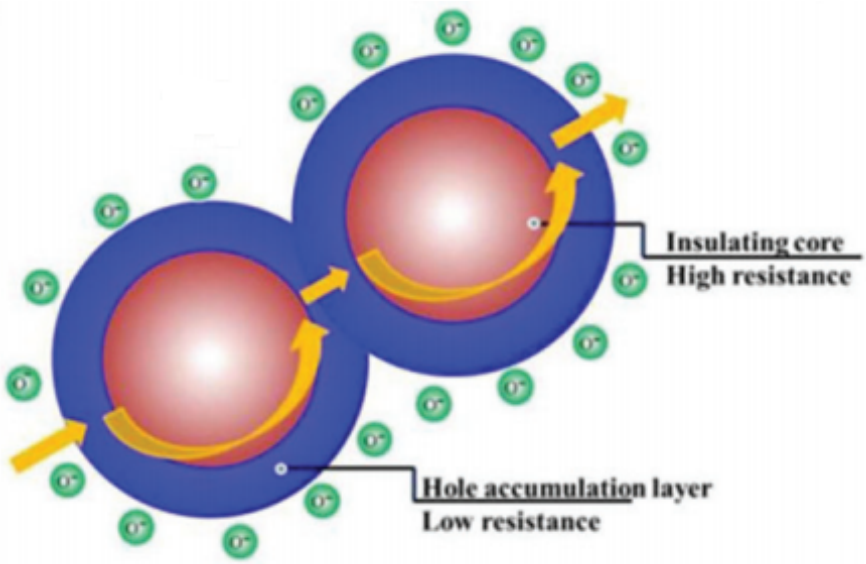

Figure 2.6: Schematic diagram of HAL theory for p-type MOS gas sensing materials.

If we want to be precise, the “oxygen adsorption model” falls under the category of the “Chemical adsorption/desorption model”, but is described independently due to the massive amount of research regarding it, that has described it adequately.

According to the “Chemical adsorption/desorption model” the gas comes into direct contact with the material and undergoes a chemical reaction, resulting in a change of the electrical signal. A great example of this model is the aforementioned SnO_2, when detecting H_2S [54]. After an X-ray photoelectron spectroscopy (XPS) analysis, the researchers inferred that during the sensing measurement process, in addition to reacting with the adsorbed oxygen anions, H_2S directly chemically adsorbs onto SnO_2 to produce SnS_2. $2H_2S + SnO_2 \rightarrow SnS_2 + 2H_2O$ This results in higher sensitivity as SnS_2 has a narrower band gap than SnO_2, thus effectively reducing the bulk resistance of the crystal grains. Nevertheless, this comes baring a toll regarding recovery properties, as it takes a certain non-negligible amount of time to convert SnS_2 back to SnO_2.

Bulk resistance control mechanism

The main function of this mechanism is the phase transformation that occurs in the gas sensing material, that leads to a change in the resistance. However, the mechanism is relatively narrow in scope, and it is only applicable for the analysis of the gas sensing process of

materials such as γ-Fe_2O_3 and ABO_3 SMO composites [50].

Gas diffusion control mechanism

In the process of gas sensing there are two main components, the sensing material and the target gas. The first two mechanisms discussed focus on the physical and chemical properties of the material. This mechanism is more focused on the gas diffusion process, and the most important factor affecting this process is the morphology of the material. This mechanism is something that has been discussed and proposed by the early 1990s. In fact, this theory can be used as a supplement to the first two mechanisms to more fully explain the changes in physical parameters during the gas sensing process. [42, 53]

2.3 Characteristics and detection of O_3

Ozone is a pale blue gas with a distinctively pungent smell, which, in the stratosphere (10-20 to 50 kilometers above the earth surface), serves as a protective shield against the sun's harmful ultraviolet radiation. Nevertheless, in the troposphere (0 to 10-20 kilometers above the earth surface) it acts as a harmful pollutant with a multitude of potential associated adverse health effects. Ozone is a powerful oxidant (far more so than dioxygen) and has many industrial and consumer applications related to oxidation [52].

This same high oxidizing potential, however, causes ozone to damage mucous and respiratory tissues in animals, and also tissues in plants, above concentrations of about 0.1 ppm. Exposure to ozone is associated with various respiratory symptoms including dyspnea, upper airway irritation, coughing, and chest tightness [25]. Tropospheric, or ground level ozone, is not emitted directly into the air, but is created by chemical reactions between oxides of nitrogen (NOx) and volatile organic compounds (VOC) as previously stated. This happens when pollutants emitted by cars, power plants, industrial boilers, refineries, chemical plants, and other sources chemically react in the presence of sunlight. Ozone is most likely to reach unhealthy levels on hot sunny days in urban environments, but can still reach high levels during colder months, meaning that we need a year-round monitoring system. Ozone can also be transported long distances by wind, so even rural areas can experience high ozone levels [58].

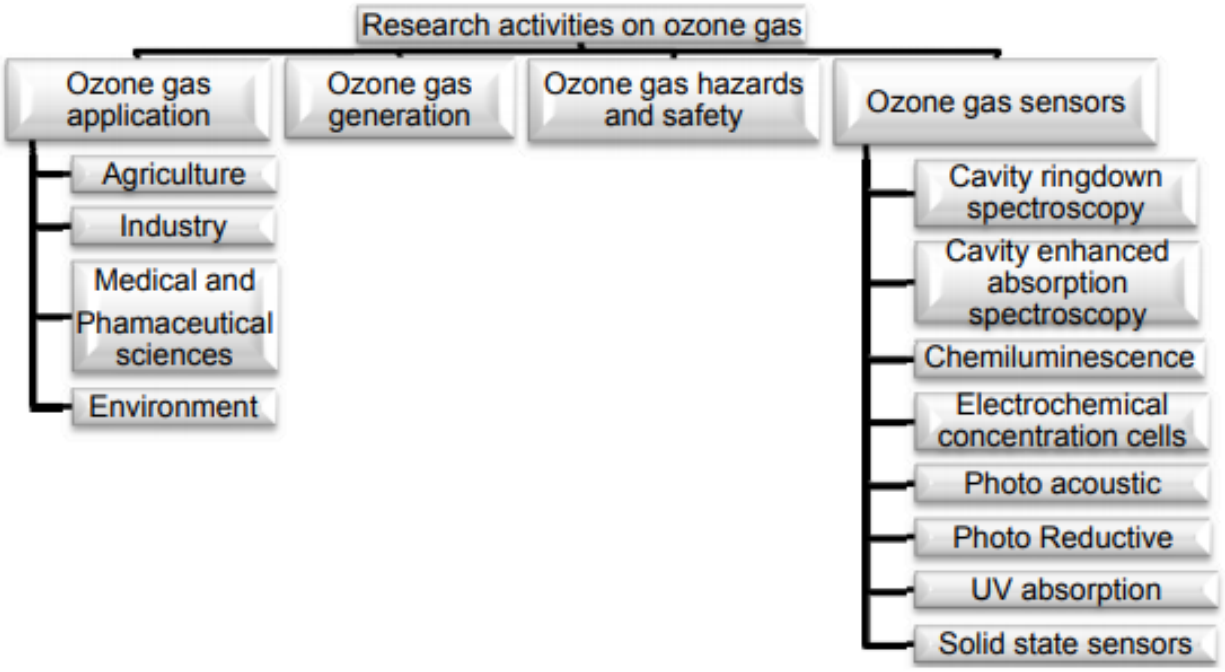

Figure 2.7: Research activities on ozone gas

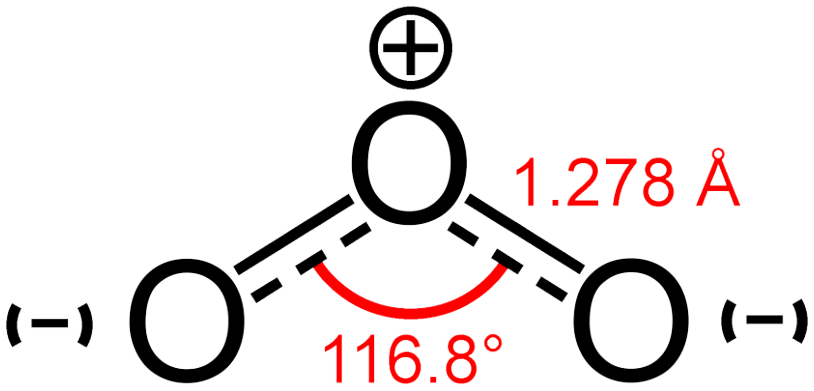

Figure 2.8: Schematic representation of O_3 molecule

As aforementioned there are a hand-full of ways to detect hazardous gases [14]. Nevertheless, ozone, when compared to other gases, has not been so vigorously studied, but does have a range of sensors able to detect it as shown in Figure 2.6. Before analyzing the main subject of this thesis, which is amperometric gas sensing using a metal oxide semiconductor, we firstly need to take a peak into another notable way the scientific community is able to detect O_3, as to present at least one more alternative.

Spectroscopic detection

In other chapters and sections of this thesis we have talked about or will be talking about spectroscopy both as a tool for analyzing a specimen and as a way to detect gases. Several gas molecules of environmental and domestic significance exhibit a strong absorption in some part of the electromagnetic spectre. Therefore, a sensitive and a selective gas detector based on this unique molecular property (i.e., absorption at a specific wavelength) can be developed using absorption spectrophotometry. This method has an inherent advantage to measure ozone absolutely without the requirement for consumables to operate or calibrate. Ozone absorbs light in the Hartley band (200–310 nm), the Huggins band (310–375 nm), the Chappius band (375–603 nm), and the Wulf band (beyond 700 nm). It has peak absorption at 253.65nm and 603nm. A typical absorption spectroscopic experimental setup is made up of the following components: Source of light radiation (light sources can either be broadband or chromatic,light emanating from a broadband light source must be propagated through a collimating lens to eliminate scattering effects), a monochromator (except when light source is a laser), a light coupler, waveguide (fibre, fibre bundle, planar wave guide), variable attenuator, lenses (optical), cuvette (absorption cell or gas cell), light detection unit (spectrometer, photo detector), amplifier, secondary filter, transducer, data acquisition unit, data processing unit, and display unit. Figure 2.8 is a typical extrinsic experimental setup for ozone measurements using optical absorption spectroscopy [14].

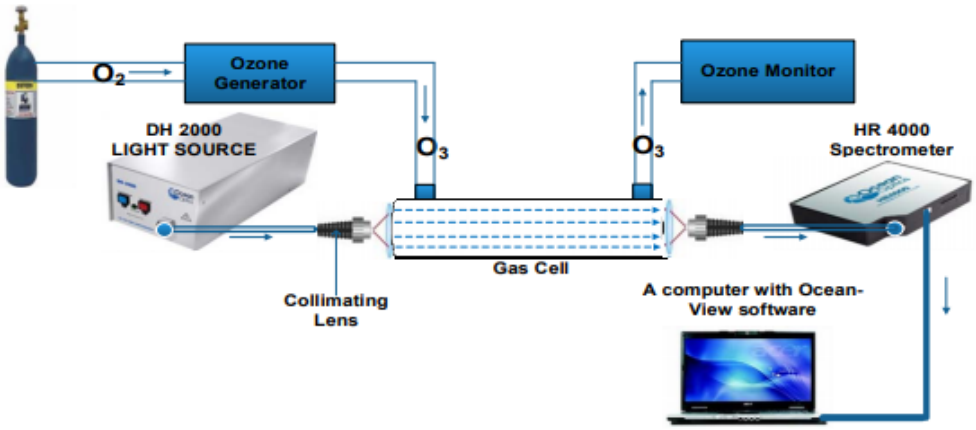

Figure 2.9: Basic layout for O_3 sensing with optical spectroscopy

Having said all of that, one of the main weapon in a scientist's arsenal for the detection of O_3 among other hazardous gases is the SMO gas sensor.

Amperometric/Conductometric sensors using metal oxides

A project of great importance to the present thesis is the work of Katerinopoulou D. et al. In her project ZnO thin films were deposited by the DC Sputtering technique on commercial transducers and glass substrates. The sensing properties for the detection of O_3 of these thin films, of various thicknesses, were investigated by both the conductometric (constant UV irradiation) and S.A.W. techniques. What is worth mentioning is that in both cases the results were more than promising. This goes to show how versatile SMOs are. [30]

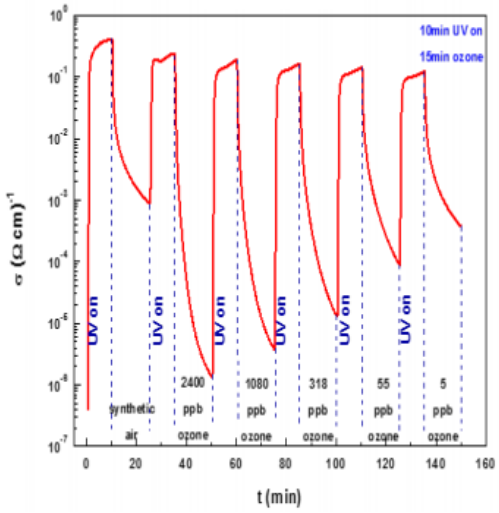

Figure 2.10: Photoreduction-oxidation cycles of ZnO film 230 nm.

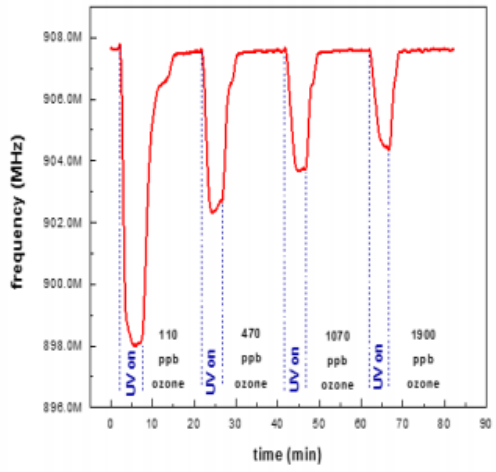

Figure 2.11: 930 MHz SAW filter response towards different O_3 concentrations at RT for ZnO film of 100 nm

One project that would be ill-advised not to present is from Luis F., et. al. [13] as they tackle O_3 sensing using a pair of the most used materials in similar projects, Zinc oxide (ZnO) and Tin oxide (SnO_2) in a heterojunction as they were spin-coated onto an Al_2O_3 substrate containing 100 nm thick Pt electrodes separated by a distance of 50mm. These compounds have drawn the interest of many researchers due to their wide range of applications, mainly as devices for gas detection or chemiresistors. It is to be noted that ZnO and SnO_2 have generally been used at temperatures above 150^{o}C, as far as sensing is concerned, which could be dangerous when dealing with explosive gases, though scientists published that UV-light irradiation is showing to be an efficient and inexpensive way for room temperature stimulation and improvement of the chemiresistors sensing activity. Gas sensing measurements were performed at room temperature (26^{o}C) under a UV-light irradiation of λ=325nm. The mechanism behind the results is reported to be the oxygen depletion layer that has been previously discussed in this thesis. They managed to produce adequate results while simultaneously showing that UV iriddation benefits the heterojunction. As can be seen, this sample presents a good sensing response even for the lowest O_3 level tested here (20 ppb), total reversibility, and a good repeatability.

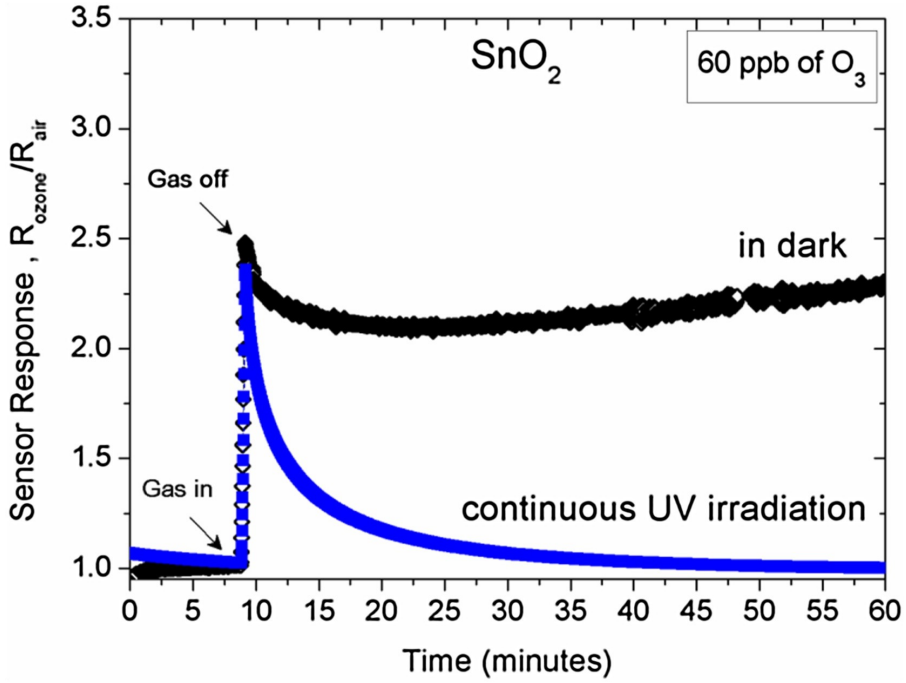

Figure 2.12: Room-temperature gas sensing response of SnO_2 nanoparticles exposed to 60 ppb of O_3 with and without (dark mode) continuous UV illumination. [13]

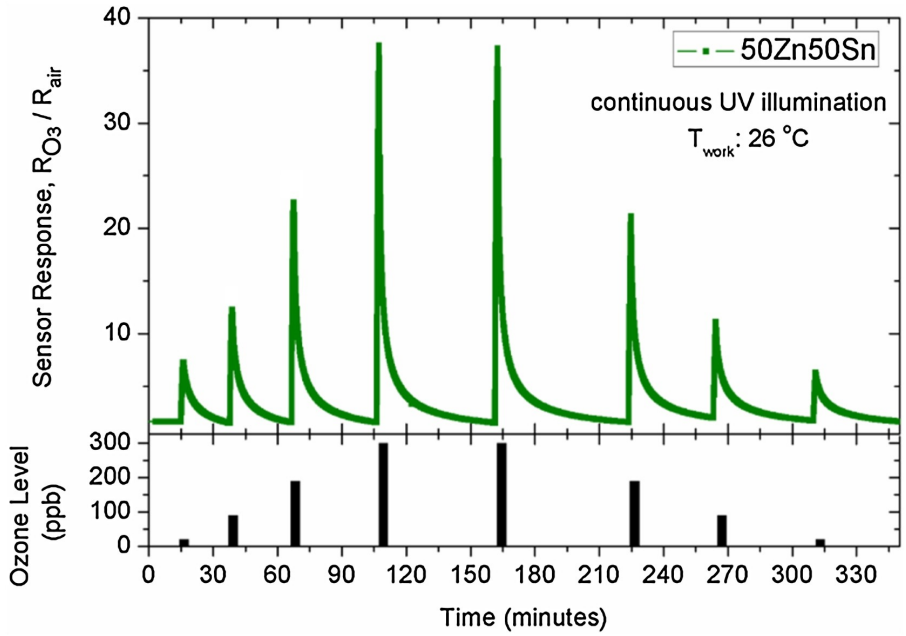

Figure 2.13: Room-temperature gas sensing response of 50Zn50Sn sample as a function of ozone gas concentration. [13]

Ending this chapter, we need to mention that numerous projects have been published regarding SMO gas sensing for O_3 [1, 4, 7, 11–13] and some of them will be mentioned in the experimental and result sections of this thesis. In order to reach them, though, the specimen used in this project needs to be analyzed and explained as thoroughly as possible.

3 Aluminum doped Nickel oxide(Al:NiO)

3.1 Physical/Chemical characteristics of NiO

As mentioned in Chapter 2, Nickel oxide (NiO) is a compound that falls under the general category of metal oxides [44], whilst Nickel is a silvery-white lustrous metal with a slight golden tinge and belongs in the transition metals [51]. It manifests in the cubic rock salt structure with octahedral Ni^{2+} and O^{2-} sites, a density value of about 6.67 gr/cm^3 and a band gap of 3.6-4 eV [50]. Due to its abundant resource availability, low production cost, non-toxicity, low growth temperatures and high adaptability to various substrates, NiO films can be employed in various fields, such as hole transport layers (HTLs) in perovskite photovoltaics, electrodes, electrochromic films, catalysts, dye-sensitized solar cells and chemical sensors [9]. Another noteworthy characteristic of NiO is its intrinsic p-type conductivity. Nandy et al. reported that the p-type conductivity of NiO may derive from the conversion of Ni^{2+} to Ni^{3+} under oxygen-rich conditions [38].

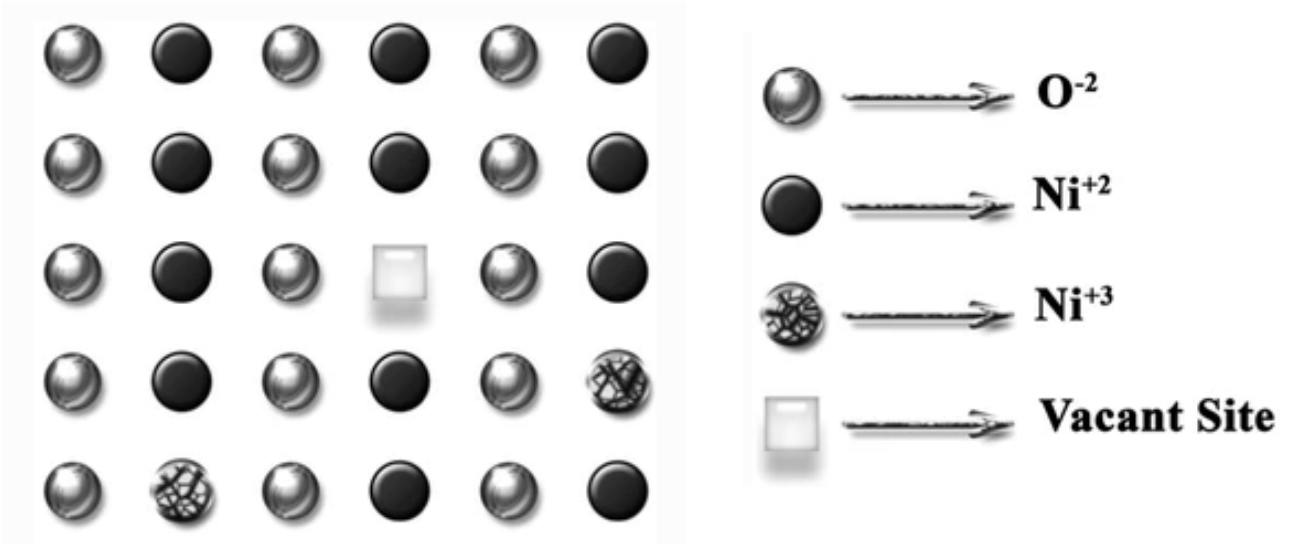

Figure 3.1: Schematic diagram showing cation vacancies trapping positive holes (p) in non-stoichiometric NiO.

Numerous synthetic methods for production of NiO thin films have been reported thus far including the sol-gel method [59], Pulsed Laser Deposition (PLD) [3], Molecular Beam Epitaxy (MBE) [39], magnetron sputtering [46], chemical bath deposition [50] and evaportaion [28].

Most would argue that the favoured synthetic method is the magnetron sputtering due to its high deposition rate, good controllability in the chemical composition, reproducibility and excellent uniformity over a large area of deposition. In a great work by S.-C. Chen, et al. [9] NiO thin films were deposited by direct current magnetron sputtering (DCMS) and high power impulse magnetron sputtering (HiPIMS) at various oxygen flow ratios. The results show that the high ionization rate of HiPIMS facilitates the formation of Ni^{3+} in the films. This can in turn produce high concentrations of nickel vacancies and holes, which is advantageous for improving the p-type conductivity of the NiO films. This is because Ni^{2+} vacancies as well as interstitial oxygen can be easily introduced under oxygen-rich conditions. These defects are beneficial to raise the film's carrier concentration, but are impedimental to the film's carrier mobility.

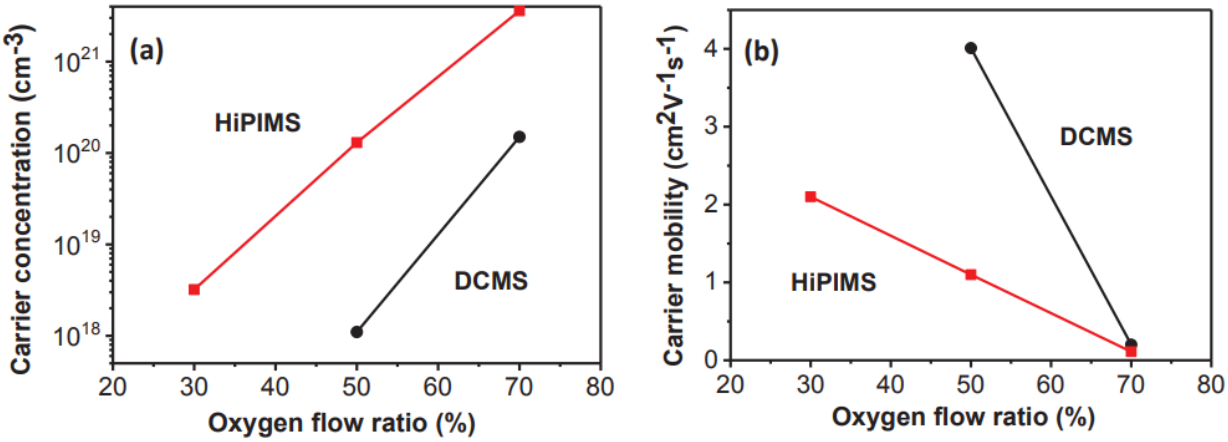

Figure 3.2: The carrier concentration (a) and the carrier mobility (b) of NiO films deposited by DCMS and HiPIMS at various oxygen flow ratios.

Meanwhile, the film's transmittance, whose role will be explained in the following chapters, in the visible region degrades due to the scattering of the incident light by the defects.

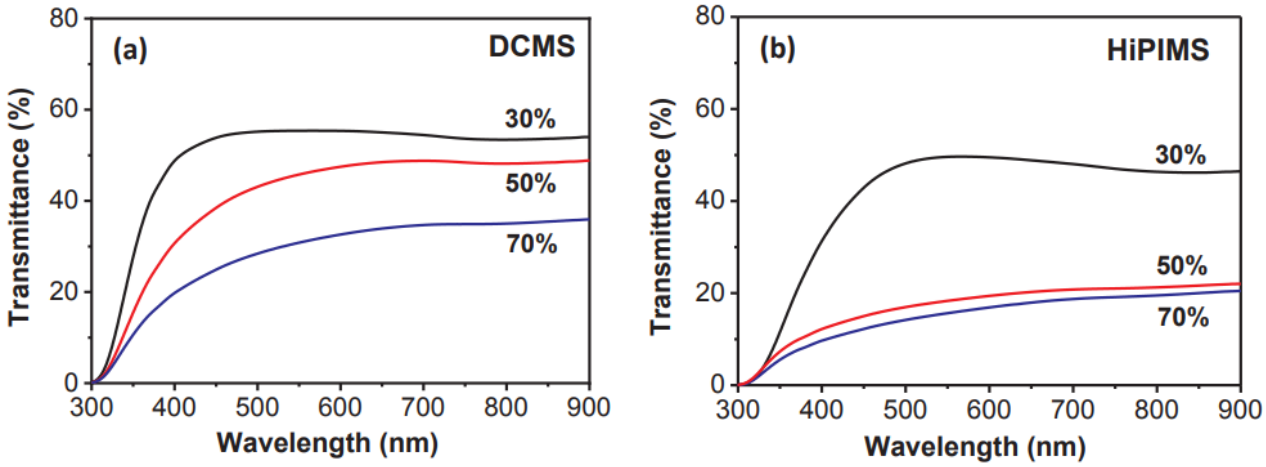

Figure 3.3: The transmittance of NiO films deposited by DCMS (a) and HiPIMS (b) at various oxygen flow ratios.

3.2 Sensing characteristics of NiO

As mentioned in the previous section, there is a wide range of applications in which NiO is being used. Nevertheless, in this thesis we will be focusing on the projects regarding gas sensing. NiO is used either by itself, in most cases, as a thin film or with other composites in order to detect a target gas. In the following line we will be presenting both of these cases using some interesting projects.

A noteworthy project of NiO thin films being used for gas sensing, and specifically ammonia gas sensing, has been published by K. Kanga Reddy and M.V. Ramana Reddy [22]. Nickel oxide thin films have been prepared using cost-effective sol-gel spin deposition technique, where a solution containing the appropriate reactants was deposited upon glass substrates which in term were annealed at 250^{o}C. The thin film gas sensor was fabricated by pasting a pair of two silver electrodes 4mm apart, on the top of the prepared NiO film and heated with the help of a hot plate at 100^{o}C for 1 hr. The array used was similar to what will be adequately explained in future chapters of this thesis. The reason this project was selected to be presented was the encouraging results being derived even though the deposition technique was simple and inexpensive. It is, also, possible to prepare the samples in a larger area and control the growth of thin films with ease. Due to ammonia being a reducing gas and NiO being a p-type semiconductor, the current flowing through the specimen is reduced when the sensors comes into contact with the gas.

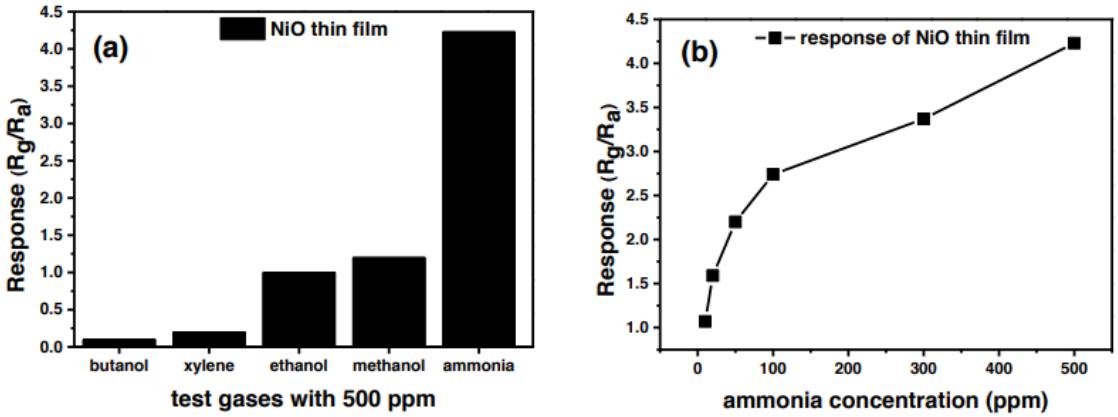

Figure 3.4: (a) Selectivity of nickel oxide thin film gas sensor towards various test gases with concentration 500 ppm and (b) Response of sensor towards different concentrations of ammonia.

The other gases shown in Figure 3.4 were used as they are reducing gases, similar to ammonia and clear selectivity amongst them is being showcased. Another key feature being shown is the characteristic plateau that can be distinguished in the amperometric measurements.

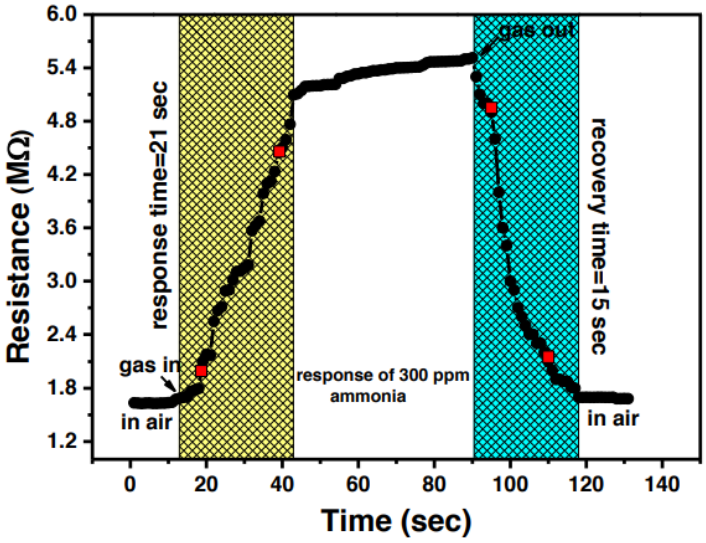

Figure 3.5: Response and recovery transients of nickel oxide thin film gas sensor towards ammonia with concentration 300 ppm.

Nevertheless, encouraging results have also been reported by P. Hao, et al. [24], in a paper where the construction of porous $LaFeO_3$ microspheres decorated with NiO nanosheets for high response ethanol gas sensors, was reported showcasing that NiO could also work in unison with other compounds. The reason behind this architecture was stated to be that this kind of morphology effectively improves the contact area between metal oxides and the target gases. Figure 3.6 presents SEM and EDS images of the final product.

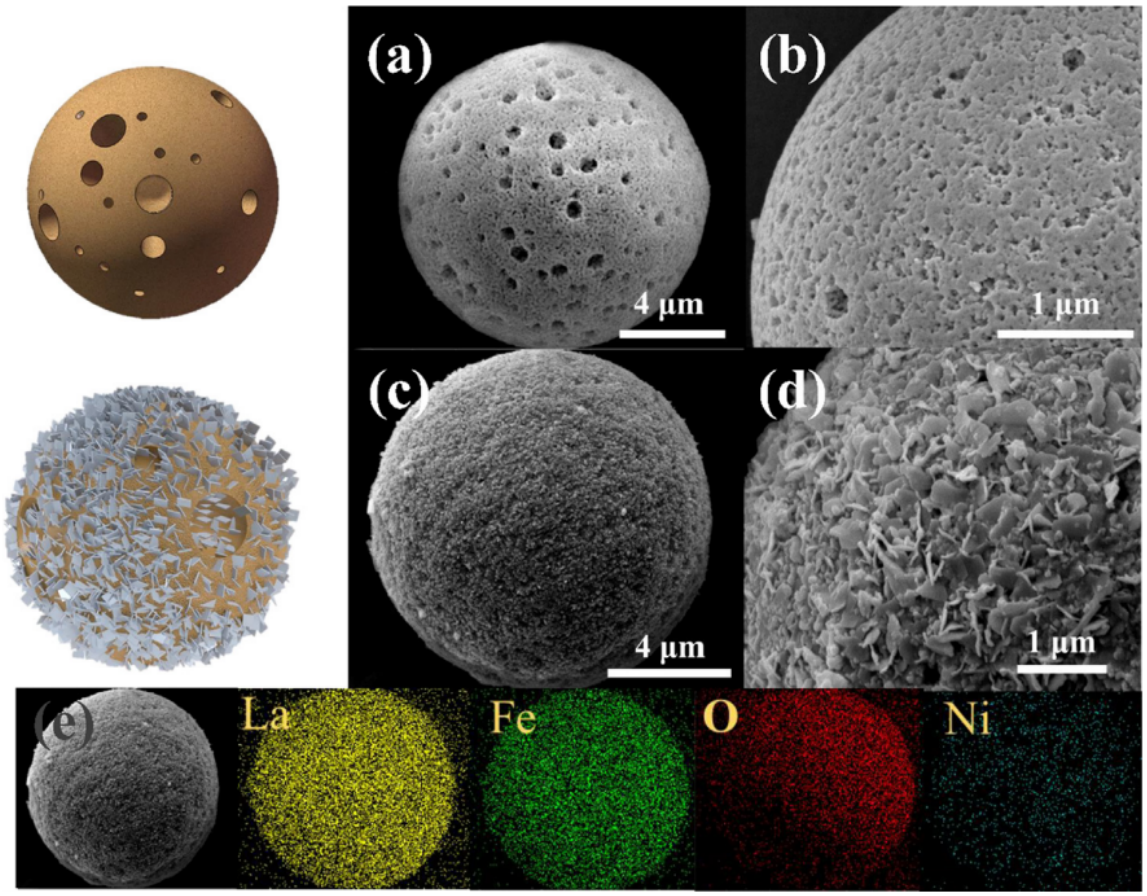

Figure 3.6: SEM images of (a-b) porous LaFeO3 microspheres, and (c-d) NiO@LaFeO3 nanocomposites. (e) EDS elemental mapping images of NiO@LaFeO3 nanocomposites (La, Fe, O and Ni).

As with most projects regarding gas sensing, the measurements consisted of figuring out the optimal working temperature, comparing the effectiveness of the new compound with the previously used specimen (namely NiO@$LaFeO_3$ and $LaFeO_3$ respectively), measure the sensitivity of the new material at different concentrations in comparison to the old one and lastly addressing the selectivity of the new sensor.

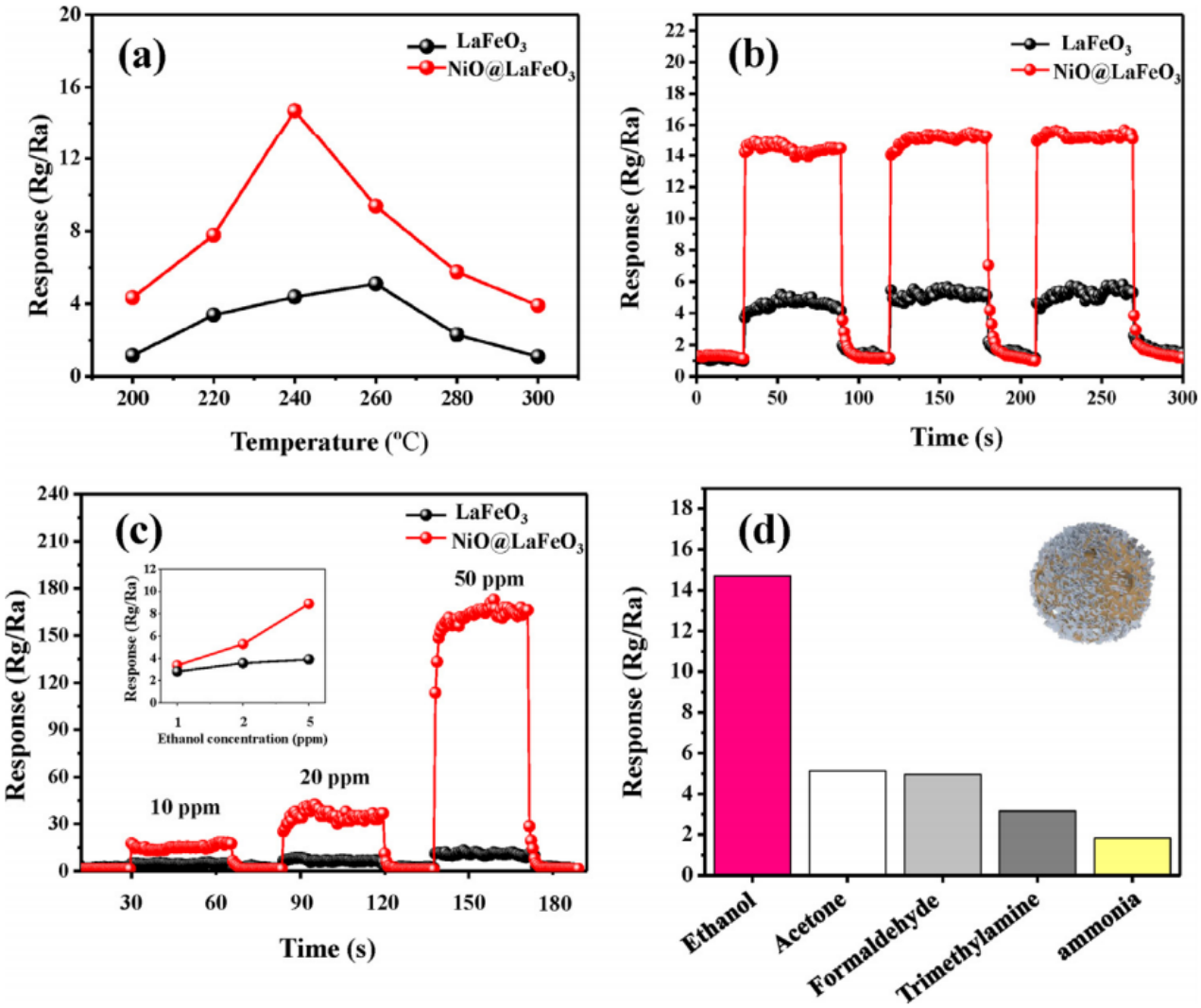

Figure 3.7: . (a) Response of pure $LaFeO_3$, $NiO@LaFeO_3$ nanocomposites at various operating temperatures to 10 ppm ethanol. (b) Response and recovery curves and the stability of the sensors based on pure $LaFeO_3$, $NiO@LaFeO_3$ nanocomposites against 10 ppm of ethanol. (c) Dynamic response curves of pure $LaFeO_3$, $NiO@LaFeO_3$ nanocomposites in ethanol of different concentrations (10–50 ppm) at 240 °C. Inset: Response of pure $LaFeO_3$, $NiO@LaFeO_3$ nanocomposites in ethanol of different concentrations (1–3 ppm) at 240 °C. (d) Sensor response of pure $LaFeO3_3$, $NiO@LaFeO_3$ nanocomposites toward 10 ppm ethanol, acetone, formaldehyde, trimethylamine and ammonia at 240 °C.

All the aforementioned experiments that were carried out by P. Hao, et al. are shown in Figure 3.7. The results of this project clearly lead the reader to the conclusion that not only does NiO functions adequately as a gas sensor on its own, but it also has the ability to enhance other compounds, effectively making it one of the most useful and versatile compounds the scientific community has to offer. Even more impressive is the fact that P. Hao, et al. argue that NiO is working as a catalyst in this collaboration of the two compounds.

3.3 Physical/Chemical characteristics of aluminum doped NiO

As stated in previous chapters, the doping of semiconductors is a widely used technique that results in the diminution of the energy needed to create carriers of electricity, be it electrons or holes. A widely used dopant of NiO is Aluminum (Al) and it is the one that is used in this thesis.

When dealing with doping one must always expect some changes in the morphology of the original specimen post doping. For example, C. Feng et al. [20] noted that, in the process of creating nanofibers of Al doped NiO to be used as gas sensors, the XRD peak intensity of the doped sample is lower than that of pure NiO, which indicates that doping Al can reduce the crystallinity. In the same work it is also reffered that when adding Al atoms into NiO, the morphologies of the samples changed significantly with nanoparticles decorated on the nanofibers. In addition, it is very interesting that Al doping effectively makes the specimen transparent, even though this depends on many factors such as thickness as well as other deposition parameters. E. Gagaoudakis et al. [21] showcase this in their project regarding Al-doped NiO prepared by radio frequency (rf) sputtering.

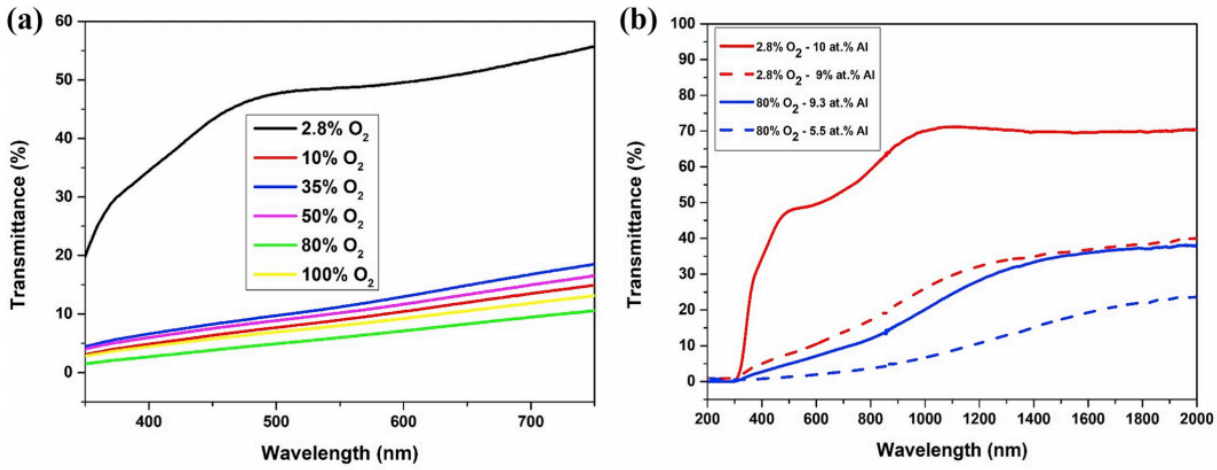

Figure 3.8: (a) Transmittance in the visible region of NiO:Al films (10 at.% Al) deposited on glass at different % oxygen in plasma. (b) Transmittance of NiO:Al films with different at.% of Al at 2.8% and 80% oxygen in plasma

3.4 Sensing characteristics of aluminum doped NiO

Aluminum doped NiO has not been used heavily in past years. Nevertheless there are some cases where researchers have used it to detect gases like Hydrogen, VOCs like methanol or methane and NOx like NO_2 [20, 21, 29, 49]. In the following Figure, a table will be presented listing some of the work that has been highlighted regarding Al:NiO as far as gas sensing is concerned.

Target gas	Optimal operating temperature	Deposition method	Morphology	Optimal percentage of Al doping	Ref.
Methanol	325ºC	Electrospinning	Nanofibers	3%	C. Feng et al.
Ethanol	200ºC	Sol gel immersion	Nanorod-flowers	2.15%	C. Wang et al.
NO_2	200ºC	RF sputtering	Thin films	5%	V. Kampitakis et al.
H_2	RT under UV irradiation	RF sputtering	Thin films	10%	E. Gagaoudakis et al.
Methane	RT under UV irradiation	RF sputtering	Thin films	10%	E. Gagaoudakis et al.

Figure 3.9: Reporting table of previous works regarding Aluminum doped NiO for gas sensing use.

As we can see most researchers use high operating temperatures that correlate with scientific literature for metal oxide gas sensors, nonetheless, there have been instances of adequate sensing capabilities in room temperature. This thesis attempted to test such specimens for O_3 gas sensing as it has not yet been reported or meticulously examined as a target gas.

4 Experimental section

Before diving any deeper into the experimental section, the overview must be presented in order to clear things out for the reader. Using RF sputtering, 9 different specimens were grown, with the key differences being the content of oxygen in the induced Ar–O_2 plasma gas mixture and the thickness of each specimen being unique. This O_2 content varied and its values were 4% (S1743-44-45), 2.8% (S1746-47-48) and 2% (S1749-50-51).

Percentage of O_2 in plasma	Specimen code	Thickness (nm)
4%	S-1743	167.5 ± 2.5
	S-1744	95.5 ± 1.5
	S-1745	52.0 ± 12.0
2.8%	S-1746	168.7 ± 7.2
	S-1747	108.0 ± 11.0
	S-1748	61.5 ± 0.5
2%	S-1749	160.3 ± 4.3
	S-1750	90.0 ± 16.3
	S-1751	69.5 ± 4.7

Figure 4.1: Percentage of O_2 present in the plasma during deposition and thickness(nm) of each specimen.

Out of these 9 specimens we selected to use, in the gas sensing measurements, the three thicker ones, namely S1743-S1746-S1749. The specimens were examined by XRD, FESEM and the optical properties were studied by a spectrophotometer, all of whom will be thoroughly explained later on.

4.1 X-Ray Diffraction

One of the most widely spread techniques for studying and analyzing a specific material is the X-Ray Diffraction (XRD) technique. It is based on the ability of crystals to diffract X-rays in a characteristic, to a specific state, manner allowing us to precisely study the crystalline phases. A common plot you would get from an X-ray diffraction technique, is a line with peaks

of different widths and heights with some background noise. Studying the characteristics of a peak, such as position or intensity, we can derive a myriad of helpful information about our material.

Generation of X-rays

The generation of these X-rays is generally achieved through sealed tubes, rotating anodes or synchrotron radiation sources. In laboratory equipment sealed tubes and rotating anodes are mostly used and they both produce X-rays by the same principle. Firstly, we produce an electron ray by accelerating electrons through a high potential field, directed to a target that when hit produces the X-rays. These electrons are generated by heating a tungsten filament in a vacuum. Then, the incident electrons induce the following effects that lead to the generation of X-rays. The first is the production of photons by decelerating electrons, thus generating a continuous distribution of wavelength, known as Bremsstrahlung. The second is the ionization of the impinged atoms by ejecting electrons from the inner shells. In order to get a more stable state, electrons from outer shells “jump” into these gaps. The difference between the electron energies of the inner shell and of the incoming electron is emitted in the form of photons, with a characteristic energy depending on the initial and final shell position of the electrons and on the material. The radiation coming out of a sealed tube or a rotating anode is therefore a super-imposition of a continuous spectrum and of characteristic radiations, though XRD methods only use the characteristic radiation with the highest intensity, the K_α radiation, and remove most of the remaining radiation by using appropriate filters or monochromators. According to the filter material, the absorption edge is situated at a different wavelength allowing a strong absorption of the continuous spectrum as well as of the K_β radiation while letting most of the K_α intensity passing through. There are appropriate filter materials for all targets.

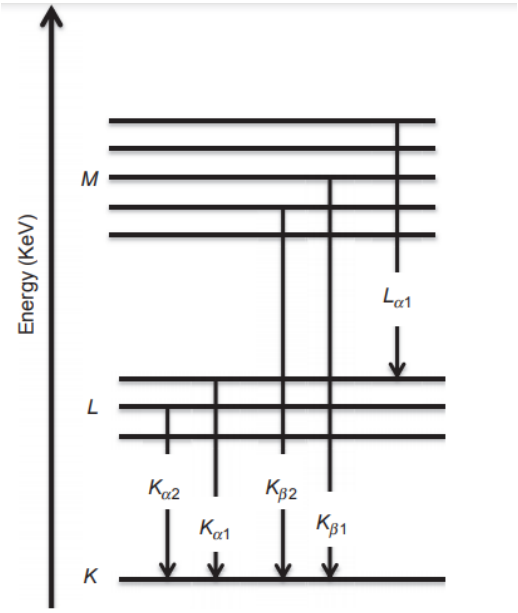

Figure 4.2: Schematic representation of the atomic energy levels and emission of characteristic X-ray radiation

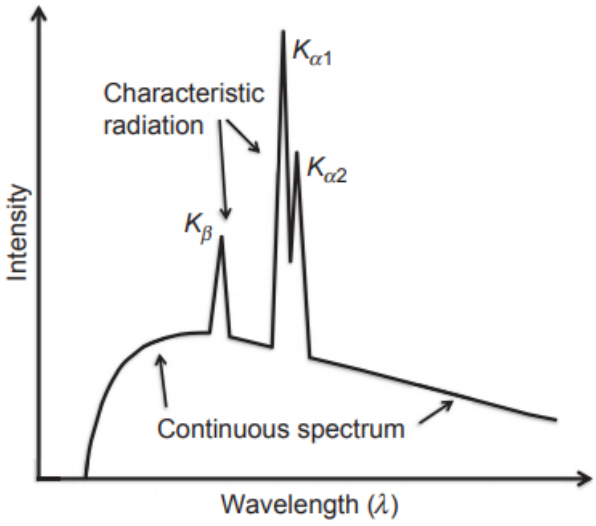

Figure 4.3: Intensity over wavelength distribution of the X-ray radiation produced by a sealed-tube showing the continuous and the characteristic spectrum.

Diffraction of X-rays by crystalline materials

Although they will not be talked about in the project, it's crucial to point out that when X-rays reach matter, several kinds of interactions can take place leading to different absorption and scattering effects. Between the electrons surrounding the atomic nuclei and the incident photons, the famous Rayleigh scattering occurs. Rayleigh scattering is the predominantly elastic scattering of light or other electromagnetic radiation by particles much smaller than the wavelength of the radiation. In this case, the incident wave has the same energy and phase as the scattered one. As a consequence, the X-ray photons impinging on all atoms of an irradiated volume are scattered in all directions, but due to the periodic nature of the crystalline structure of the material being studied, constructive or destructive interference will occur, resulting in a characteristic diffraction phenomena which can be studied to investigate the crystal structure of materials.

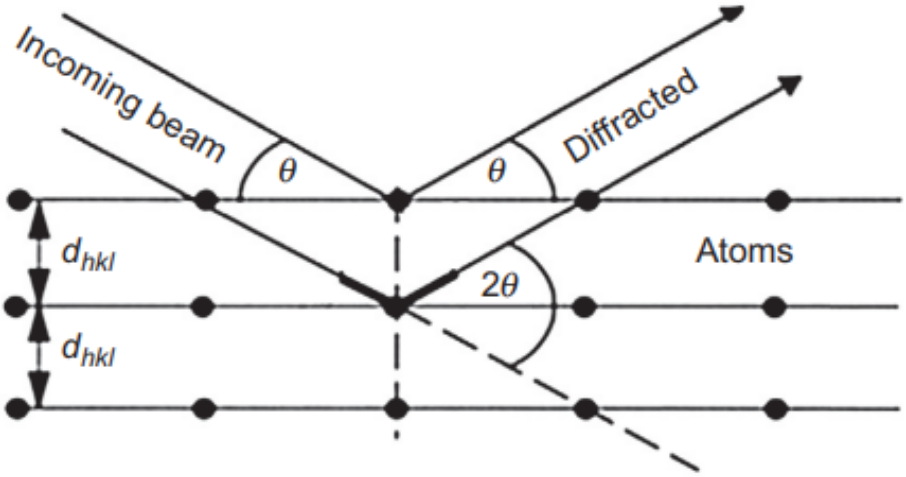

Figure 4.4: Geometrical condition for diffraction from lattice planes.

The principle of the methods is based on the diffraction of X-rays by periodic atomic planes and the angle or energy-resolved detection of the diffracted signal. The geometrical interpretation of the XRD phenomenon (constructive interference) has been given by W.L. Bragg. Figure 4.4 gives the details about the geometrical condition for diffraction and the determination of Bragg's law which is described in the following equation.

$$n\lambda = 2d_{\text{hkl}}sin(\theta) \tag{4.1}$$

In the equation *n* is the order of diffraction, *λ* is the wavelength of the incident beam in nanometers, d_{hkl} is the lattice spacing in nanometers and *θ* is the angle of the diffracted beam in degrees.

The total diffracted intensity for a lattice plan family ($I_{(hkl)}$) depends on several factors. These terms are combined to obtain an expression describing the total intensity at any 2θ position.

$$I_{(hkl)} = K \times |F_{(hkl)}|^2 \times f_\alpha e^{\frac{-Bsin^2(\theta)}{\lambda^2}} \times A \times L(\theta) \times P(\theta) \times m \tag{4.2}$$

The diffracted intensities $I_{(hkl)}$ are directly proportional to the square of the crystallographic structure factor $F_{(hkl)}$, which is a complex quantity with an equation of

$$F_{(hkl)} = \sum_{j=1}^{N} f_j \times exp[2\pi i \times (hx_j + ky_j + lz_j)] \tag{4.3}$$

with f_j being the atomic scattering factor of atom *j*, *hkl* being the Miller indices of diffracting planes and *xyz* the relative atomic position in the unit cell. The summation of *j* runs through all the atoms in a unit cell. According to the crystal symmetry, different extinctions of interferences will occur, leading to different diffraction patterns. For example, in the case of body-centered lattices, diffraction occurs if the condition *h+k+l=2n* is satisfied, while in face-centered lattices, the condition *h+k,h+l,k+l=2n* has to be satisfied. Circling back to the intensity $I_{(hkl)}$, *K* is a constant independent of 2θ, $f_\alpha e^{\frac{-Bsin^2(\theta)}{\lambda^2}}$ is the factor describing the average displacement of atoms from their mean position due to temperature, *A* the absorption factor, *L(θ)* the Lorentz factor which is equal to $\frac{1}{sin(2\theta)}$, *P(θ)* the polarization factor which is equal to $\frac{1+cos(2\theta)}{2}$ and *m* the multiplicity describing the number of equivalent planes that can diffract at a given Bragg angle.

After all is said and done, diffraction data is represented in a plot of intensity as a function of the 2θ angle. The information content that can be extracted is represented in the coming figure.

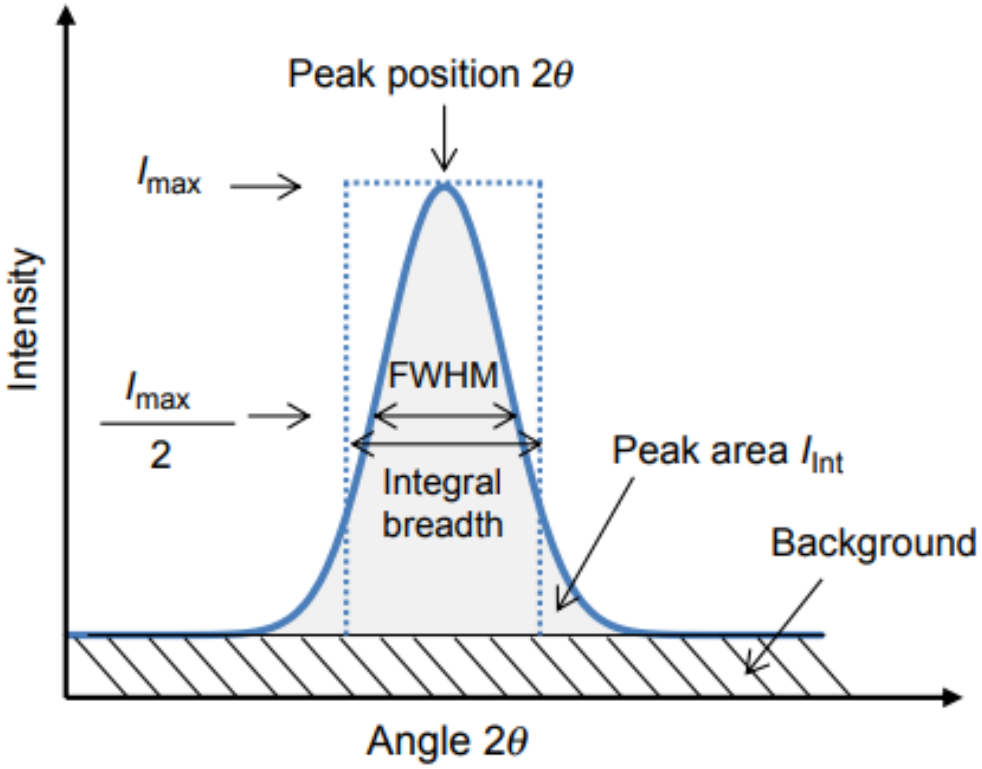

Figure 4.5: Diffraction peak and information content that can be extracted.

As mentioned above, different lattice planes have different diffraction conditions, and varying intensities of the diffracted signal occur according to the crystal structure and space group of the present phases. As a consequence, each phase produces a characteristic diffraction pattern that allows its identification. Moreover, when several phases are present in a system, the characteristic patterns of all phases are superimposed and the intensity of the diffraction peaks of the phases are respectively proportional to their amounts. Therefore, the XRD method is widely used for the identification of present phases (qualitative analysis) and for the determination of their respective amounts (quantitative analysis).

Last but not least, we will be talking about Scherrer's equations, which is a mathematical formula that is used repeatedly in the scientific community. The reason being that it determines the mean size of nano crystallites in nano crystalline bulk materials. Crystallite size:

$$\tau_{\text{XRD}} = \frac{K \times \lambda}{\beta \times cos(\theta)} \tag{4.4}$$

where K is the Scherrer constant related to crystallite shape, normally taken as 0.9, λ is the X-ray wavelength, β is the FWHM (full-width at half-maximum), and θ is the Bragg angle. [17]

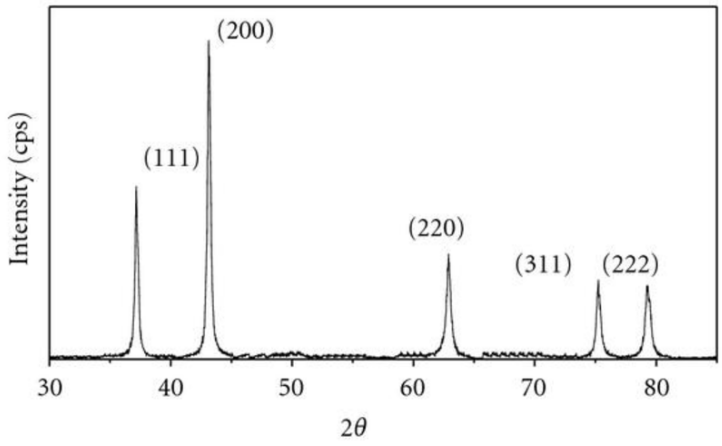

Figure 4.6: Typical XRD pattern of NiO nanoparticles.

In this thesis the different specimens were investigated using a PANalyticalEmpyrean diffractionometer equipped with Cu-LFF (λ=1.5406 Å) X-rays source, scanning in the range of 20°-90°.

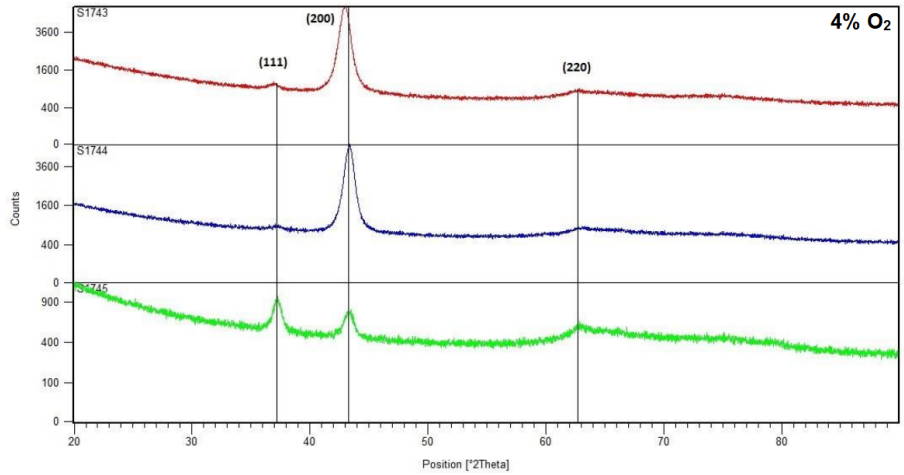

Figure 4.7: XRD pattern of specimens S1743-44-45(4% O_2 in plasma)(167.5 nm, 95.5 nm, 52.0 nm) showing the three main lattice plains (111, 200, 220) presented as a typically retrieved XRD spectra.

4.2 Scanning Electron Microscopy

S.E.M. or scanning electron microscopy is one of if not the most versatile method in a scientist's arsenal for the characterization of the chemical composition or the examination and analysis of the microstructure morphology of a material. In order to get a firm grip on its basic principles of operation and the principles of electron microscopy in general, one has to familiarize one's self with the basics of light optics.

To begin with, the unaided eye can discriminate objects subtending about 1/60˚ visual angle, corresponding to a resolution of 0.1 mm (at the optimum viewing distance of 25 cm). Taking a step further, optical microscopy has a resolution of up to 2,000 Å by enlarging the visual angle through optical lens. Electron microscopy uses high energy electron beams instead of a simple light source. Resolution as a physical quantity is defined as the minimum distance by which two structures could be separated and still be distinguishable from each other. The limit of resolution is dependent on the wavelength of the illumination source as proven by Ernst Abbe. At a certain wavelength, when the resolution exceeds its limit the image becomes blurred.

Due to phenomena such as diffraction and interference, a light beam cannot be focused as a perfect dot. What we see is a disc with a larger diameter than the source that has concentric rings surrounding it with diminishing intensities. This in known as an Airy disc. The primary wave front contains approximately 84% of the light energy, and the intensity of secondary and tertiary wave fronts decay rapidly at higher orders. The radius of an Airy disc is defined as the distance between the first-order peak and trough. Two objects can be distinguished from each other when their respective first order peaks have a distance equal to or greater than the radius of the Airy disc.

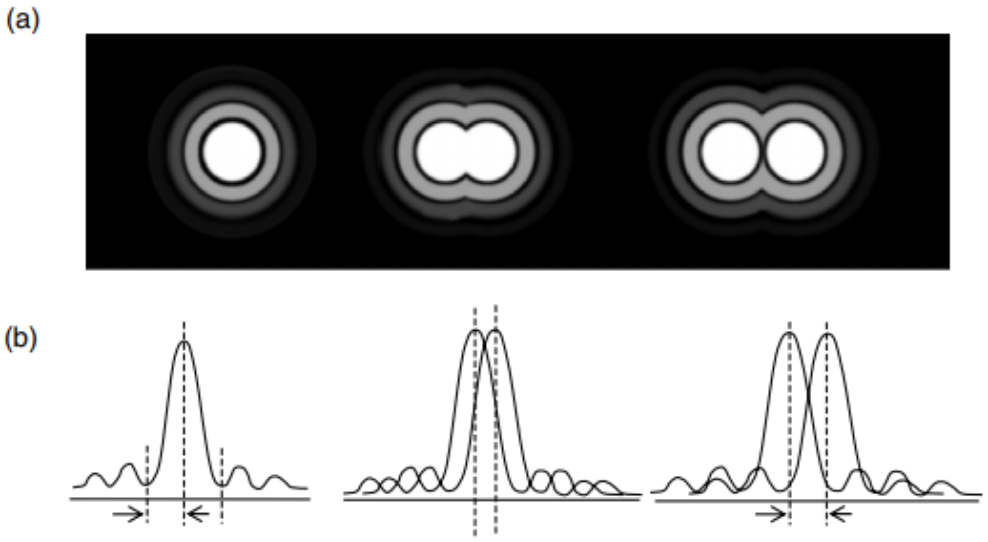

Figure 4.8: Illustration of resolution in (a) Airy disk and (b) wave front.

Abbe's equation can describe mathematically the resolution in a perfect optical system:

$$d = \frac{0.612\lambda}{nsin(\alpha)} \tag{4.5}$$

where *d*=resolution, *λ*=wavelength of imaging radiation, *n*=index of refraction of medium between point source and lens, relative to free space, *α*=half the angle of the cone of light from specimen plane accepted by the objective (half aperture angle in radians). In optics *n*sin(α)* is often referred to as Numerical Aperture (NA). NA of an optical system is a dimensionless number that characterizes the range of angles over which the system can accept or emit light. By incorporating index of refraction in its definition, NA has the property that it is constant for a beam as it goes from one material to another, provided there is no refractive power at the interface.

If we substitute the illumination source and the condenser lens in light microscopes with an electron beam and electromagnetic coils, respectively, we can construct the first Transmission Electron Microscope (TEM), that was built in the 1930s', that focused the electron beam onto the specimen plane using electromagnetic condenser lenses.

On the other hand, the general principle of a SEM is that it utilizes a focused electron beam to

scan across the surface of the specimen systematically, producing large numbers of signals, which will be discussed later. These electron signals are eventually converted to a visual signal displayed on a cathode ray tube (CRT). As mentioned above, image formation in the SEM is dependent on the acquisition of various signals produced from interactions between the specimen and the incident electron beam. These interactions can be divided into two major categories: elastic interactions and inelastic interactions.

Elastic scattering results from the deflection of the incident electrons by the specimen's atomic nucleus or by outer shell electrons of similar energy. Its characteristic is the negligible energy loss during the collision and a wide-angled directional change of the scattered electrons. Inelastic scattering occurs through a variety of interactions between the incident electrons and the electrons and atoms of the sample, that result in the primary beam electron transferring substantial energy to that atom. The amount of energy loss depends on whether the specimen electrons are excited singly or collectively and on the binding energy of the electron to the atom.

Regarding the aforementioned wide-angled directional change, incident electrons that are elastically scattered through an angle of more than 90˚ are called backscattered electrons (BSE), and yield a useful signal for imaging the sample. Taking energy loss into account, the excitation of the specimen electrons during the ionization of specimen atoms leads to the generation of secondary electrons (SE), which are conventionally defined as possessing energies of less than 50 eV and can be used to image or analyze the sample.

In addition to those signals that are utilized to form an image, a number of other signals are produced when an electron beam strikes a sample, including the emission of characteristic x-rays, Auger electrons, and cathodoluminescence, that will be discussed briefly later on.

Not all signals are detected from the same region. In most cases when incident an electron strikes the specimens' surface, instead of being bounced off immediately, they penetrate into the sample for some distance before they collide with a specimen atom. In doing so, the primary electron beam produces what is known as a region of primary excitation, from which the variety of signals are produced as shown in Figure 4.9 .

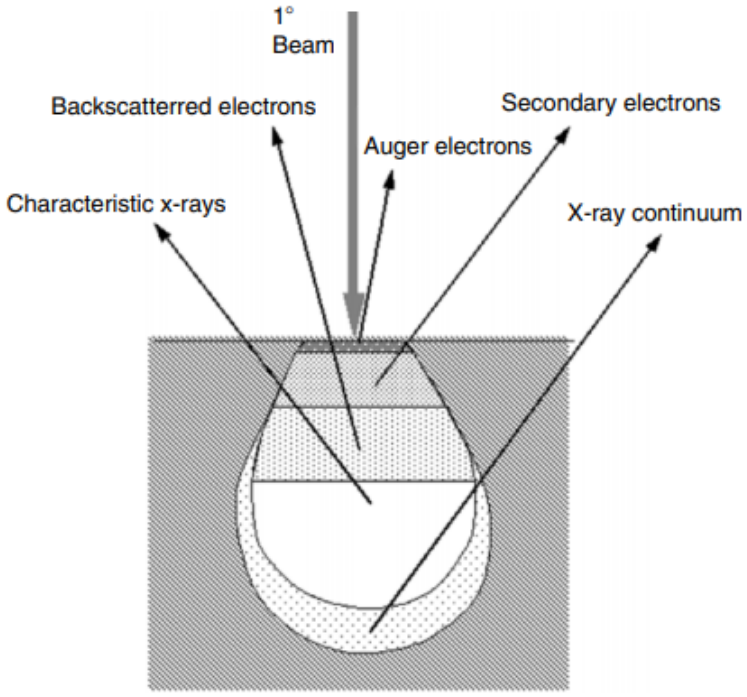

Figure 4.9: Illustration of several signals generated by the electron beam–specimen interaction in the scanning electron microscope and the regions from which the signals can be detected.

The size and shape of this region is mostly dependent on the energy of the electron beam and the atomic number, hence the density, of the specimen. At a certain accelerating voltage, the shape of the interaction volume is a “tear drop” for specimens of low atomic number and a hemisphere for specimens of high atomic number. The volume and depth of penetration expand with an increase of the beam energy and shrink as the atomic number decreases, because specimens with higher atomic number have more particles to stop electron penetration. One effect of the interaction volume on signal acquisition is that the use of a high accelerating voltage will result in a deep penetration length and a large primary excitation region, and ultimately cause the loss of detailed surface information of the sample.

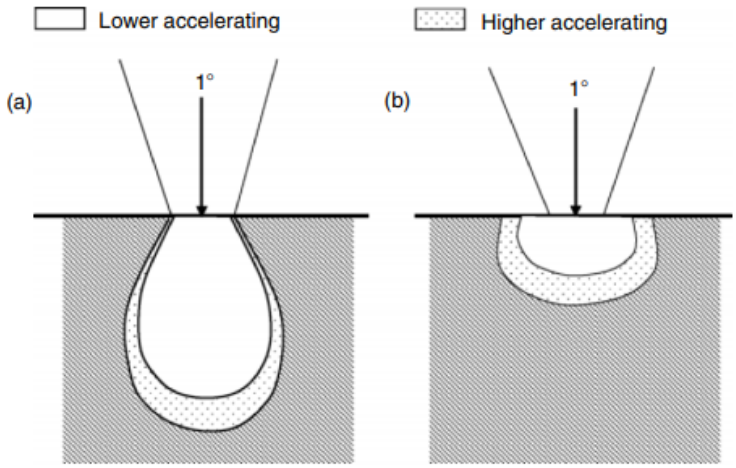

Figure 4.10: Influence of accelerating voltage and specimen atomic number on the primary excitation volume: (a) low atomic number and (b) high atomic number.

Secondary electrons

The most widely used signal produced by the interaction of the primary electron beam with the specimen is the secondary electron emission signal. When the primary beam strikes the sample surface causing the ionization of specimen atoms, loosely bound electrons may be emitted and these are referred to as secondary electrons. As they have low energy, typically an average of around 3–5 eV, they can only escape from a region within a few nanometers of the material surface. So secondary electrons accurately mark the position of the beam and give topographic information with good resolution. The topographical image is dependent on how many of the secondary electrons actually reach the detector that carries some applied bias. The standard collector for secondary electrons in most SEMs is called Everhart– Thornley (ET) detector and applies both a bias (+10 kV) to the scintillator and a lower bias (+300 V) to the Faraday cage, which screens the detector. Then, the scintillator converts the electron energy to photons (visible light). The photons produced travel down a Plexiglas or polished quartz light pipe and move out through the specimen chamber wall, into a photomultiplier tube (PMT) which converts the quantum energy of the photons back into electrons. The output voltage from the PMT is further amplified before being output as brightness modulation on the display screen of the SEM. A secondary electron signal can resolve surface structures down to the order of 10 nm or better. Secondary electrons that are prevented from reaching the detector will generate shadows or be darker in contrast than

those regions that have an unobstructed electron path to the detector.

Backscattered electrons

The detection of backscattered electrons is another valuable method of producing an image in SEM, which provide both compositional and topographical information. Roughly 10–50 percent of the beam electrons are backscattered toward their source, and on an average these electrons retain 60–80 percent of their initial energy. In specimens with high atomic number a greater number of BSEs is produced because of the extra positive charges in the nucleus, thus resulting in a more intense signal. Thus, SEM images provide atomic number contrast. The region of the specimen from which BSEs are produced is considerably larger than it is for secondary electrons, due to the fact that BSEs have greater energy, which prevents them from being absorbed by the sample. And so, the lateral resolution of a BSE image is considerably worse (1.0 μm) than it is for a secondary electron image (10 nm). But with a fairly large width of escape depth, BSEs carry information about features that are deep beneath the surface. In examining relatively flat samples, BSEs can be used to produce a topographical image that differs from one produced by secondary electrons, because some BSEs are blocked by regions of the specimen that secondary electrons might be drawn around. In BSEs detectors there usually is a negatively biased Faraday cage to repel secondary electrons, resulting in an image produced by electrons travelling in a straight path from the specimen to the detector.

Characteristic X-rays

Yet another signal produced by the interaction of the specimen with the primary electron beam is characteristic x-rays. When an inner shell electron is displaced by collision with an electron from the primary beam, an outer shell electron may fall into the inner shell to reestablish the proper charge balance in its orbitals following an ionization event. Thus, the ionized atom returns to ground state, by emitting an x-ray photon. In addition to the characteristic x-ray peaks, the continuous background talked about in the XRD section is also being generated through the aforementioned process of decelerating high-energy electrons (Bremsstrahlung x-ray signal). This constitutes a background noise, and is usually stripped from the spectrum before analysis although it contains information that is essential to the proper understanding

and quantification of the emitted spectrum.

Auger electrons

As we saw in the generation of characteristic x-rays, when the incident primary electron beam displaces an inner shell electron from an atom, an outer shell electron takes its place. In the Auger effect, instead of emitting x-ray photons, the excess of energy is transferred to another electron, which is ejected from the atom; this second ejected electron is called an “Auger electron”. This electron has a characteristic energy and can therefore be used to provide chemical information. Because of their low energies, Auger electrons are emitted only from near the surface, due to having escape depths of only a few nanometers. They are principally used in surface analysis.

Cathodoluminescence

Following the interaction between the specimen and the primary electron beam, cathodoluminescence acts as a stabilizing mechanism that takes place when electrons recombine to fill holes made by the collision between electrons and atoms. In general, certain materials will release excess energy in the form of photons with infrared, visible, or ultraviolet wavelengths, similar to the emission of characteristic x-rays. These photons can be detected and counted by using a light pipe and photomultiplier similar to the ones utilized by the secondary electron detector. The best possible image resolution using this approach is estimated at about 50 nm. [60]

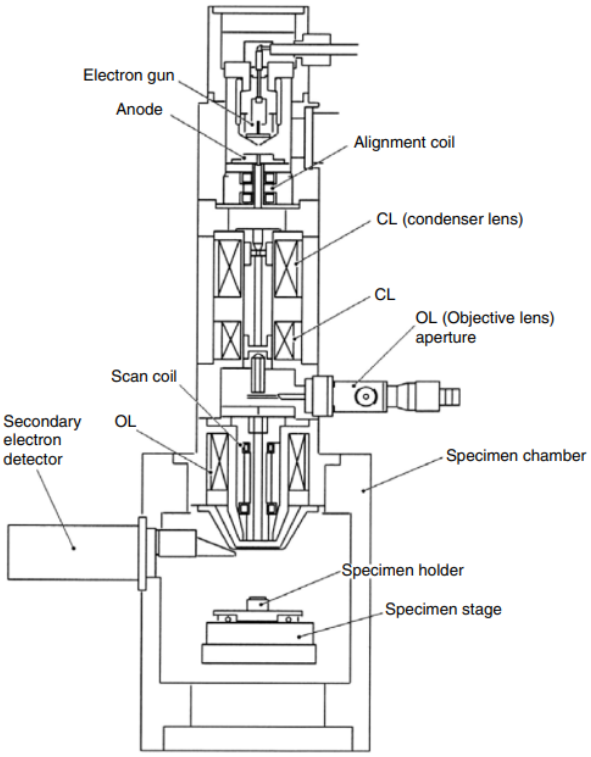

Figure 4.11: Schematic diagram of a scanning electron microscope (JSM—5410, courtesy of JEOL, USA).

The surface morphology of the specimens was examined by Field Emission Scanning Electron Microscopy (FESEM, Hitachi S570), equipped with an Energy Dispersive X-ray (EDX) spectrometry system.

4.3 Optical characterisation

Light spectroscopy

First things first, spectroscopy deals with the production, measurement, and interpretation of spectra arising from the interaction of electromagnetic radiation with matter. There is a wide variety of spectroscopic methods available for solving a broad range of analytical problems. The methods differ with respect to the species to be analyzed (such as molecular or atomic spectroscopy), the type of radiation-matter interaction to be monitored (such as absorption, emission, or diffraction), and the region of the electromagnetic spectrum used in the analysis. A very frequently used technique for characterizing thin films is Ultraviolet/Visible/Near Infrared (UV/Vis/NIR) absorption spectroscopy.

Its operational principle is quite simple. Light of a wavelength corresponding to the energy levels we want to achieve (in this project 250-2500 nm) is targeted towards a thin film specimen. The intensity of the beam is, then, measured in order to calculate the transmittance, or to put it blunter, the percentage of light that has been absorbed($T = \frac{I}{I_o}$). As a consequence of absorption and scattering effects, the incident beams are weakened along their path in the material. The intensity loss is exponential and follows the general law of Beer-Lambert:

$$I = I_o e^{-\alpha d} \rightleftharpoons e^{-\alpha d} = \frac{I}{I_o} \rightleftharpoons -\alpha d = \ln \frac{I}{I_o} \rightleftharpoons \alpha = -\frac{1}{d} \ln \frac{I}{I_o} \tag{4.6}$$

Having measured the initial beam intensity (I_o), the transmitted intensity (I) and the thickness of the absorbing layer (d), we can calculate the mass absorption coefficient (α). Using the following equation we use the Tauc plot [$(\alpha vh)^n$-hv] in order to extract the Energy gap of the semiconductor thin film.

$$(\alpha h v)^{\frac{1}{n}} = A(hv - E_g) \tag{4.7}$$

Whereas α=absorption coefficient, h=Planck's constant, v=the incident photon's frequency, E_g is the band gap and A is a proportionality constant. The value of the exponent denotes the nature of the electronic transition, whether allowed or forbidden and whether direct or indirect:

For direct allowed transitions n=1/2

For direct forbidden transitions n=3/2

For indirect allowed transitions n=2

For indirect forbidden transitions n=3

Typically the allowed transitions dominate the basic absorption processes, giving either n=1/2 or n=2, for direct and indirect transitions, respectively. Thus, the basic procedure for a Tauc analysis is to acquire optical absorbance data for the sample in question that spans a range of energies from below the band gap transition to above it. Plotting the $(\alpha hv)^{1/n}$ versus (hv) in most cases is a matter of testing n=1/2 or n=2 to compare which provides the better fit

and thus identifies the correct transition type. [48] The point where the linear fit intercepts the X-axis is the estimated Energy gap of our specimen (at Figure about 3.7 eV).

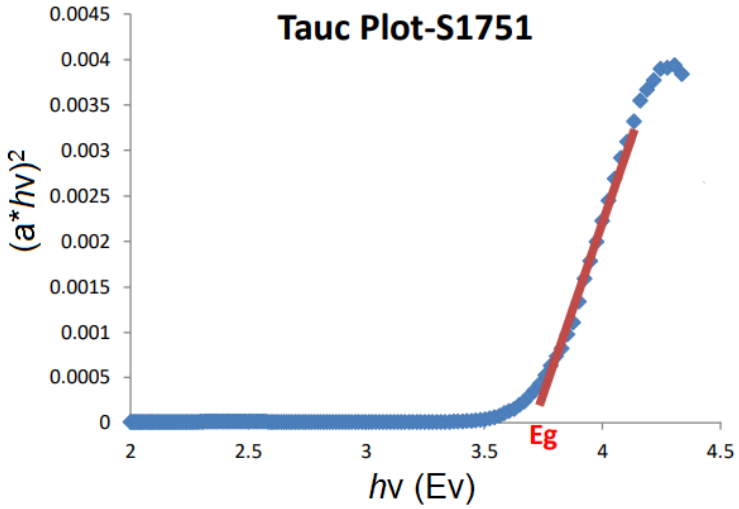

Figure 4.12: Example Tauc Plot from UV-Vis analysis of a Al:NiO thin film that illustrates the method of fitting the linear region to evaluate the band-gap at the X-axis intercept, here about 3.7 eV.

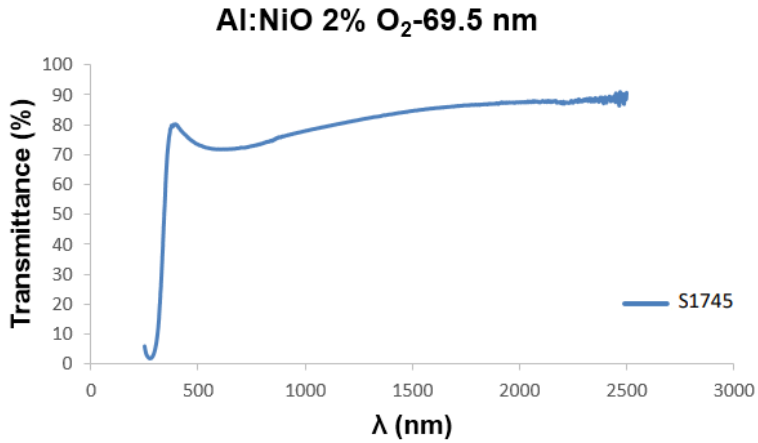

Figure 4.13: Transmittance spectra of specimen S1751 (2% O_2 in plasma, 69.5 nm)

The kind of spectra that is depicted in Figure 4.13 leads us to the Tauc plot, which is used to evaluate the band gap of the specimen.

Optical properties of the films were studied by a PerkinElmer Lambda 950 UV/Vis/NIR spectrophotometer, in the wavelength range of 250–2500 nm. The thickness of the films was measured by using a stylus profilometer (Veeco Dektat 150).

4.4 Gas sensing array

The gas sensing array for projects similar to this thesis is the different machines, devices and gas tanks that constitute one architectural structure, able to present to us the end result of our measurements. In this thesis, as depicted in Figure 4.15, the array is made up of:

1. The gas sensing device (in this case the IDE).
2. The gas chamber that fills with gases and inside which, the sensor is placed.
3. A tank of gas (or more tanks depending on the projects) that is filled with a specific gas which is used in the experiment (in this case, dry synthetic air) and is connected trough tubes to the gas chamber.
4. A pump that creates the vacuum needed to complete the experiment and suck the gases from inside the chamber to create flow.
5. An ozonator that is connected to the tank in order to take synthetic air and produce O_3 and the gas chamber so that it can be filled with said O_3.
6. Mass Flow Controllers that regulate the gas flow for both the O_3 and the synthetic air, as they are inserted into the gas chamber. Both MFCs are set up to 500 standard cubic centimeters per minute (sccm).
7. A temperature controller that is connected to the sensor and allows us to adjust the temperature of the specimen.
8. A Keithley 6517A electrometer that is connected to the sensor and the computer and plays the role of a mediator. This device depicts the value of the electric current, but also transports said value to the computer.
9. A computer which is connected to the Keithley device so that it can produce, via a specific programm, a plot of electric current vs time passed.

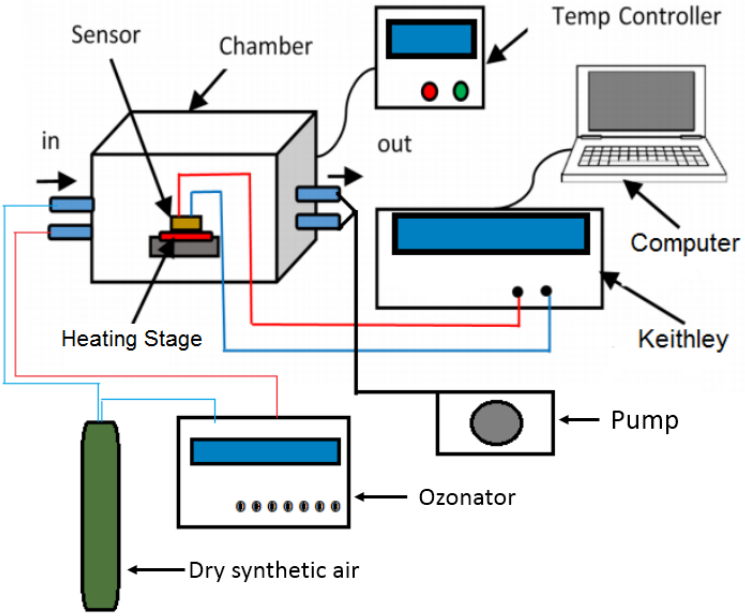

Figure 4.14: Gas sensing setup.

4.5 Inter-Digitated Electrodes or I.D.E.s

Inter-Digitated Electrodes or I.D.E.s are the base upon which most projects dealing with gas sensing using metal oxides are built. As depicted in Figure 4.14, IDEs are small devices that the sensing material is deposited on top of, in order to connect the electrodes, so that the electrical signal can reach our detector. Substrates of the IDE may vary in the material from which they are made but most use common glass for high temperature tolerance or some kind of organic compound (plastic) for elasticity. The vast majority of the electrodes are constructed from Platinum (Pt) or Gold (Au) due to their extremely low electrical resistance and the distance between each individual electrode varies from 5μm to 15μm depending on the need of the project. Due to them being inexpensive and easy to fabricate, IDEs have taken the scientific community by storm and they now stand as the predominant transducer in gas sensing projects. Through wires that connect the IDE (electrodes) and an electrometer, electrical signal is detected and depicted on a PC screen in relation to time passing.

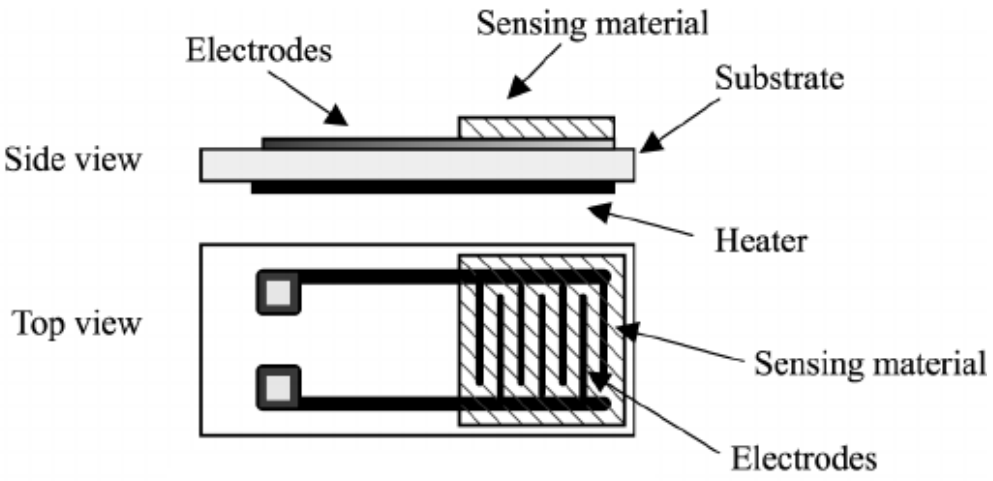

Figure 4.15: Schematic representation of a typical IDE.

4.6 Measurements

The experimental measurements carried out in this thesis were conducted for the first time, since there are no previous records of Aluminum doped Nickel oxide being used for the detection of O_3. Three different specimens of similar thickness (167.5, 168.7, 160.3 nm) were used, with the distinguishing feature being that they had different percentages of oxygen (4, 2.8, 2 %) inside the chamber during the deposition. Through the use of the gas sensing array seen in Figure 4.14, a controlled environment inside the chamber with a pressure of approximately 700 mbar was created, where synthetic air and ozone in different concentrations were alternated, in order to create gas cycles.

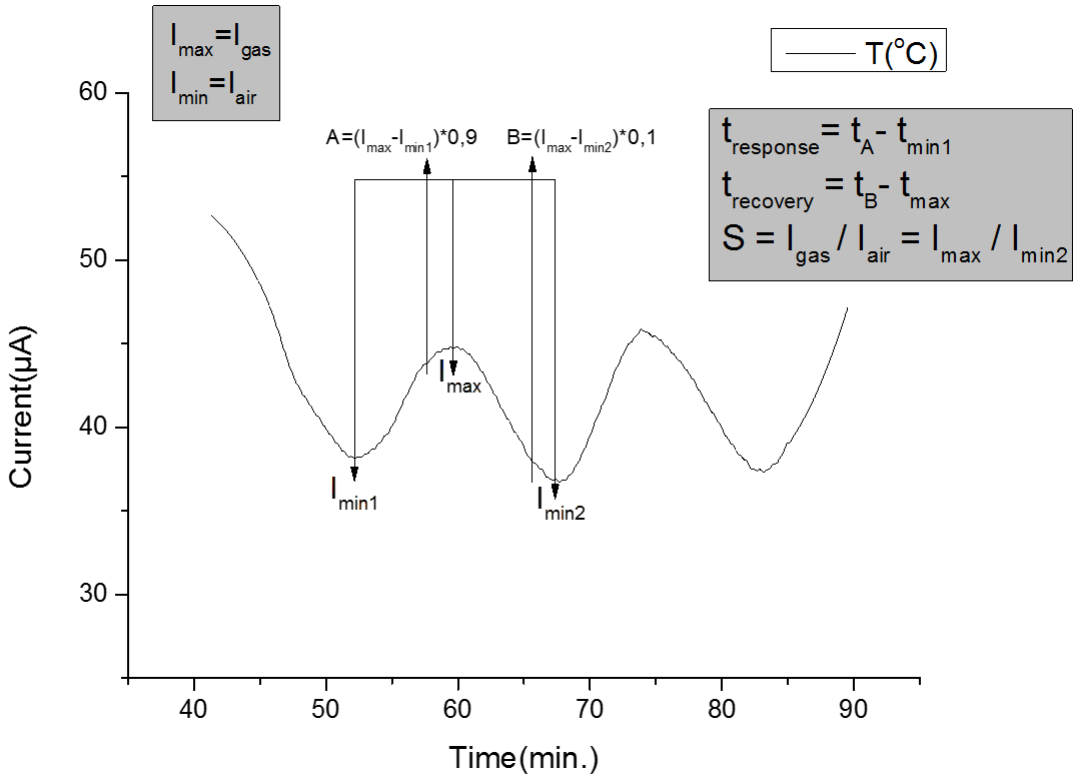

Figure 4.16: Schematic representation of a typical cyclical measurement and explanatory information about the upcoming calculations.

Due to ozone being a highly oxidizing gas and our semiconductor being p-type, during the time that ozone was present, the current flowing through the specimen got stronger creating peaks, but when synthetic air was present, valleys were created. Figure 4.16 is a schematic representation of one typical cyclical measurement and contains explanatory information about the upcoming results.

5 Results

5.1 Material Characterisation

As mentioned in the previous chapter Al:NiO films were analysed by three different techniques to study their structural, morphological and optical properties. Using an appropriate software the structure and lattice parameters of the films were determined by the XRD spectra shown in Figures (5.1, 5.2, 5.3). The patterns reveal that three lattice planes are present divulging the cubic structure of the material at hand. What is also evident is that whilst the thickness of the specimens gets smaller, the intensity of the main peak (200) also decline.

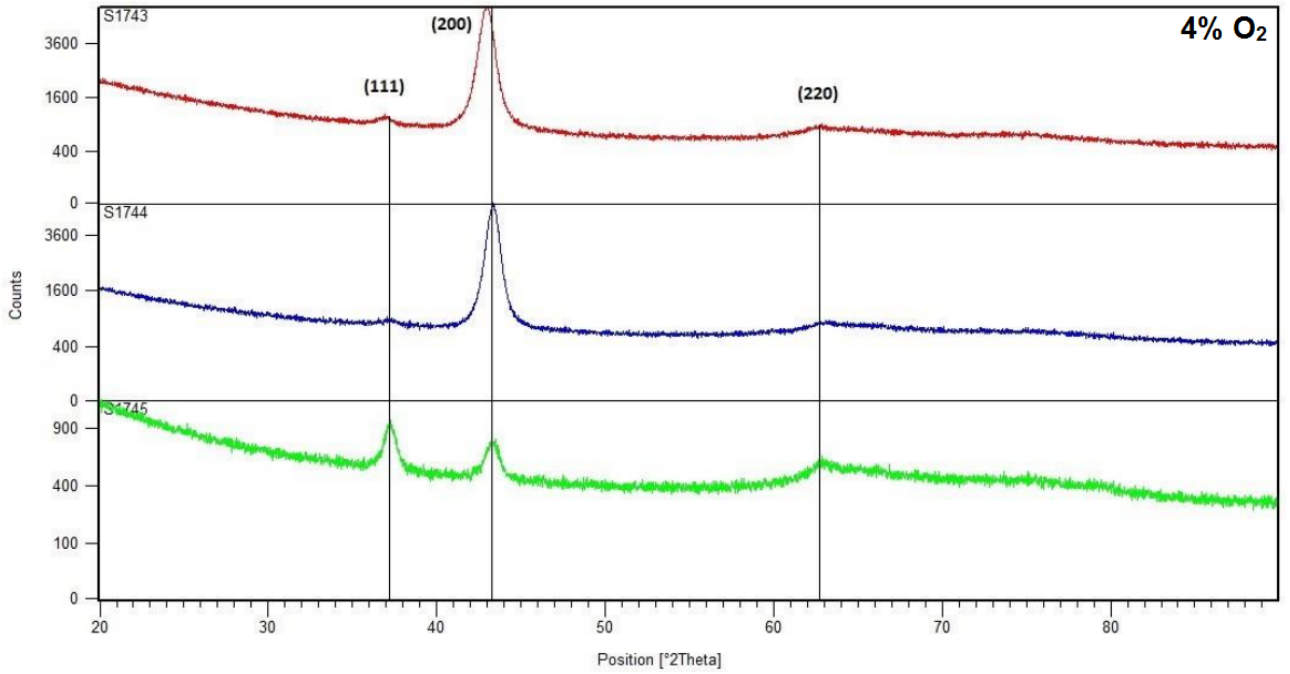

Figure 5.1: XRD pattern of specimens S1743-44-45 (167.5 nm, 95.5 nm, 52.0 nm) (4% O_2 in plasma) showing the three main lattice plains(111, 200, 220).

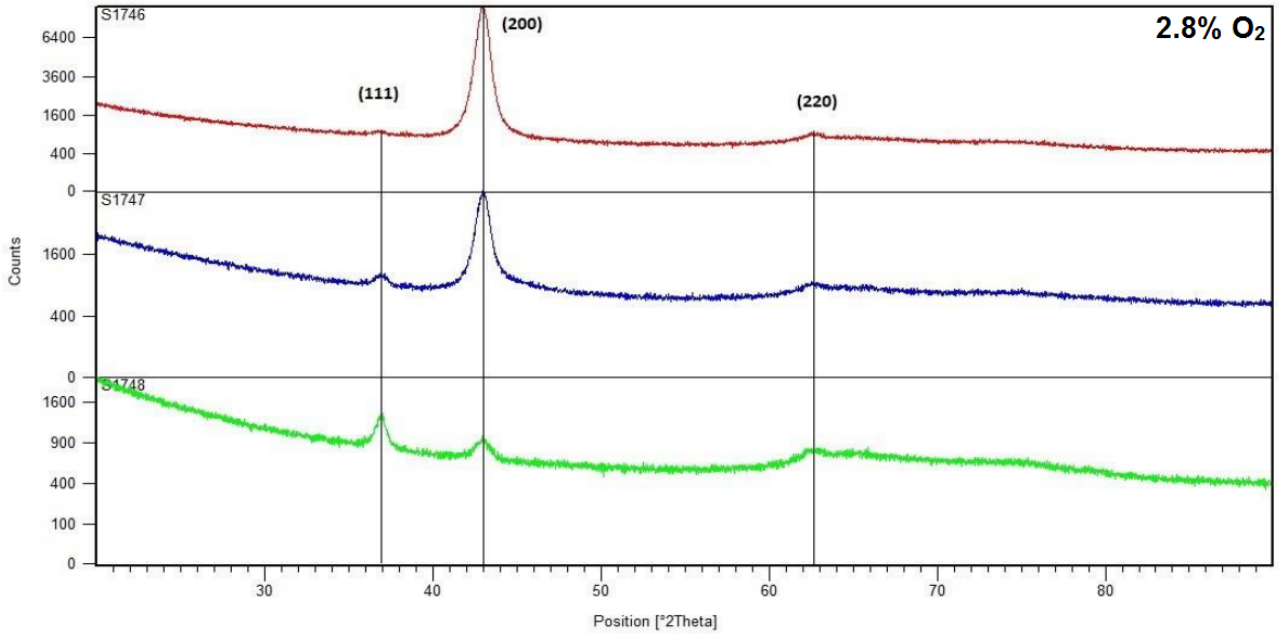

Figure 5.2: XRD pattern of specimens S1746-47-48 (168.7 nm, 108.0 nm, 61.5 nm) (2.8% O_2 in plasma) showing the three main lattice plains(111, 200, 220).

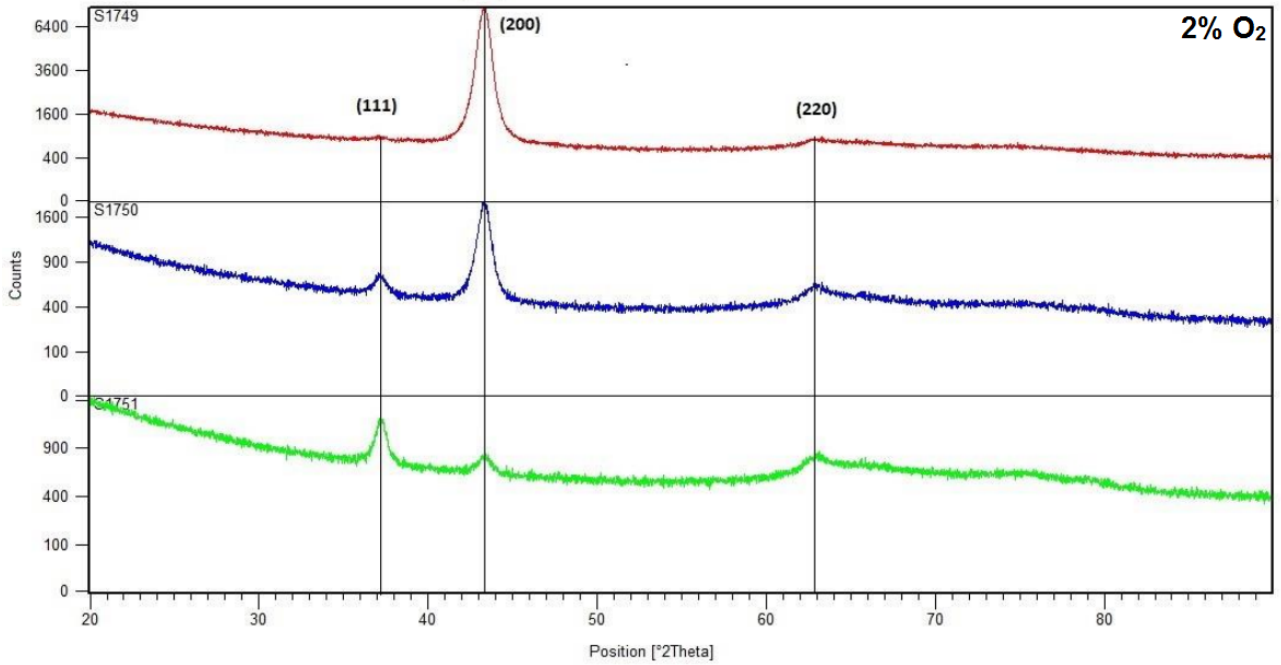

Figure 5.3: XRD pattern of specimens S1749-50-51 (160.3 nm, 90.0 nm, 69.5 nm) (2% O_2 in plasma) showing the three main lattice plains(111, 200, 220).

Knowing the angles of the peaks corresponding to the main lattice plains and their Full Width at Half Maximum, the crystallite size was calculated using Scherrer's equation (Eq. 4.4) shown in Chapter 4.

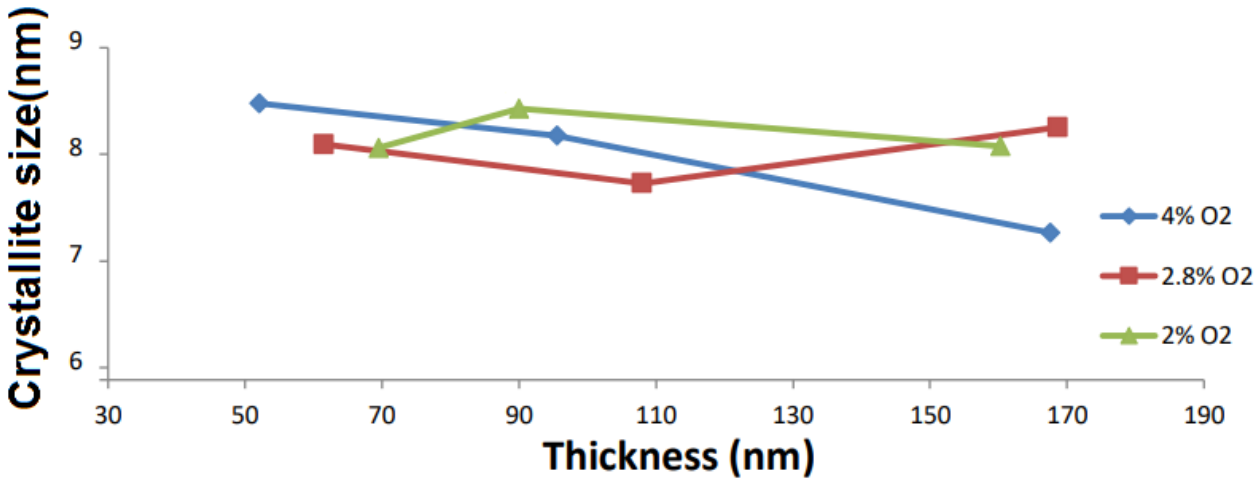

Figure 5.4: Calculated crystallite sizes of all specimens versus their thickness.

Due to the films being too thin for a regular SEMicroscope, a FE-SEM was used and in the following images the results are being presented.

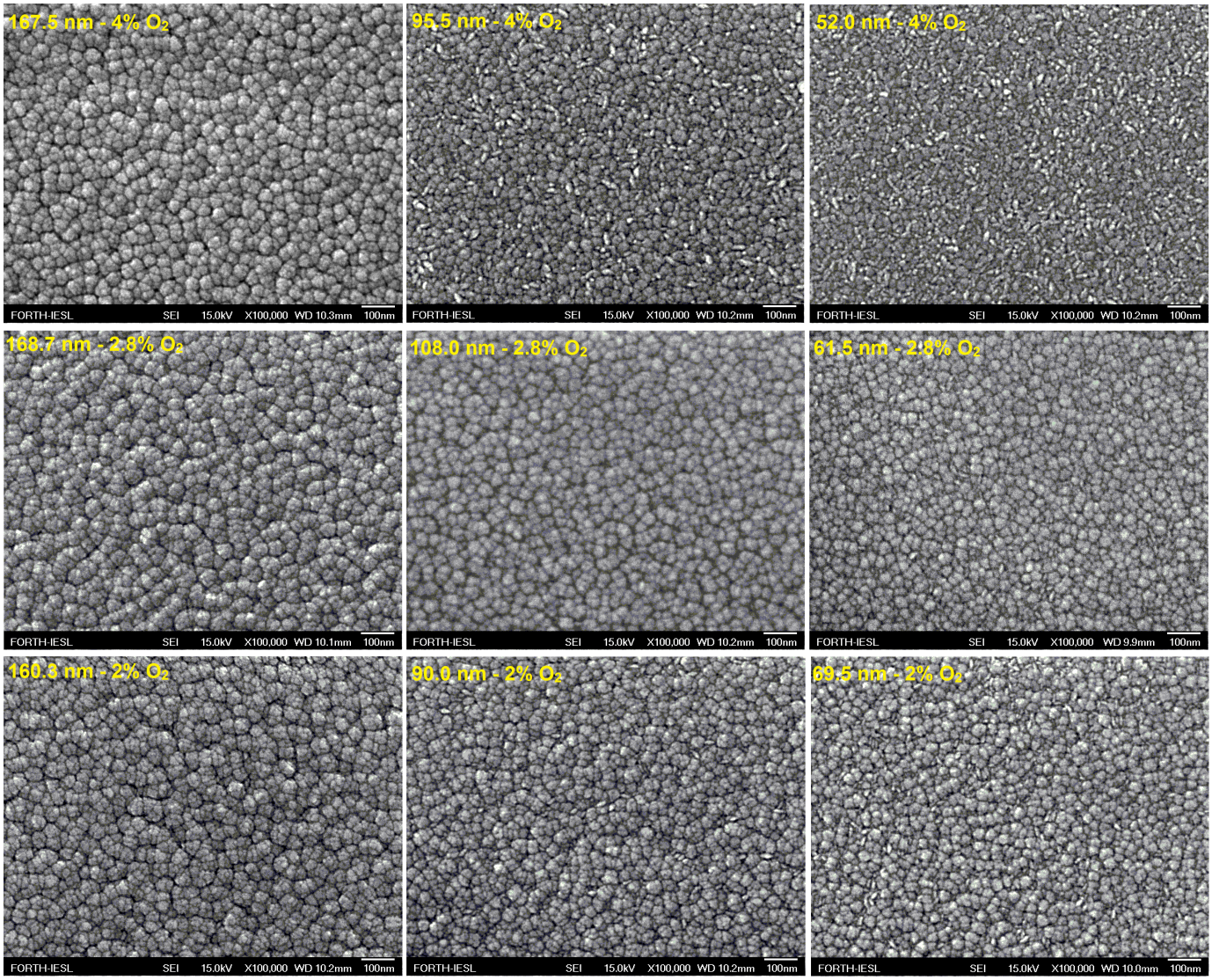

Figure 5.5: FE-SEM images of the surfaces of all specimens of Al:NiO.

It can be seen that all the specimens have a homogeneous structure with similarly spherical grains. As the films get thinner the grains, whilst retaining their spherical structure, diminish in size substantially.

Last but not least, the transmittance of all specimens was measured in order to determine the energy gap of the semiconductor.

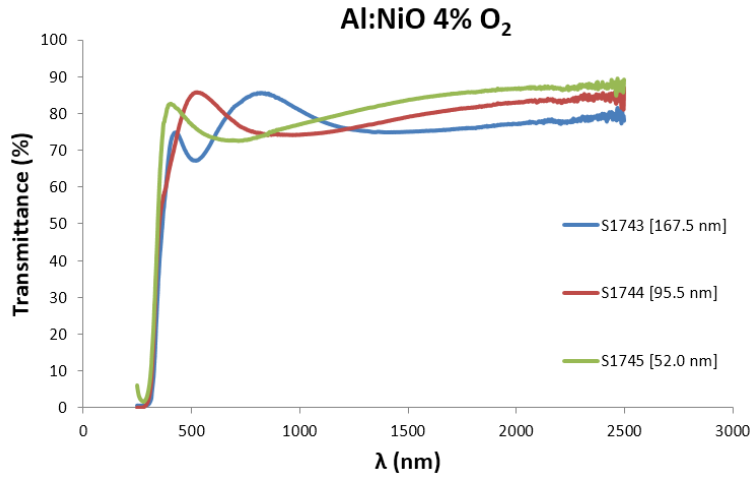

Figure 5.6: Transmittance spectra of specimens S1743-44-45 (167.5 nm, 95.5 nm,52.0 nm) (4% O_2 in plasma)

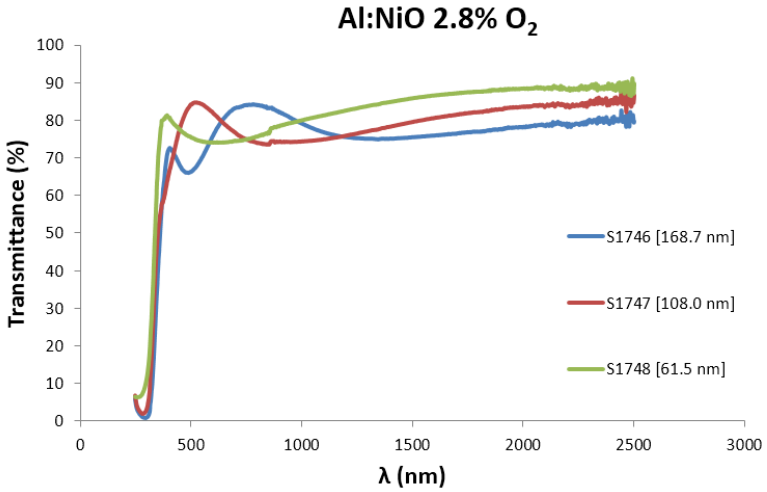

Figure 5.7: Transmittance spectra of specimens S1746-47-48 (168.7 nm, 108.0 nm, 61.5 nm) (2.8% O_2 in plasma)

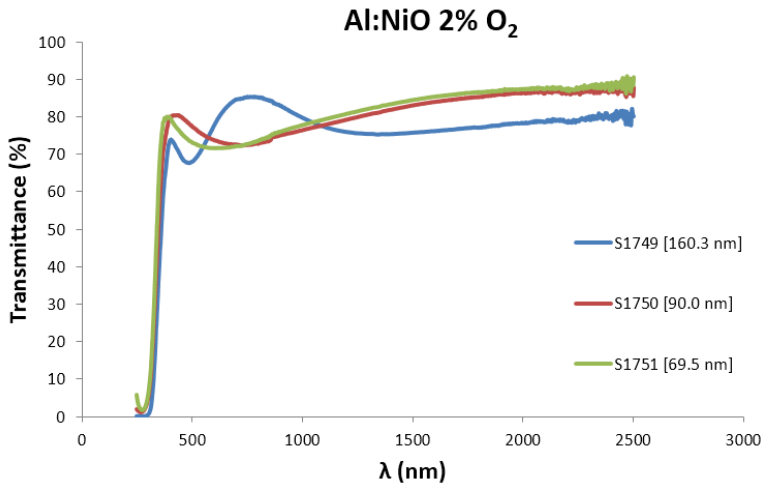

Figure 5.8: Transmittance spectra of specimens S1749-50-51 (160.3 nm, 90.0 nm, 69.5 nm) (2% O_2 in plasma)

From the transmittance diagrams it is concluded that the permeability at the optical spectrum (400-700 nm) ranges from 70% to 90%. What is worth mentioning is that specimens with greater thickness appear to be slightly more transparent than the thinner ones. This can be attributed to the increased number of impurities in the specimen that absorb photons in the specific range. In order to depict the Tauc plot, the absorption coefficient was calculated.

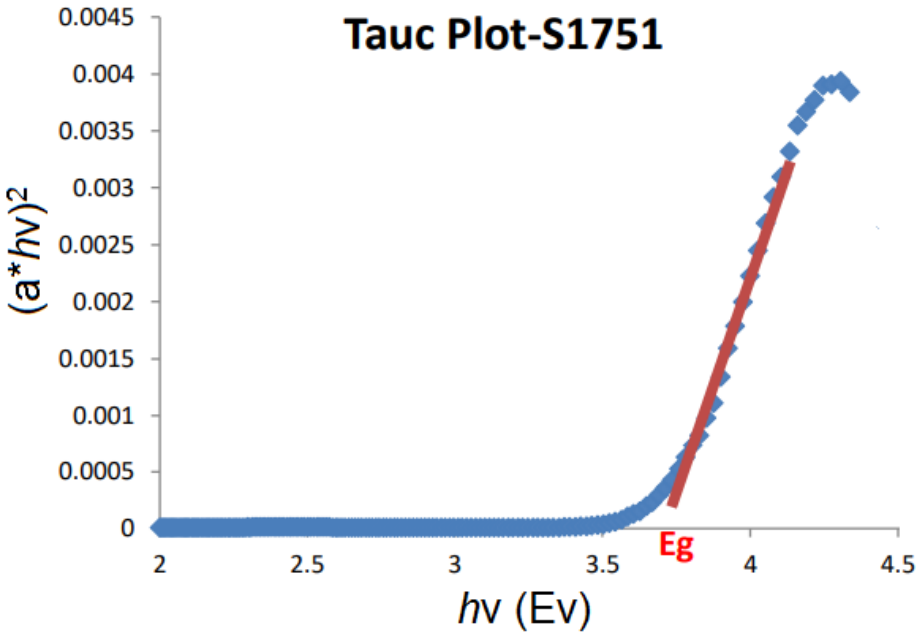

Figure 5.9: Tauc plot of specimen S1751 (2% O_2 in plasma, 69.5 nm) for the calculation of the Energy gap.

Using the same procedure, the Eg of all specimens was calculated and is hereby presented.

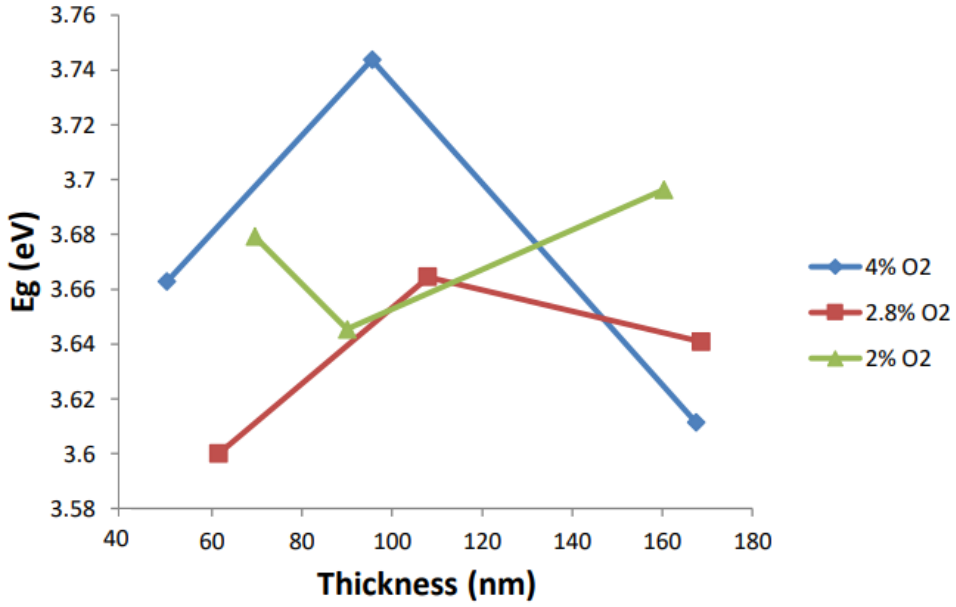

Figure 5.10: Calculated energy gaps of all specimens depending on their thickness.

5.2 Gas Sensing Results and Discussions

In the following graphs of Figures 5.11-5.13 the electrical current variations of each sample against different O_3 concentrations at different temperatures are presented. Initially, the specimen was exposed to dry synthetic air for approximately 45 minutes in order to reach a saturated level of current value. Subsequently, the sample was exposed for 5 (4% O_2 in plasma) or 10 (2.8% & 2% O_2 in plasma) minutes to O_3 of specific concentration and later exposed to 10 (4% O_2 in plasma) or 15 (2.8% & 2% O_2 in plasma) minutes of synthetic air for the recovery.

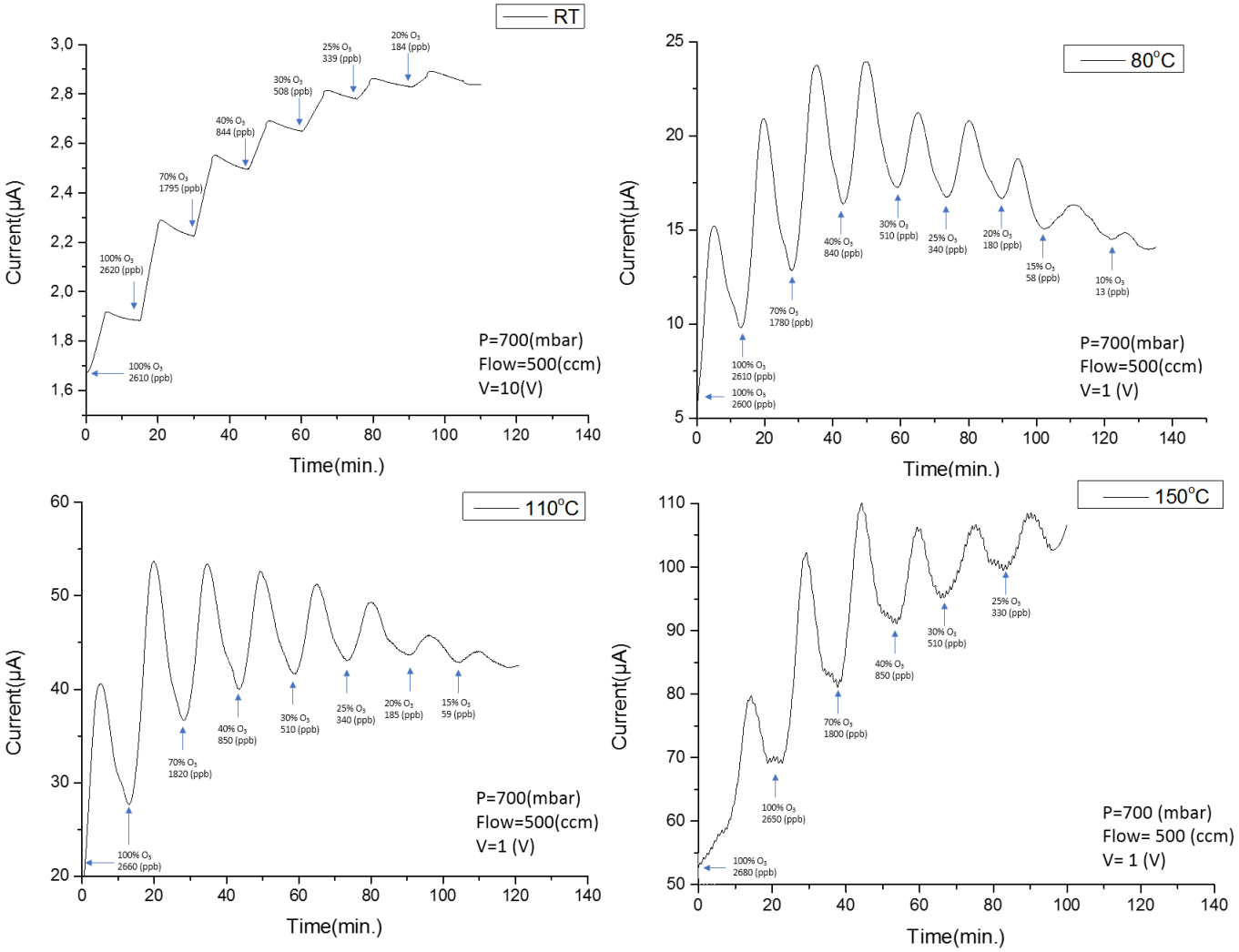

Figure 5.11: Electrical current variations under exposure to O_3 of different concentrations, of a 167.5 nm Al:NiO film grown with 4% O_2 in plasma by the RF sputtering technique.

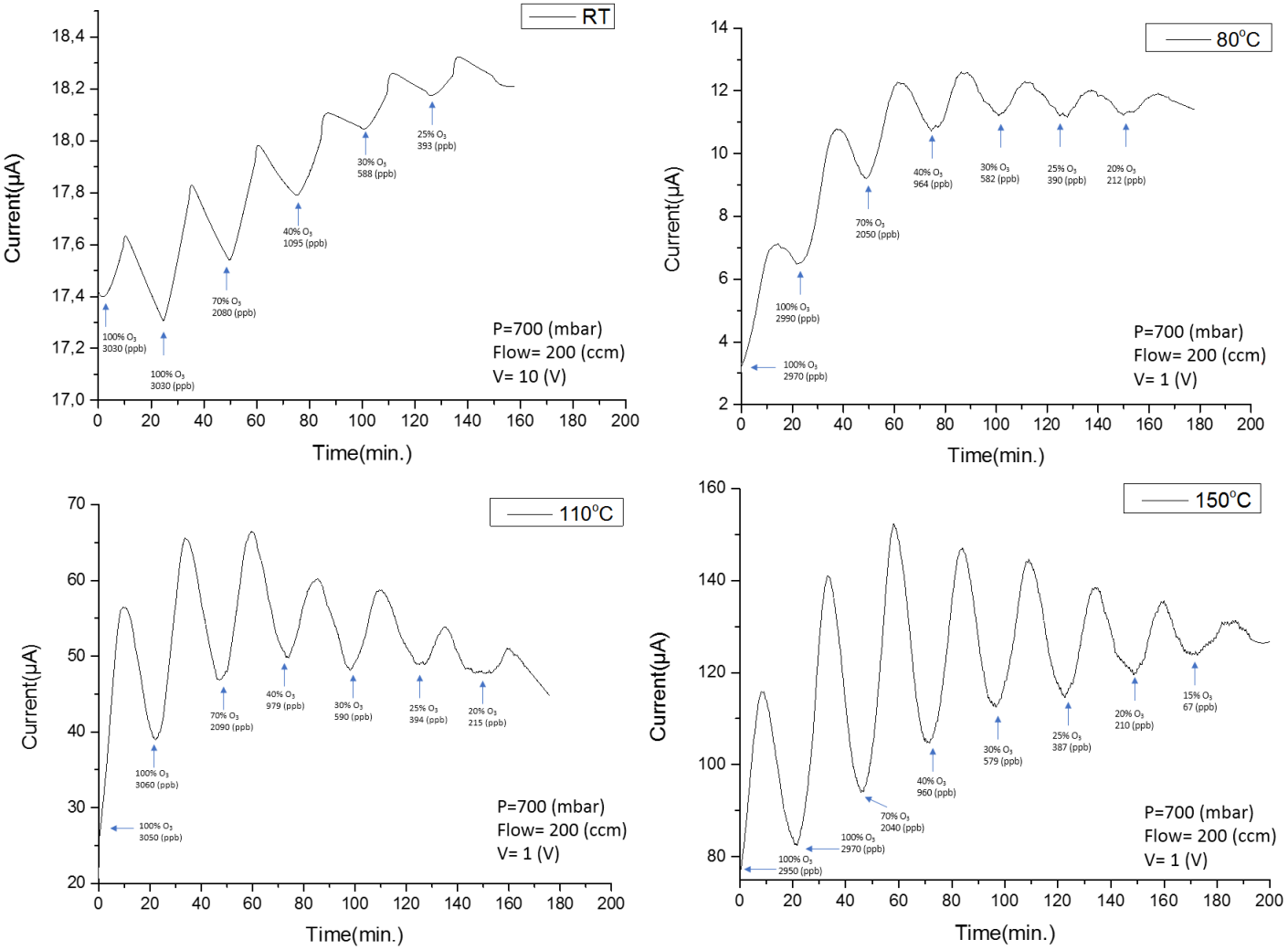

Figure 5.12: Electrical current variations under exposure to O_3 of different concentrations, of a 168.7 nm Al:NiO film grown with 2.8% O_2 in plasma by the RF sputtering technique.

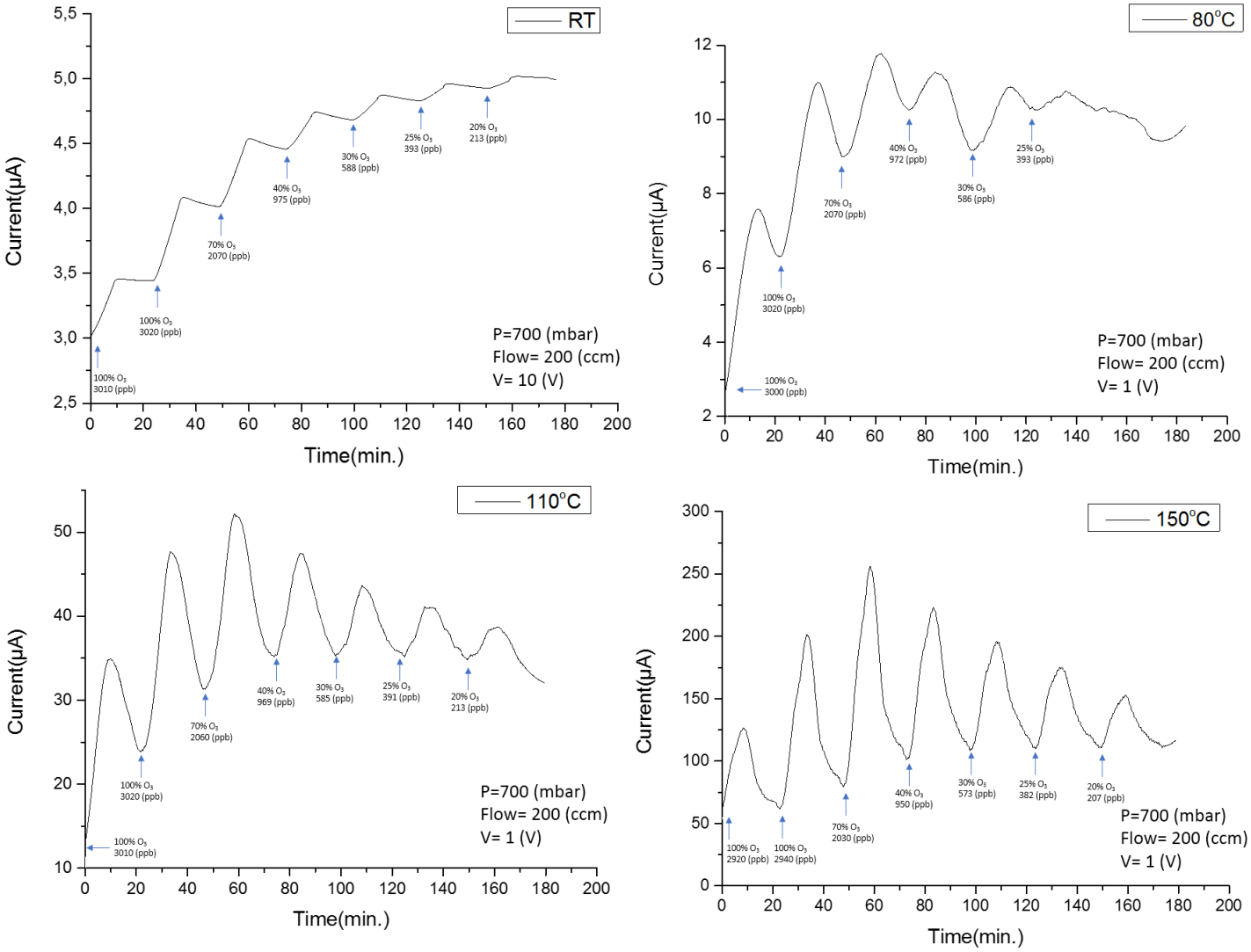

Figure 5.13: Electrical current variations under exposure to O_3 of different concentrations, of a 160.3 nm Al:NiO film grown with 2% O_2 in plasma by the RF sputtering technique.

In order to evaluate the gas sensing performance of Al:NiO films, sensitivity as well as response and recovery time were calculated by the fluctuations in the electrical current shown in Figures 5.11, 5.12, 5.13. The quantities that have been calculated are meant to provide an accurate depiction of the sensitivity of our specimens and their overall performance as gas sensors. Figure 4.13 explains the calculations that lead to the following figures.

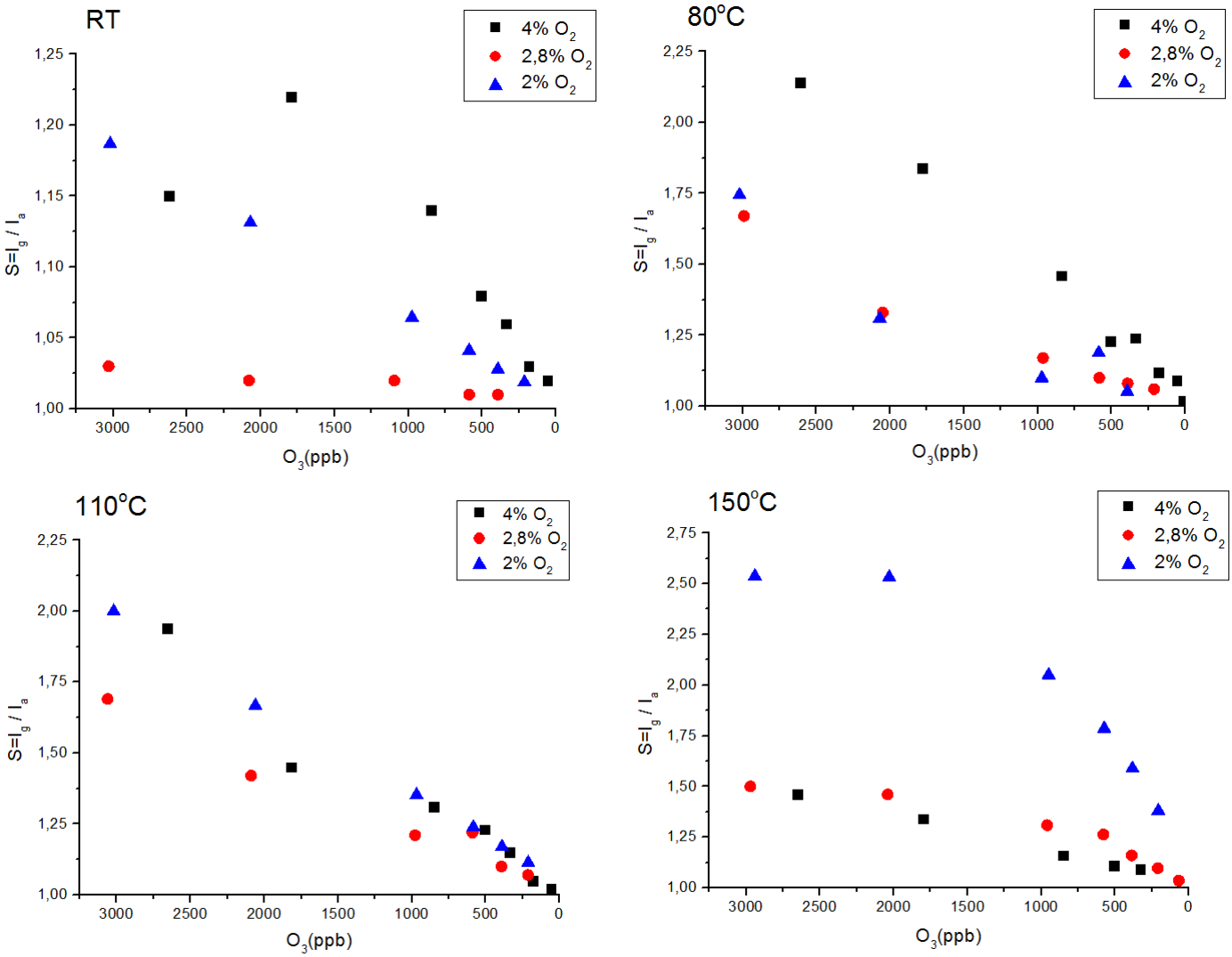

Figure 5.14: Sensitivity of each specimen in varying concentrations of O_3 and temperatures.

It is perfectly clear that the sensitivity of these specimens is more than adequate to qualify as a suitable gas sensor, compared to other O_3 gas sensors [1, 4, 7, 11–13]. From the lot, the performance of specimen S-1749 (2% O_2, 160.3 nm) stands out at an optimal operating

temperature of 150°C. An argument, though, could be made about specimen S-1743 (4% O_2, 167.5 nm) as it is the front runner at 80°C, as far as sensitivity is concerned, due to the sheer decrease of optimal temperature by about 70°C, but also because the sensitivity does not drop by a vast amount. What is evident, though, from the aforementioned figures is that at room temperature there is not adequate recovery to the sensor.

Sensing material	Ozone level (ppb)	Operating temp. (°C)	Sensitivity (S)	Response time (sec.)	Recovery time (sec.)	Ref.
WO_3	54	200	3.0	~15	~200	K. Aguir et al.
CuO	300	250	1.4	~150	~820	A. Bejaoui et al.
ZnO	80	250	8	~30	~15	A. C. Catto et al.
α-Ag_2WO_4	80	300	0.6	~7	~13	L. F. da Silva et al.
$SrTi_{0.85}Fe_{0.15}O_3$	100	260	1.5	~26	~72	L. F. da Silva et al.
50% ZnO-50%SnO_2	60	26 under UV irradiation	12	~13	~90	L. F. da Silva et al.
Al: NiO	200	150	1.4	~470	~730	Present work

Figure 5.15: Sensitivity, optimal temperatures, response and recovery times of different O_3 gas sensing materials.

Figure 5.15 takes into account the best performance of each material at the concentration of O_3 closer in value to the ones detrimental to human health. Moreover, the time it takes for each specimen to respond after coming in contact with the target gas of different concentrations along with the time to recover from said contact were calculated and presented in Fig. 5.16-5.18 for each operating temperature, namely RT, 80°C, 110°C and 150°C.

It can be seen that at lower concentrations a lot of fluctuations arise, at a, somewhat, steady gas sensor. These fluctuations could be attributed to the gas sensing setup in addition to the temperature controller that produces background noise that is comparable to the actual measurements.

Due to the fact that S-1743 (4% O_2, 167.5 nm) had smaller cyclical measurements in terms of time (15 min. total time for S-1743, compared to 25 min. total time for the other two specimens), the numbers may be misleading when trying to determine the optimum Al:NiO film for an O_3 gas sensor. Thus, the percentage of time spent on response and recovery has been calculated in regards to the total amount of time of each cycle and is hereby shown in Fig. 5.20-5.23.

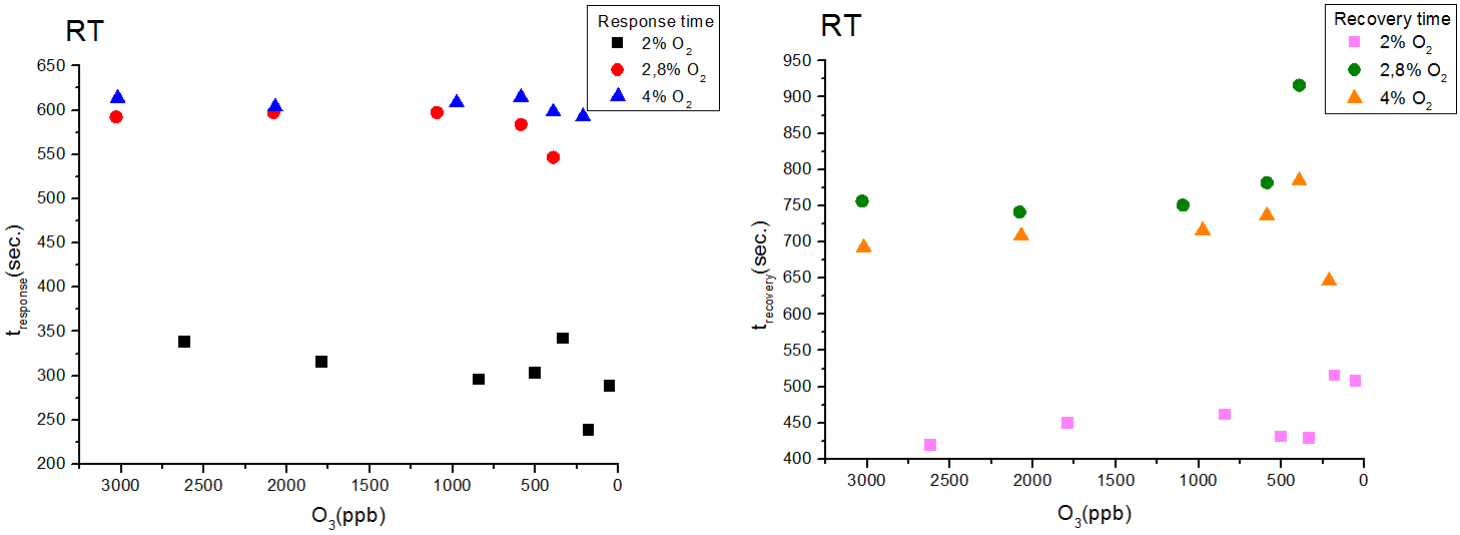

Figure 5.16: Response and recovery time of Al:NiO films against O_3 at room temperature.

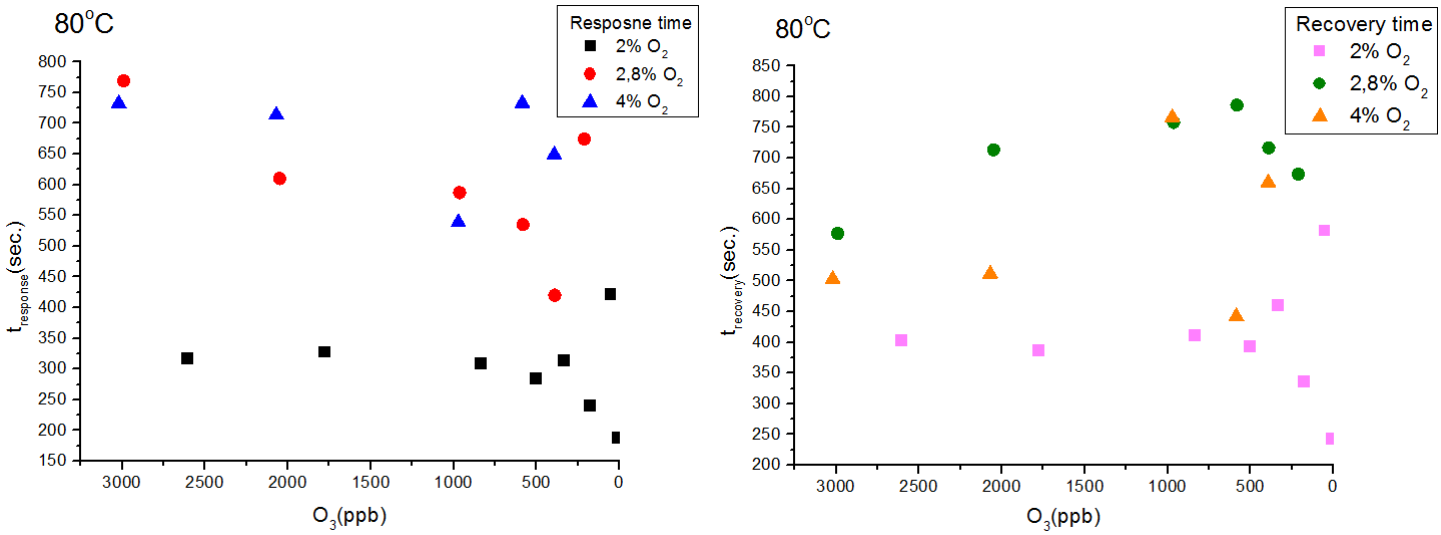

Figure 5.17: Response and recovery time of Al:NiO films against O_3 at 80°C.

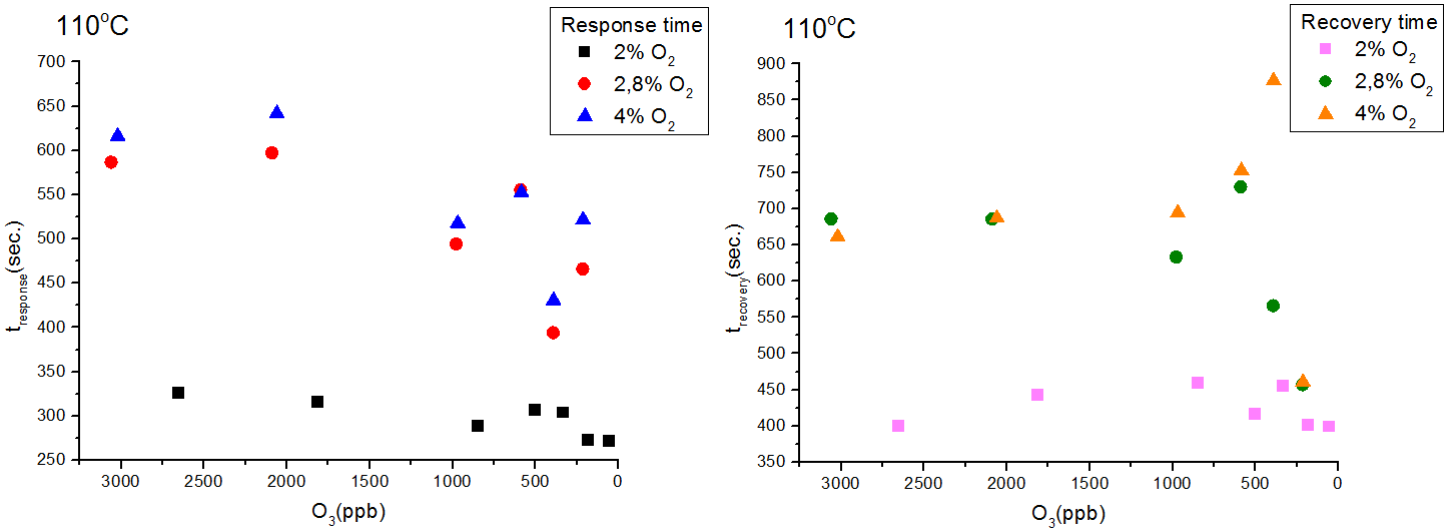

Figure 5.18: Response and recovery time of Al:NiO films against O_3 at 110°C.

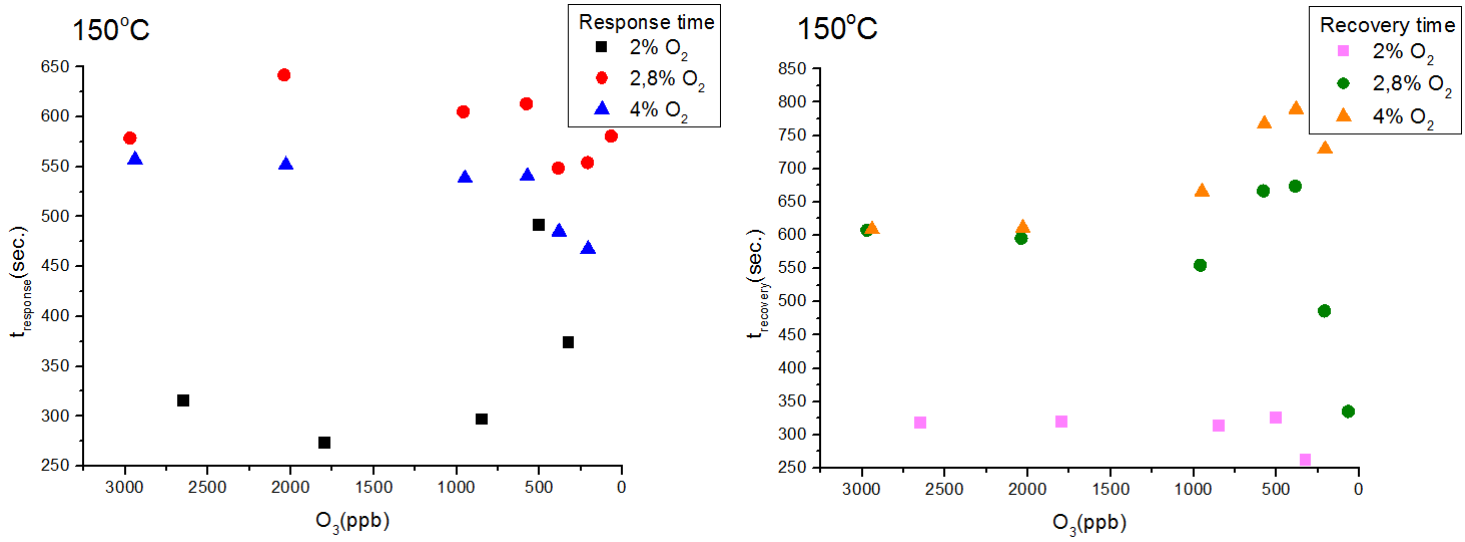

Figure 5.19: Response and recovery time of Al:NiO films against O_3 at 150°C.

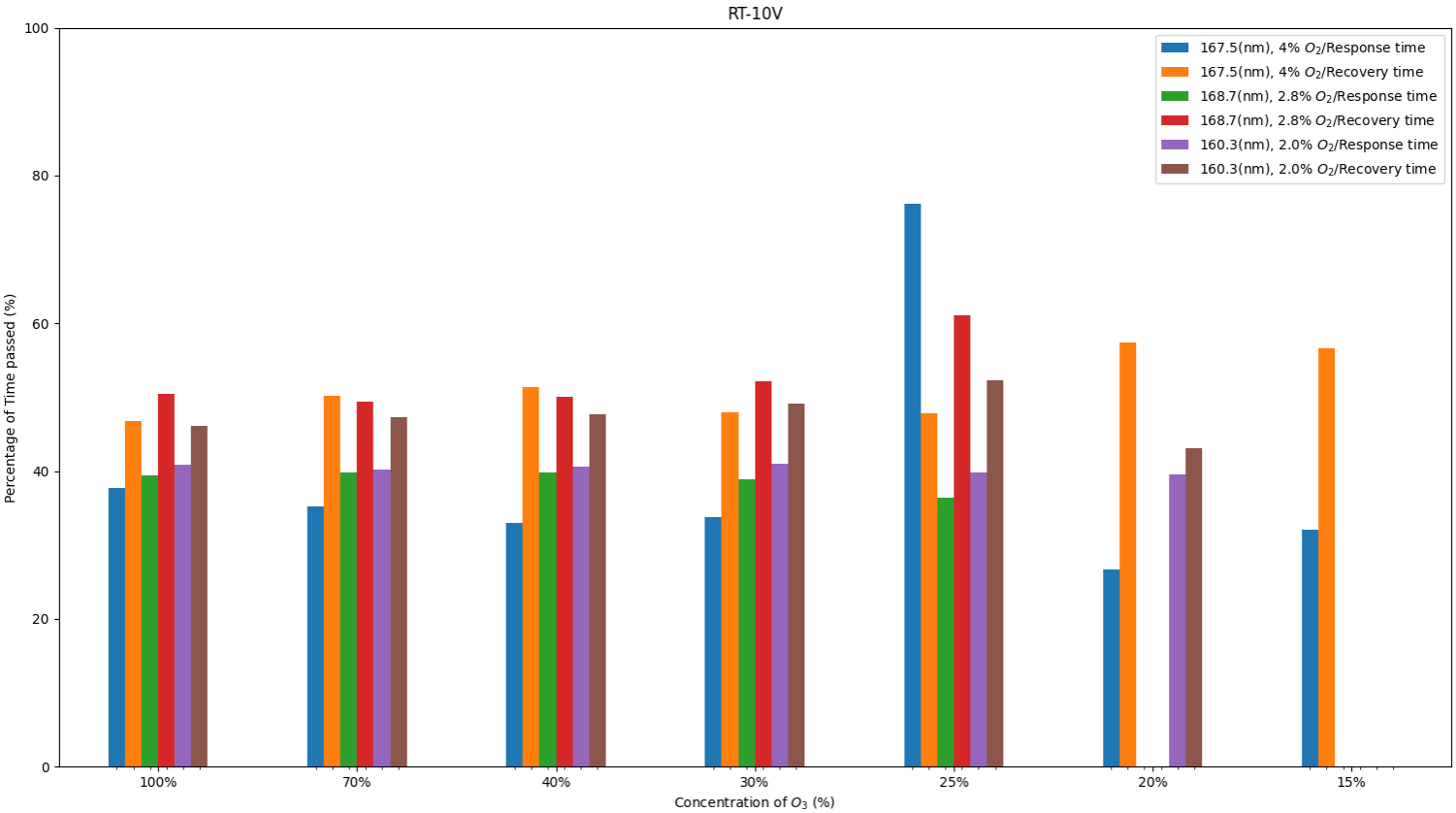

Figure 5.20: Bar chart representing the percentage of time spent on response and recovery in regards to the total amount of time in each cycle at RT for each specimen.

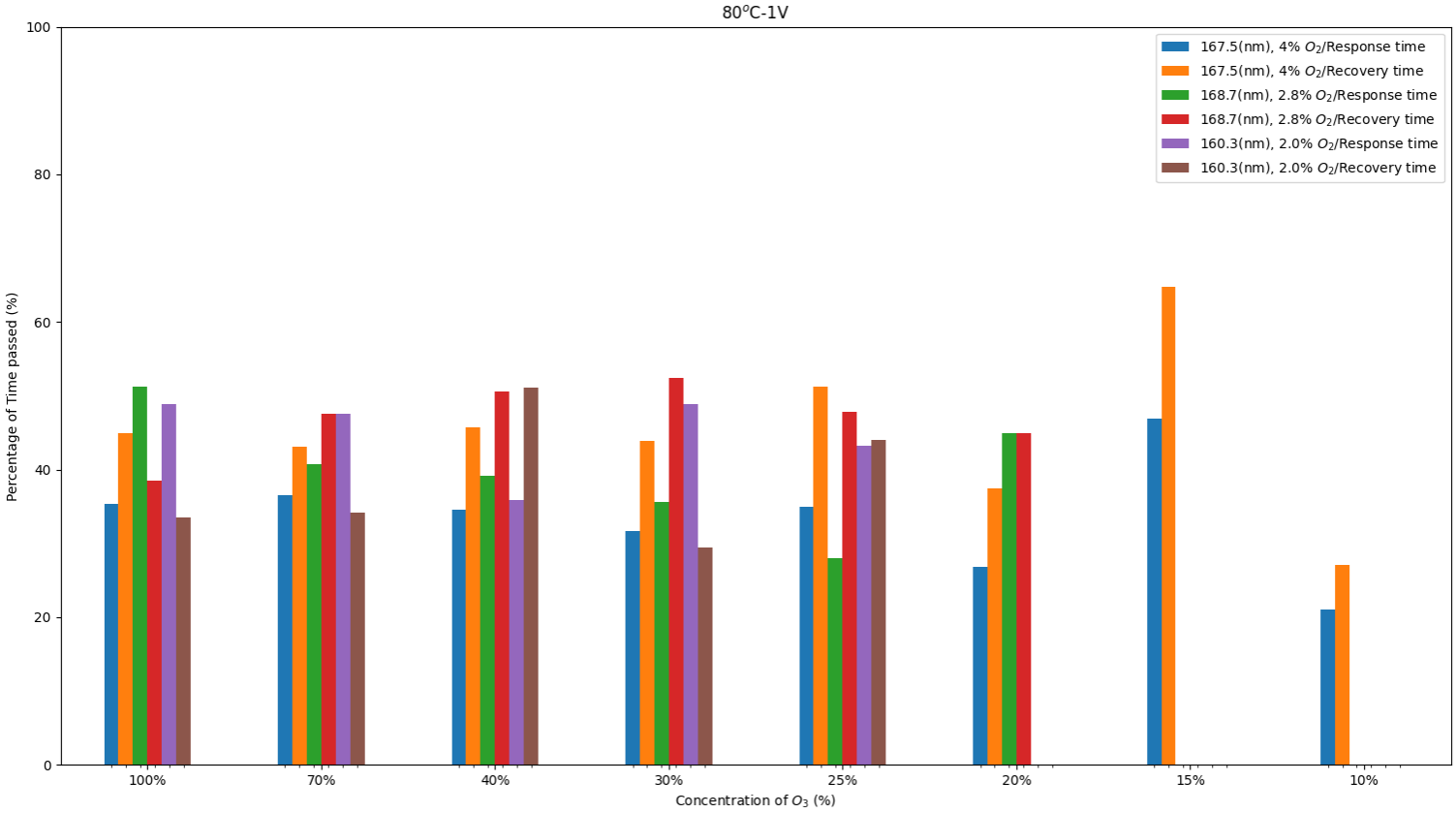

Figure 5.21: Bar chart representing the percentage of time spent on response and recovery in regards to the total amount of time in each cycle at 80°C for each specimen.

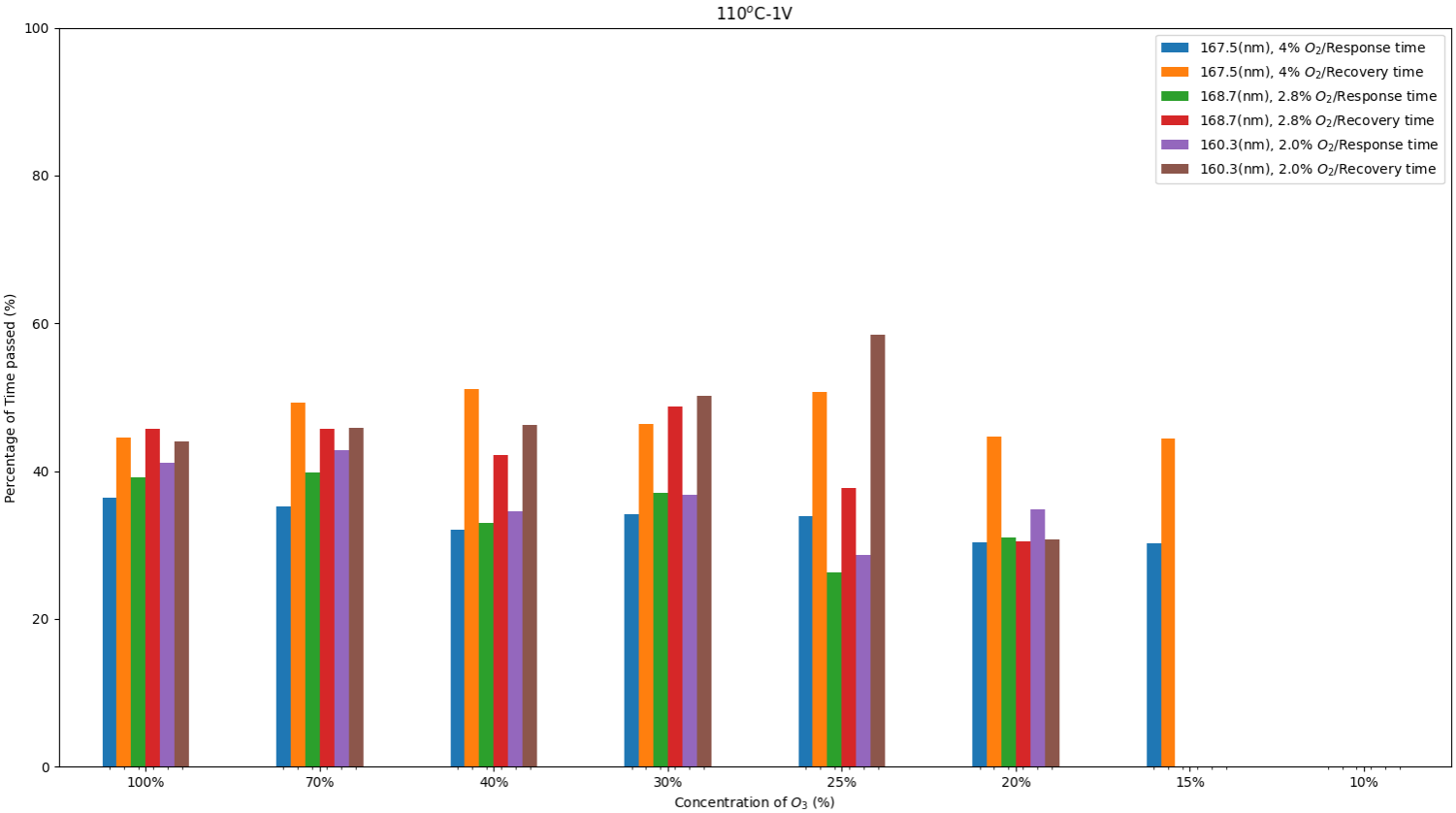

Figure 5.22: Bar chart representing the percentage of time spent on response and recovery in regards to the total amount of time in each cycle at 110°C for each specimen.

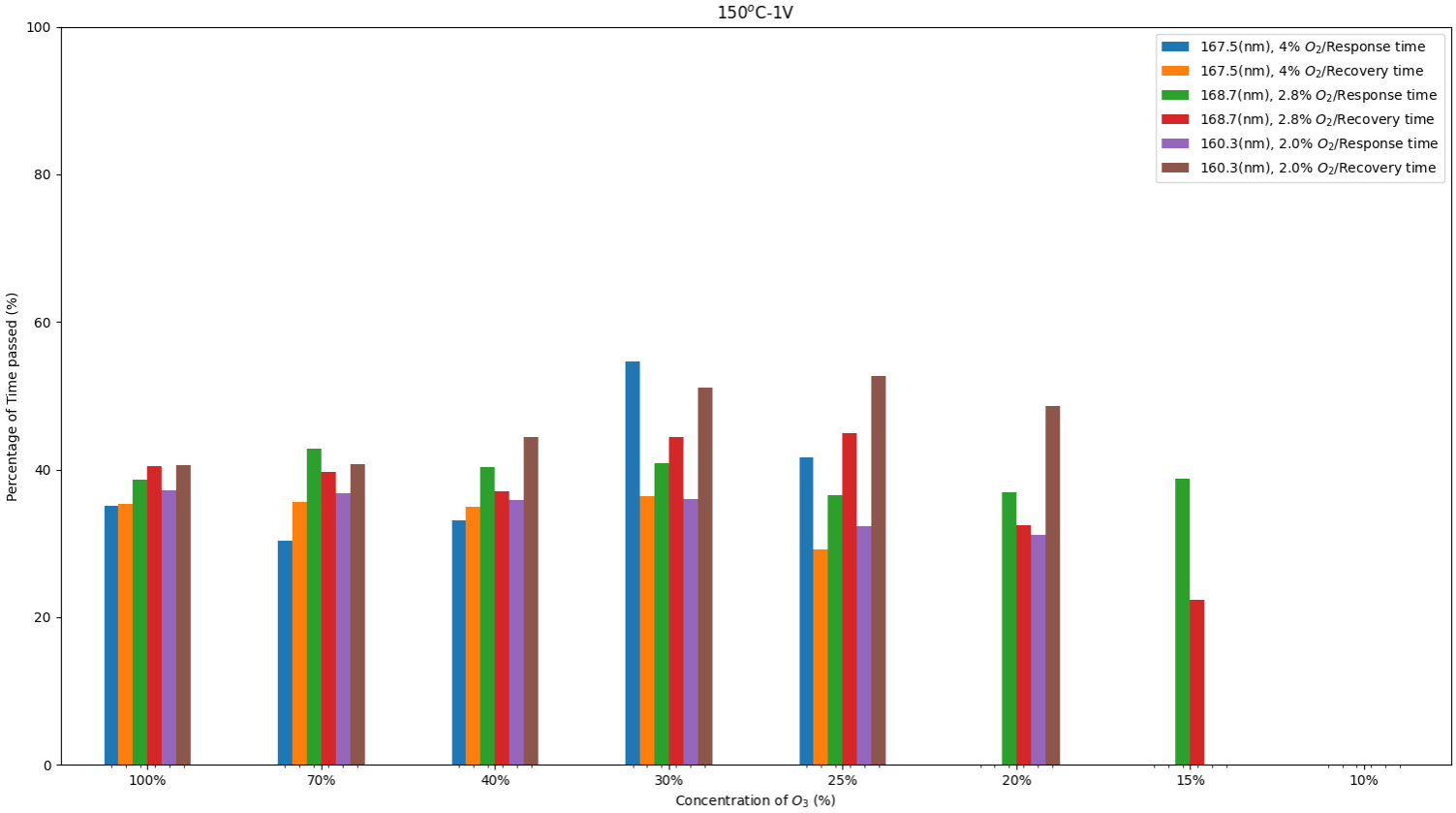

Figure 5.23: Bar chart representing the percentage of time spent on response and recovery in regards to the total amount of time in each cycle at 150°C for each specimen.

Finally, figures 5.20-5.23 make abundantly clear that as we move towards lower concentrations our gas sensors do not react adequately or at all in some cases. Nevertheless, we can see that all samples appeared to have similar gas sensing performances, proving that absolute time is actually misleading.

Circling back to the results regarding response and recovery time, these gas sensors do not match up well with O_3 gas sensors of other works as seen in Fig. 5.15. However, most projects do not present data for the response and recovery time of the sensors and mainly focus on the sensitivity of the compound. This proves detrimental to the scientific community as a whole, as these parameters are a key factor to the transition of the sensor from the lab to the real world. Moreover, due to the different gas cycles that each project submits their sensor to, as with this thesis, absolute time is misleading when trying to determine the best performing compound.

5.3 Conclusions

Nine Aluminum doped NiO films of varying thickness were created and deposited onto IDEs, via the RF sputtering technique, with the key difference being the percentage of O_2 present in the plasma during the deposition. The films were, then, characterised by three different techniques (XRD, FE-SEM, UV-Vis). This thesis focused, mainly, on studying the ozone gas sensing abilities of the the three thicker films(167.5 nm - 4% O_2, 168.7 nm - 2.8% O_2, 160.3 nm - 2% O_2). The variables that were altered during the measurements are the concentration of O_3 present in the chamber as well as the temperature of the specimens. What is evident from this study is that these kind of films are adequately sensitive to O_3 at medium temperatures (80-150^{o}C) but could not recover from the exposure at room temperature. Moreover, the three thicker films that were studied showcase high response and recovery times, which indicates that some further optimisation is required. Regardless, the subject itself necessitates additional measurements in order to determine the lowest concentration of O_3 that the specimens can detect, provided a more stable heating stage. This could also lead to less background noise in the measurements themselves. A following work could also include carrier excitation with UV light that may result in a lower optimal temperature.

Bibliography

[1] K Aguir, C Lemire, and D.B.B Lollman. Electrical properties of reactively sputtered wo3 thin films as ozone gas sensor. *Sensors and Actuators B: Chemical*, 84(1):1 – 5, 2002. E-MRS 2001 conference papers.

[2] Ayaz Ali, Ozhan Koybasi, Wen Xing, Daniel N. Wright, Deepak Varandani, Takashi Taniguchi, Kenji Watanabe, Bodh R. Mehta, and Branson D. Belle. Single digit parts-per-billion nox detection using mos2/hbn transistors. *Sensors and Actuators A: Physical*, 315:112247, 2020.

[3] A. Alshahrie, S. Joudakzis, Ahmed Al-Ghamdi, Lyudmila Bronstein, and Waleed Mahmoud. Synthesis and characterization of p-type transparent conducting ni1-xruxo (0≤x≤0.1) films prepared by pulsed laser deposition. *Ceramics International*, 45, 09 2018.

[4] A. Bejaoui, J. Guerin, J.A. Zapien, and K. Aguir. Theoretical and experimental study of the response of cuo gas sensor under ozone. *Sensors and Actuators B: Chemical*, 190:8 – 15, 2014.

[5] Vladimir Bochenkov and G Sergeev. Nanomaterials for sensors. *Russian Chemical Reviews - RUSS CHEM REV-ENGL TR*, 76:1084–1093, 11 2007.

[6] Encyclopedia Britannica. https://www.britannica.com/science/semiconductor.

[7] Ariadne C. Catto, Luís F. da Silva, Maria I. B. Bernardi, Máximo S. Li, Elson Longo, Paulo N. Lisboa-Filho, Otaciro R. Nascimento, and Valmor R. Mastelaro. An investigation into the influence of zinc precursor on the microstructural, photoluminescence, and gas-sensing properties of zno nanoparticles. *Journal of Nanoparticle Research*, 16(12):2760, Nov 2014.

[8] Gongxuan Chen, Qing Huang, Tian Wu, and L. Lu. Polyanion sodium vanadium phosphate for next generation of sodium□ion batteries—a review. *Advanced Functional Materials*, 30, 06 2020.

[9] Sheng-Chi Chen, Tsung-Yen Kuo, Hsin-Chih Lin, Rong-Zhi Chen, and Hui Sun. Optoelectronic properties of p-type nio films deposited by direct current magnetron sputtering versus high power impulse magnetron sputtering. *Applied Surface Science*, 508:145106, 12 2019.

[10] Tze-Ming Chen, Ware G. Kuschner, Janaki Gokhale, and Scott Shofer. Outdoor air pollution: Ozone health effects. *The American Journal of the Medical Sciences*, 333(4):244 – 248, 2007.

[11] Luís F. da Silva, Ariadne C. Catto, Waldir Avansi, Laécio S. Cavalcante, Juan Andrés, Khalifa Aguir, Valmor R. Mastelaro, and Elson Longo. A novel ozone gas sensor based on one-dimensional (1d) α-ag2wo4 nanostructures. *Nanoscale*, 6:4058–4062, 2014.

[12] Luís F. da Silva, Valmor R. Mastelaro, Ariadne C. Catto, Carlos A. Escanhoela, Sandrine Bernardini, Sérgio C. Zílio, Elson Longo, and Khalifa Aguir. Ozone and nitrogen dioxide gas sensor based on a nanostructured srti0.85fe0.15o3 thin film. *Journal of Alloys and Compounds*, 638:374 – 379, 2015.

[13] Luís F. da Silva, J.-C. M'Peko, Ariadne C. Catto, Sandrine Bernardini, Valmor R. Mastelaro, Khalifa Aguir, Caue Ribeiro, and Elson Longo. Uv-enhanced ozone gas sensing response of zno-sno2 heterojunctions at room temperature. *Sensors and Actuators B: Chemical*, 240:573 – 579, 2017.

[14] Michael David, Mohd Ibrahim, Sevia Idrus, Tay Ching, and Tay Ching En Marcus. Fundamental review to ozone gas sensing using optical fibre sensors. *TELKOMNIKA*, 13:1133–1144, 12 2015.

[15] Ananya Dey. Semiconductor metal oxide gas sensors: A review. *Materials Science and Engineering: B*, 229:206–217, 03 2018.

[16] ECS. https://www.electrochem.org/semiconductors-shaping-society?fbclid=iwar3goajsypfnzstjof islvw48em6cgmmtptsdcuiz1wsn6apja431vft6rk.

[17] J. Epp. 4 - x-ray diffraction (xrd) techniques for materials characterization. pages 81 – 124, 2016.

[18] Abdullahi Evuti. International journal of engineering sciences a synopsis on biogenic and anthropogenic volatile organic compounds emissions: Hazards and control. *TI International Journal of Engineering Sciences*, 2:145–153, 05 2013.

[19] T. Y. Fan and R. L. Byer. Diode laser-pumped solid-state lasers. *IEEE Journal of Quantum Electronics*, 24(6):895–912, 1988.

[20] Changhao Feng, ZhongWei Jiang, Bin Chen, Pengfei Cheng, Yinglin Wang, and Cheng Huang. Aluminum doped nio nanofibers as chemical sensors for selective and sensitive methanol detection. *Analytical Methods*, 11, 12 2018.

[21] Emmanouil (Manolis) Gagaoudakis, G Michail, Dimitra Katerinopoulou, Konstantinos Moschovis, E Iliopoulos, George Kiriakidis, Vassilios Binas, and E. Aperathitis. Transparent p-type nio:al thin films as room temperature hydrogen and methane gas sensors. *Materials Science in Semiconductor Processing*, 109:104922, 04 2020.

[22] K. Ganga Reddy and M. V. Ramana Reddy. Room temperature ammonia gas sensing properties of NiO thin film. 2269:030100, October 2020.

[23] E. L. W. Gardner, A. De Luca, T. Vincent, R. G. Jones, J. W. Gardner, and F. Udrea. Thermal conductivity sensor with isolating membrane holes. pages 1–4, 2019.

[24] Pei Hao, Ge Qiu, Peng Song, Zhongxi Yang, and Qi Wang. Construction of porous lafeo3 microspheres decorated with nio nanosheets for high response ethanol gas sensors. *Applied Surface Science*, 515:146025, 2020.

[25] Peijue Huangfu and Richard Atkinson. Long-term exposure to no2 and o3 and all-cause and respiratory mortality: A systematic review and meta-analysis. *Environment International*, 144:105998, 2020.

[26] Gary W. Hunter, Sheikh Akbar, Shekhar Bhansali, Michael Daniele, Patrick D. Erb, Kevin Johnson, Chung-Chiun Liu, Derek Miller, Omer Oralkan, Peter J. Hesketh, Pandiaraj Manickam, and Randy L. Vander Wal. Editors' choice—critical review—a critical review of solid state gas sensors. *Journal of The Electrochemical Society*, 167(3):037570, feb 2020.

[27] Haocheng Ji, Wen Zeng, and Yanqiong Li. Gas sensing mechanisms of metal oxide semiconductors: A focus review. *Nanoscale*, 11, 10 2019.

[28] Dong Jiang, J.M. Qin, X. Wang, S. Gao, Q.C. Liang, and J.X. Zhao. Optical properties of nio thin films fabricated by electron beam evaporation. *Vacuum*, 86, 02 2012.

[29] Viktor Kampitakis, Emmanouil (Manolis) Gagaoudakis, D. Zappa, Elisabetta Comini, E. Aperathitis, A. Kostopoulos, George Kiriakidis, and Vassilios Binas. Highly sensitive and selective no2 chemical sensors based on al doped nio thin films. *Materials Science in Semiconductor Processing*, 115:105149, 08 2020.

[30] Dimitra Katerinopoulou, Konstantinos Moschovis, Emmanouil (Manolis) Gagaoudakis, E. Aperathitis, Vassilios Binas, and George Kiriakidis. A comparable study on zno-based room temperature ozone sensing characteristics utilizing conductometric and surface acoustic waves techniques. *Madridge Journal of Nanotechnology Nanoscience*, 2:44–51, 04 2017.

[31] G. Korotcenkov and Beongki Cho. Metal oxide composites in conductometric gas sensors: Achievements and challenges. *Sensors and Actuators B: Chemical*, 244, 12 2016.

[32] I. Kortidis, H. Swart, Suprakas Sinha Ray, and David Motaung. Characteristics of point defects on the room temperature ferromagnetic and highly no2 selectivity gas sensing of p-type mn3o4 nanorods. *Sensors and Actuators B: Chemical*, 285, 04 2019.

[33] J. Li, J. Wang, X. Yi, Z. Liu, T. Wei, J. Yan, and B. Xue. *III-Nitrides Light Emitting Diodes: Technology and Applications*. Springer Series in Materials Science Series. Springer Singapore Pte. Limited, 2020.

[34] Xiao Liu, Sitian Cheng, Hong Liu, Sha Hu, Daqiang Zhang, and Huansheng Ning. A survey on gas sensing technology. *Sensors*, 12(7):9635–9665, 2012.

[35] Mark Mendell. Indoor residential chemical emissions as risk factors for respiratory and allergic effects in children: A review. *Indoor air*, 17:259–77, 09 2007.

[36] Ali Mirzaei, S.G. Leonardi, and Giovanni Neri. Detection of hazardous volatile organic compounds (vocs) by metal oxide nanostructures-based gas sensors: A review. *Ceramics International*, 42, 06 2016.

[37] Paul Naethe, Michael Delaney, and Tommaso Julitta. Changes of nox in urban air detected with monitoring vis-nir field spectrometer during the coronavirus pandemic: A case study in germany. *Science of The Total Environment*, 748:141286, 2020.

[38] Suman Nandy, Biswajit Saha, M. Mitra, and K. Chattopadhyay. Effect of oxygen partial pressure on the electrical and optical properties of highly (200) oriented p-type ni1− x o films by dc sputtering. *Journal of Materials Science*, 42:5766–5772, 07 2007.

[39] A. Neubecker, T. Pompl, T. Doll, W. Hansch, and I. Eisele. Ozone-enhanced molecular beam deposition of nickel oxide (nio) for sensor applications. *Thin Solid Films*, 310:19–23, 1997.

[40] Sunil Patil, Arun Patil, Chandrakant Dighavkar, Kashinath Thakare, R. Borse, Sachin Nandre, N. Deshpande, and R.R. Ahire. Semiconductor metal oxide compounds based gas sensors: A literature review. *Frontiers of Materials Science*, 9, 03 2015.

[41] Kocache Ray. Gas sensors. *Sensor Review*, 14(1):8–12, Jan 1994.

[42] Go Sakai, Naoki Matsunaga, Kengo Shimanoe, and Noboru Yamazoe. Theory of gas-diffusion controlled sensitivity for thin film semiconductor gas sensor. *Sensors and Actuators B: Chemical*, 80:125–131, 11 2001.

[43] Farrukh Sarah, Fan Xianfeng, Mustafa Kiran, Hussain Arshad, Ayoub Muhammad, and Younas Mohammad. *Nanotechnology and the Generation of Sustainable Hydrogen*. Springer International Publishing, 2021.

[44] D. F. (Duward F.) Shriver and P. W. (Peter William) Atkins. *Shriver Atkins Inorganic chemistry / Peter Atkins ... [et. al.]*. Oxford University Press, Oxford, 4th ed. edition, 2006.

[45] Kinga Skalska, Jacek S. Miller, and Stanislaw Ledakowicz. Trends in nox abatement: A review. *Science of The Total Environment*, 408(19):3976 – 3989, 2010.

[46] Hui Sun, Ming-Han Liao, Sheng-Chi Chen, Zhiyue Li, Po-Chun Lin, and Shu-Mei Song. Synthesis and characterization of n-type nio:al thin films for fabrication of p-n nio homojunctions. *Journal of Physics D: Applied Physics*, 51, 01 2018.

[47] Antonio Tricoli, Marco Righettoni, and Alexandra Teleki. Semiconductor gas sensors: Dry synthesis and application. *Angewandte Chemie (International ed. in English)*, 49:7632–59, 10 2010.

[48] Brian Viezbicke, Shane Patel, Benjamin Davis, and Dunbar Birnie. Evaluation of the tauc method for optical absorption edge determination: Zno thin films as a model system (phys. status solidi b 8/2015). *physica status solidi (b)*, 252, 03 2015.

[49] Chen Wang, Xiaobiao Cui, Jiangyang Liu, Xin Zhou, Xiaoyang Cheng, Peng Sun, Xiaolong Hu, Xiaowei Li, Jie Zheng, and Geyu Lu. The design of superior ethanol gas sensor based on the al-doped nio nanorod-flowers. *ACS Sensors*, 1, 11 2015.

[50] Mingjing Wang, Tianyi Hou, Zhurui Shen, Xiaodong Zhao, and Huiming Ji. Mof-derived fe2o3: Phase control and effects of phase composition on gas sensing performance. *Sensors and Actuators B: Chemical*, 292, 04 2019.

[51] Wikipedia. https://en.wikipedia.org/wiki/nickel?fbclid=iwar0x-umktxcdecjtbwowh0ggi4upjj8vacpof 7taratnqers1jj8remlun4.

[52] Wikipedia. https://en.wikipedia.org/wiki/ozone?fbclid=iwar2eiannzh9fgushbjceh1d0gm_ely3l8xm 0mfr5hbcg3jeawf5ud9iugmq.

[53] D. E. Williams, G. S. Henshaw, K. F. E. Pratt, and R. Peat. Reaction–diffusion effects and systematic design of gas-sensitive resistors based on semiconducting oxides. *J. Chem. Soc., Faraday Trans.*, 91:4299–4307, 1995.

[54] Xingyu Xiao, Liangliang Liu, Junhao Ma, Yuan Ren, Xiaowei Cheng, Yongheng Zhu, Dongyuan Zhao, Ahmed A. Elzatahry, Abdulaziz Alghamdi, and Yonghui Deng. Ordered mesoporous tin oxide semiconductors with large pores and crystallized walls for high-performance gas sensing. *ACS Applied Materials & Interfaces*, 10(2):1871–1880, Jan 2018.

[55] Tianhe Yang, Weigen Chen, and Pinyi Wang. A review of all-optical photoacoustic spectroscopy as a gas sensing method. *Applied Spectroscopy Reviews*, pages 1–28, 05 2020.

[56] Wei Yi, Kin Lo, Terrence Mak, Kwong Leung, Yee Leung, and Mei Meng. A survey of wireless sensor network based air pollution monitoring systems. *Sensors*, 15:31392–31427, 12 2015.

[57] Hongquan Zhang, Bin Shen, Wenbin Hu, and Xinlei Liu. Research on a fast-response thermal conductivity sensor based on carbon nanotube modification. *Sensors*, 18:2191, 07 2018.

[58] Kaihui Zhao, Huihong Luo, Zibing Yuan, Danni Xu, Yi Du, Shu Zhang, Yuqi Hao, Yonghua Wu, Jianping Huang, Ying Wang, and Rongsheng Jiang. Identification of close relationship between atmospheric oxidation and ozone formation regimes in a photochemically active region. *Journal of Environmental Sciences*, 102:373 – 383, 2021.

[59] Sikai Zhao, Yanbai Shen, Pengfei Zhou, Jin Zhang, Wei Zhang, Xiangxiang Chen, Dezhou Wei, Ping Fang, and Yansong Shen. Highly selective no 2 sensor based on p -type nanocrystalline nio thin films prepared by sol−gel dip coating. *Ceramics International*, 44, 10 2017.

[60] Weilie Zhou, Robert Apkarian, Zhong Wang, and David Joy. *Fundamentals of Scanning Electron Microscopy (SEM)*, pages 1–40. 01 2006.